Ecole Polytechnique
Département de Mécanique
Laboratoire d'Hydrodynamique de l'Ecole Polytechnique (LadHyX)

Ecoulements diphasiques en microfluidique : De la science à l'application

Thèse d'Habilitation à diriger des recherches
de l'Université Denis Diderot (Paris VII)

présentée par
Charles N. Baroud

Soutenance le 24 octobre 2008 devant le jury composé de :

Françoise Brochard	Présidente
Yves Couder	Rapporteur
Jacques Magnaudet	Rapporteur
Howard Stone	Rapporteur
Jean-Louis Viovy	Examinateur

Note sur la langue

Ce document est rédigé en anglais car, même si j'aprécie et parle la langue de Hergé et de Camus, je l'écris mal. J'ai donc décidé d'utiliser un anglais plus neutre et que je contrôle mieux, pour ne pas offenser la sensibilité des lecteurs francophones qui trouveront sûrement dans ma prose des erreurs ou des expressions "qui ne se disent pas comme ça".

Illustrations et films

Une partie importante des images présntées dans ce document, surtout dans les chapitres 2 et 3, sont extraites à partir de séquences vidéo. Les vidéos associées à ces séquences peuvent être visionnés sur la page web suivante :

`http://www.ladhyx.polytechnique.fr/people/baroud/movies.html`

Résumé

Ce mémoire présente certains travaux en microfluidique, réalisés depuis 2002 au sein du LadHyX. Nous commençons, dans le premier chapitre, par décrire le contexte de la microfluidique de gouttes, aussi bien du point de vue pratique que du point de vue des questions fondamentales. En effet, si les gouttes microfluidiques représentent une piste prometteuse pour la miniaturisation des opérations chimiques et bio-chimiques dans les laboratoires-sur-puce, leur utilisation pose certaines questions auxquelles il faudra répondre avant que cette utilisation ne puisse devenir généralisée.

Certaines de ces questions concernent l'évolution de la forme et de la vitesse d'une goutte dans un microcanal, en particulier par rapport au fluide porteur et dans des géométries typiques de la microfluidique. Quelques résultats sur ces questions sont donnés dans le chapitre 2, où nous étudions d'abord la stabilité de division d'un doigt de fluide peu visqueux dans une bifurcation remplie d'un fluide visqueux. Nous démontrons que la solution symmétrique est toujours instable dans le cas de canaux ouverts à l'atmosphère. Cependant, l'ajout de membranes élastiques au bout des canaux de bifurcation peut stabiliser la division symmétrique pour des nombres capillaires assez faibles.

Ensuite nous nous penchons sur le transport de bouchons de liquide poussés dans un microcanal par une pression d'air. Nous démontrons d'abord une relation nonlinéaire entre la vitesse d'un pont et l'inverse de sa longueur, pour une pression donnée. Cette relation peut-être comprise en tenant compte du changement de la forme des interfaces avant et arrière, dus aux équilibres visco-capillaires au voisinage de ces interfaces. En particulier, le facteur dominant a pour source l'angle de contact dynamique à l'avant du bouchon qui introduit une résistance supplémentaire au mouvement. Ce résultat peut élucider l'augmentation de la résistance au mouvement dans un écoulement diphasique par rapport aux écoulements mono-phasiques.

Par ailleurs, nous étudions le passage d'un tel bouchon à travers une bifurcation en T à angles droits, soumis à un forçage à pression constante. Ce passage est caractérisé par trois évolutions possibles : le blocage du bouchon à la bifurcation, la rupture du bouchon, ou sa division en deux ponts dans les canaux fils. Alors que la pression de blocage peut-être comprise à partir de la simple pression de Laplace à l'avant du bouchon, un équilibre visco-capillaire doit de nouveau être évoqué pour déterminer la transition entre la rupture et la division.

Enfin, ce chapitre 2 explore aussi la sortie d'un liquide à travers un pore et la relation entre cette situation et celle de n pores parallèles. Nous mesurons en premier lieu la forme de l'interface qui tend vers une parabole plutôt qu'un cercle. Nous nous intéressons ensuite à la sortie de l'interface à travers deux pores parallels; l'évolution de l'interface dans ce cas montre trois régimes distincts en fonction du temps. Aux temps courts nous observons une avancée indépendante des deux interfaces, alors qu'aux temps longs nous

revenons à la solution parabolique observée pour un pore unique. Cependant, aux temps intermédiaires, la fusion des deux interfaces qui se rencontrent produit un transitoire durant lequel le flux augmente, et qui produit une redistribution de l'écoulement vers la région du centre, entre les deux pores. Cette évolution est ensuite généralisée à n pores où la redirection du flux vers le centre produit une cascade de fusions en paires de gouttes, et donc des interactions purement locales.

Le chapitre 3 change de ton et s'attaque aux problèmes technologiques du contrôle de gouttes microfluidiques par un chauffage local induit par laser. Cette technologie, co-développée au LadHyX et brevetée par l'Ecole Polytechnique et le CNRS, peut être utilisée pour implémenter les opérations de base sur des gouttes microfluidiques, notamment le contrôle de leur production (fréquence et taille), de leur fusion, division, ou leur tri. Nous démontrons ainsi comment le chauffage par laser peut-être combiné avec la géométrie du microcanal pour implémenter toutes ces opérations.

Un modèle hydrodynamique du fonctionnement de cette technique est aussi présenté afin d'expliquer l'origine de la force agissant sur une goutte. Ce modèle se base sur une description d'une goutte circulaire entre deux plaques infinies, et résout l'équation de Stokes tridimensionnelle moyennée dans l'épaisseur. La force prédite par ce modèle montre un scaling qui augmente quand la taille de la goutte diminue, grâce à l'augmentation de la projection de cette force sur l'axe quand le rayon de courbure local diminue.

Plus loin, des mesures récentes de température, de la dynamique de formation des écoulements, et du transport du surfactant, sont exposées. Ces mesures expérimentales commencent à montrer les limites de l'application de la technique en termes de dynamique, de dépendance sur les fluides et les surfactants utilisés. Enfin, des manipulations avancées mettant en oeuvre des méthodes optiques holographiques pour produire des spots laser variables et complexes sont exposées. Ces techniques ouvrent des possibilités nouvelles pour la manipulation de gouttes à des débits plus élevés et pour implémenter des opérations plus avancées, comme le stockage ou le changement d'ordre des gouttes.

Le quatrième chapitre présente des travaux récents et en cours sur le transport de sufractant autour de la surface d'une goutte et la production de gouttelettes de taille inférieure au micron par le phénomène de tip-streaming. Enfin, deux sujets sont rapidement abordés concernant la statistique des écoulements diphasiques dans des réseaux, ainsi que des applications à la biologie cellulaire du contrôle de gouttes.

Acknowledgements

This document presents the fruits of almost six years of work which was performed at LadHyX. In doing this work, I have benefited from the help of many people, both directly on the scientific aspects, and indirectly on everything else!

On the direct scientific aspects, special thanks should go to Jean-Pierre Delville and François Gallaire, who both struggled along with me on trying to get to grips with the laser manipulation problems. More recently, it has been a pleasure to work with David McGloin and David Burnham on laser heating experiments, Jean-Baptiste Masson, Antigoni Alexandrou, Pierre-Louis Tharaux, and Paul Abbyad on biological problems. Benoit Roman and José Bico also frequently contribute to keeping me sain, as well as Thomas Dubos who teaches me about shear. Patrick Tabeling has also been a source of inspiration and good ideas.

I have been surrounded by very gifted collaborators in the last years namely Cedric Ody, Emilie Verneuil, Maria-Luisa Cordero, Yu Song, Michaël Baudoin, who have had the courage to work in my group. In this, I have also benefited from the help of Paul Manneville on the recent network problems. Undergraduate students have also been instrumental in moving things forward. Those include Sedina Tsikata, Samuel Lemaire, Sabine Mengin, Guillaume Boudarham, Paul Reverdy, Xin Wang, and Pierre-Thomas Brun. The work that these collegues have produced has been impressive and has taught me tremendous amounts that I hope I haven't deformed in this document.

Furthermore, Patrick Huerre and Emmanuel de Langre have played an invaluable mentoring role, because it's not enough to have ideas, you have to be able to get them to work. Thérèse Lescuyer had a huge impact by helping to manage all the material aspects.

Outside LadHyX, I have been enjoying life in common with Antonia, as well as frequent phone calls to Lebanon to my parents and family. I thank them all for the love they give me.

Contents

Charles N. Baroud

Laboratoire d'Hydrodynamique (LadHyX)
Ecole Polytechnique
F-91128 Palaiseau, Cedex
01.69.33.52.61

Né le : 23/11/1972
Nationalités : Liban et USA
Email :
baroud@ladhyx.polytechnique.fr

Formation

– The University of Texas at Austin

Doctor of Philosophy (Doctorat) *12/01*

Thèse expérimentale sous la direction de Harry Swinney, intitulée *"Transitions from three- to two-dimensional turbulence in a rotating system."*

Master of Science in Mechanical Engineering *01/98*

Spécialisation sur les systèmes dynamiques et le design. Etude expérimentale, sous la direction d'Ilene Busch-Vishniac, intitulée *"Induced micro-variations in hydro-dynamic bearings."*

– Massachusetts Institute of Technology

Bachelor of Science *01/94*

Programme combiné en génie mécanique et physique. Mémoire sur la dynamique non-linéaire et le chaos.

Brevets

- Demande de brevet français No. 0407988 : "Circuit microfluidique à composant actif" C.N. Baroud, J-P. Delville, R. Wunenburger, et P. Huerre. Déposée le 19 juillet 2004. Étendue à l'international, juillet 2005. Publiée : 01/2006. Dépot international (Europe, USA, Canada, Japon): 01/2007.

- Demande de brevet français : "Procédé de traitement de gouttes dans un circuit microfluidique". C.N. Baroud et J-P. Delville. Déposé en mai 2006.

Publications

"Induced micro-variations in hydrodynamic bearings," C.N. Baroud, I. Busch-Vishniac and K .Wood, *ASME Journal of Tribology*, v.122, pp.585-589 (2000).

"Experimental and numerical studies of an eastward jet over topography," Y. Tian, E.R. Weeks, K. Ide, J.S. Urbach, C.N. Baroud, M. Ghil, and H.L. Swinney, *Journal of Fluid Mechanics.* v.438, pp.129-157 (2001).

"Nonlinear determinism in time series measurements of 2-dimensional turbulence," M. Ragwitz, C.N. Baroud, B. B. Plapp and H. L. Swinney. *Physica D*, v.162, pp.244-255 (2002).

"Anomalous self-similarity in rotating turbulence," C.N. Baroud, B. B. Plapp, Z.-S. She and H. L. Swinney. *Physical Review Letters*, v.88, pp.114501 (2002).

"Scaling in three-dimensional and quasi-two-dimensional rotating turbulent flows," C.N. Baroud, B. B. Plapp, Z.-S. She and H. L. Swinney. *Physics of Fluids*, v.15 pp. 2091-2104 (2003).

"Reaction-diffusion dynamics: confrontation between theory and experiment in a microfluidic reactor," C.N. Baroud, F. Okkels, L. Ménétrier, and P. Tabeling. *Physical Review E*, v.67, pp.060104(R) (2003).

"Nonextensivity in turbulence in rotating two-dimensional and three-dimensional flows," C.N. Baroud and H. L. Swinney. *Physica D*, v. 184, pp. 21-28 (2003).

"Multiphase flows in microfluidics – a short review," C.N. Baroud and H. Willaime. *Comptes rendus - Physique*, v. 5, pp. 547-555 (2004).

"The propagation of low-viscosity fingers into fluid-filled, branching networks," C.N. Baroud, S. Tsikata et M. Heil. *Journal of Fluid Mechanics*, v. 546, pp. 285-294 (2006).

"Transport of wetting and partially wetting plugs in rectangular microchannels", C. Ody, C.N. Baroud et E. de Langre. *J. of Colloid and Interface Science*, v. 308, pp. 231-238, 2007.

"Thermocapillary valve for droplet formation and sorting, C.N. Baroud, J-P. Delville, F. Gallaire et R. Wunenburger." *Physical Review E*, v. 75 p. 046302(1-5) (2007).

"Capillary Origami: spontaneous wrapping of a droplet with an elastic sheet". C. Py, P. Reverdy, L. Doppler, J. Bico, B. Roman and C.N. Baroud. *Physical Review Letters*, v. 98, p. 156103, 2007.

"An optical toolbox for total control of droplet microfluidics". C.N. Baroud, M. Robert de SaintVincent, et J.P. Delville. *Lab on a Chip*, v. 7, pp. 1029-1033, 2007.

"Capillary origami", C. Py, P. Reverdy, L. Doppler, J. Bico, B. Roman and C.N. Baroud. *Physics of Fluids*, v. 19, p. 091104 .

"Collective behavior during the invasion of a network of channels by a wetting liquid", X.C. Wang, C.N. Baroud. and J.B. Masson. *Submitted*, 2007.

"Thermocapillary manipulation of droplets using holographic beam shaping: Microfluidic pin-ball", M.L. Cordero, D.B. Burnham, C.N. Baroud, and D. McGloin. *submitted*, 2008.

Expérience professionnelle

Ecole Polytechnique, Palaiseau 2002-présent

- Professeur chargé de cours au département de mécanique depuis 09/2006.
- Maître de conférences de 2002-2006.

Chargé de démarrer l'activité en microfluidique au LadHyX.

Ecole Nationale Supérieure des Techniques Avancées (ENSTA) 2005-2007
Enseignant vacataire, cours d'ouverture en Microfluidique.

Ecole Normale Supérieure, Paris 2001-2002
Séjour post-doctoral en microfluidique avec Patrick Tabeling. Méthode d'analyse des réactions chimiques en microfluidique, et mélangeur chaotique. Encadrement de stagiaires. Bourse du ministère de la Recherche.

The University of Texas at Austin
Center for Nonlinear Dynamics 1996-2001
Thèse : mise au point et exploitation d'une plaque tournante afin d'étudier les écoulements turbulents en rotation. Conception et mise au point d'un système de visualisation numérique (PIV). La transition entre un écoulement tri-dimensionnel et bi-dimensionnel est observée par des mesures statistiques (séries temporelles) et dynamiques (champs de vitesse) en fonction de la vitesse de rotation.

UT-MEMS group 1996
Mesures de l'effet de changements micrométriques de la surface d'un roulement hydrodynamique sur les forces exercées.

Sun Microsystems 1994-1995
Responsable du support technique francophone pour l'Amérique du Nord, pour tous les produits hardware et software de Sun Microsystems.

Massachusetts Institute of Technology 1990-1994
Plusieurs projets de recherche dans les départements de physique et de génie mécanique; travail expérimental sur le projet LIGO; numérique sur les systèmes Hamiltoniens.

Etudiants au LadHyX

- Cédric Ody : Thèse (2004-2007) co-encadré avec Emmanuel de Langre.
- Maria-Luisa Cordero : Etudiante en thèse (octobre 2006-).
- Emilie Verneuil : Post-doctorante (septembre 2006- août 2007)
- Michaël Baudoin : Post-doctorant (2008)
- Yu Song : Etudiante en thèse (octobre 2007-) co-encadrée avec Paul Manneville.
- Environ 10 stagiaires de l'Ecole Polytechnique, de l'ENS, de master, ou d'universités étrangères (MIT, U.C. Berkeley, U. of Saint Andrews).

Activités académiques

- Membre du jury de thèse de Marie-Noelle Fiamma, UPMC, novembre 2006.
- Organisateur du mini-symposium *microfluidique* au European Conference on Fluid Mechanics, juin 2006.
- Membre du comité du département de mécanique, 2004-2007.
- Reviewer pour les journaux suivants: Physical Review Letters, Journal of Fluid Mechanics, Physics of Fluids, Lab on a Chip, Microfluidics and Nanofluidics, Journal of Applied Physiology, Journal of Micromechanics and Microengineering, Comptes Rendus de l'Académie des Sciences.

Séminaires et conférences invités

1st European Conference on Microfluidics, Bologna, Italie 12/08
Conférence invitée.

Microdroplets in action symposium, University of Cambridge 05/08
Conférence invitée.

Laboratoire MMN, ESPCI, Paris 06/07
Séminaire du laboratoire.

Journée Microfluidique, Paris 05/07
Conférence invitée.

University of Saint-Andrews, Ecosse. 03/07
Colloquium du département de physique

Centro de Investigación en energia, UNAM, Mexico 02/07
Seminaire du "departamento de termociencias"

University of Cambridge, Department of Chemistry, Angleterre 02/07
Séminaire du "microdroplet group"

Workshop ATOM3D, Thales Research & Technology, Palaiseau, France 07/06
Présentation invitée

Institut Català de Nanotecnologia, Barcelone 06/06
Séminaire de l'institut.

Université Joseph-Fourrier, Grenoble 05/06
Séminaire du laboratoire de Spectroscopie

Laboratoire d'Optique de Biosciences, Ecole Polytechnique 05/06
Séminaire du laboratoire.

Ecole Normale Supérieure de Cachan, Antenne de Bretagne 04/06
Séminaire du groupe de mathématiques.

University of Cambridge, Angleterre 02/06
• Séminaire du *BP Institute for Multiphase Flow*
• Séminaire du *Department of Applied Maths and Theoretical Physics (DAMTP)*

University of Bristol, Angleterre 02/06
Séminaire du groupe de mécanique des fluides, département de maths

University of Texas at Austin 11/05
Séminaire du Center for Nonlinear Dynamics

Institut de Recherche sur les Phénomènes Hors Equilibre (IRPHE), Marseille 12/04
Séminaire du laboratoire

Université de Lille I, Lille 11/04
Séminaire inter-laboratoires physique (CERLA) et chimie (Chimie Organique et Macromoléculaire)

University of Manchester, Angleterre 02/03
Séminaire du Manchester Centre for Nonlinear Dynamics

Observatoire de Paris, Meudon 05/02
Séminaire de l'observatoire

Université Paris Sud, Orsay 03/02
Séminaire du laboratoire FAST.

Ecole Normale Supérieure, Paris 01/02
Séminaire du Laboratoire de Physique Statistique.

American University of Beirut 12/01
Séminaire du departement Mechanical Engineering.

Laboratoire Coriolis, Grenoble 01/01
Séminaire du laboratoire.

University of California, Berkeley 10/00
Séminaire geophysical fluid dynamics.

University of Texas at Austin 10/99
Séminaire du groupe Thermo/Fluids.

American University of Beirut 06/99
Séminaire du Center for Advanced Mathematical Studies.

Interventions orales et posters, après 2000

Zing conference, Cancun, Mexique 02/08
Laser control of microfluidic drops.

MicroTAS 2007, Paris 10/07
Flow and temperature field measurements in a flow focusing geometry subject to optical forcing
M.L. Cordero, E. Verneuil, and C.N. Baroud

MicroTAS 2007, Paris 10/07
Giant deformations and tip-streaming from sheared drops
S. Molesin and C.N. Baroud

Microfluidique 2006, Toulouse 12/06
Thermocapillary manipulation of microfluidic droplets: Theory and applications
C.N. Baroud, J-P Delville et François Gallaire

MicroTAS 2006, Tokyo 11/06
Control of droplets in microchannels through laser-induced thermocapillarity
C.N. Baroud, J-P Delville

World Congress of Biomechanics, Munich 07/06
Modeling pulmonary transport of liquid plugs in microfluidic channels
C. Ody, E. de Langre, et Charles N. Baroud

APS, Division of Fluid Mechanics meeting, Chicago 11/05
Localized laser forcing for breaking, sorting, or blocking droplets in a microchannel
C.N. Baroud et J-P. Delville.

Euromech 472, microfluidique. Grenoble 09/05
Communication invitée

Gordon conference: Physics and Chemistry of Microfluidics, Oxford 09/05
Laser actuated building blocks for droplet microfluidics
C.N. Baroud et J-P. Delville.

Congrès français de mécanique 2005, Troyes 09/05
Modélisation en microfluidique du transport de ponts liquides dans l'arbre pulmonaire
C. Ody et C.N. Baroud.

SPIE (International Society of Optical Engineering) annual meeting, San Diego 08/05
Laser-actuated microfluidic building blocks
C.N. Baroud, J.P. Delville, R. Wunenburger.

2ème Congrès SHF "Microfluidique", Toulouse 12/04
Pompe et vanne microfluidiques actionnées par laser
C.N. Baroud, J.P. Delville, R. Wunenburger et P. Huerre.

International Congress on Theoretical and Applied Mechanics (ICTAM) 08/04
How to breathe in a liquid-filled lung: symmetry of airway reopening.
C.N. Baroud and M. Heil.

American Physical Society, Division of Fluid Dynamics, USA 11/03
A microfluidic model for lung airway reopening.
C.N Baroud and M. Heil

MicroTAS 2003, Lake Tahoe, USA 10/03
Measurement of fast kinetics in a microfluidic system
C.N Baroud, L. Ménétrier, F. Okkels and P. Tabeling

Congrès Francais de Mécanique, Nice 9/03
La microfluidique appliquée aux systèmes de réaction-diffusion
C.N. Baroud, L. Ménétrier, F. Okkels and P. Tabeling

Congrès SHF "Microfluidique", Toulouse 12/02
Analyser une reaction chimique dans un micro-Te
C.N. Baroud, L. Menetrier, T. Colin, F. Okkels et P. Tabeling

Premier colloque Dynamique et Applications, Beyrouth 10/02
Micron-scale fluid dynamics applied to fast chemical kinetics.

American Physical Society, Division of Fluid Dynamics 11/00
Measurements of 2D turbulent spectra in experiments on a Beta-plane.
C.N. Baroud, B. B. Plapp and H. L. Swinney.

Nonlinear-Dynamics and Pattern Formation conference 06/00
Jupiter revisited: New images of rapidly rotating turbulence.
C.N. Baroud, B. B. Plapp and H. L. Swinney.

Chapter 1

Introduction

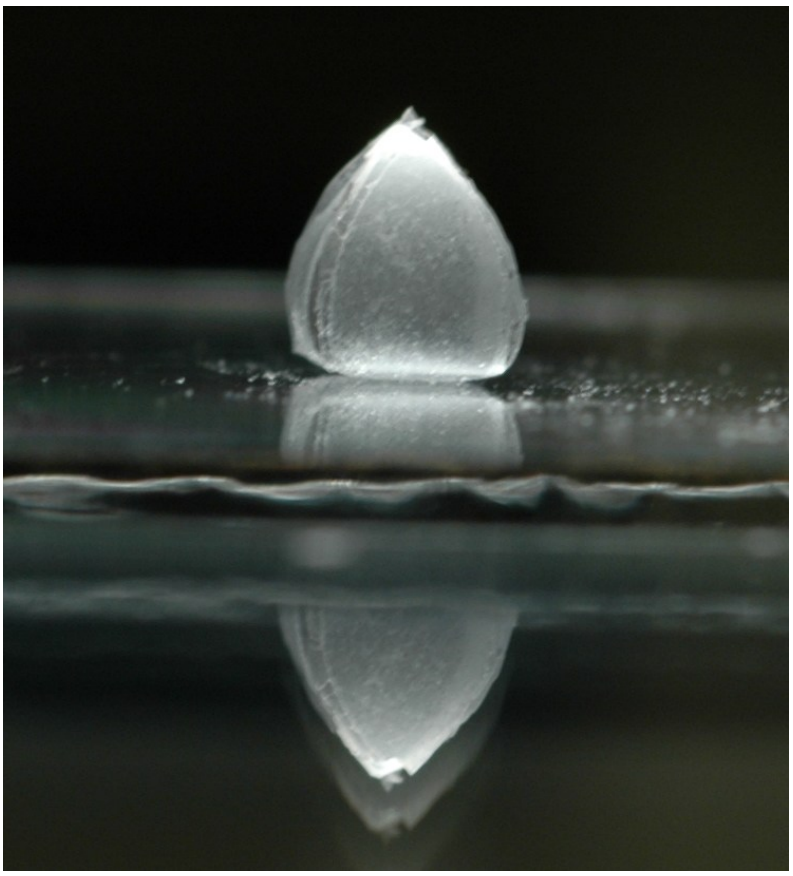

Microfluidics is not a science; it is a tool that allows, through the manipulation of small quantities of fluids, the invention of new and exciting ways to approach problems in biology, chemistry, nanotechnologies, and many other fields. For this reason, the most important publications and conferences on microfluidics bring together scientists from many of the fields cited above, in addition to the fluids engineers and physicists. This makes the field extremely stimulating and encourages people to collaborate together because, unlike more traditional areas, no one can claim to master all of the required expertise to truly produce innovative work in microfluidics. A principal role of fluid mechanics research is therefore to develop further the tools that allow the micromanipulation of fluids and to understand the limitations and opportunities that emerge.

However, microfluidics is also a way to access fluid dynamical phenomena that are difficult or impossible to observe by other techniques. The small scales involved imply that the Reynolds number is usually small, even for moderate fluid velocities (see Ref. [108] for an excellent review). In this way, one can use microfluidics to access situations in which viscous or capillary effects are naturally dominant compared to inertial effects. This idea is not fundamentally new, it follows the same approach as working in the Hele-Shaw geometry or in capillary tubes. The novelty resides in the ability to make the fluidics with complex and well controlled geometries. In this case, microfabrication is the tool that allows new fluid dynamics to be explored.

In both of the cases above, the new techniques also raise significant questions that have constituted the main body of research in microfluidics. Indeed, since the early work on the miniaturization of chemical analysis, it has become clear that a broad range of issues had to be addressed before the devices that were initially promised become available. This is true for example for biochemical sensing techniques when the number of molecules becomes small [71], for material compatibility issues when new materials are used for micro-fabrication [78], as well as for issues in the physical and flow aspects such as mixing without turbulence [92]. The initial microfluidic devices, which were imagined by electronicians and chemists, rapidly ran into the limitations of using simple fluidic resistor models to describe the flow in the channels. One had to realize, for example, that the parabolic profile of a pressure driven flow had important consequences on the device functionality [73, 67].

Moreover, multiple attempts to produce new devices by simply reducing the scale of macroscopic objects have shown that this is often a poor strategy that produces unsatisfactory results. One can see, for example, the decades spent on miniaturizing positive displacement pumps through complex multi-stage lithography techniques and noticing that none of these pumps are commercially available [76]. This is because the force balance is often changed due to miniaturization even though the continuum description remains valid to remarkably small scales. For instance, a valve that is engineered for the centimeter scale relies on the implicit assumption that adhesion forces are negligible compared to the inertia of the valve or fluid. However, such a valve may become unusable, as the scale is reduced, if adhesion is not accounted for. The often quoted adage that surface effects begin to dominate over volumetric effects is true, even though the implications of this domination are not always clear *a priori*.

Finally, one cannot forget the limitations imposed by microfabrication techniques. The vast majority of microfluidics research is done in channels that use some form of photo-lithography and surface etching. Although these techniques allow for the fab-

rication of almost any planar geometry, they rapidly run into difficulties when three-dimensional structures are needed [85]. This implies that making a three-dimensional serpentine channel for chaotic mixing [83] is too difficult to be widely used. More importantly, it implies that most microchannels have a quasi-rectangular cross-section. So forget about all of the axisymmetric analytical solutions to the Stokes flow equations.

All this motivates the fluids physicist or engineer to explore the fluid dynamical aspects of microfluidics. The benefit from this is two-fold:

A – Important advances can be made in understanding the behavior of fluids and beautiful phenomena, which may only be observable on small scales, can be discovered [108]. This is true of many Stokes flow problems that are easier accessed on small scales [67, 13, 10], as well as issues related to flows of rarefied gases when the mean free path becomes comparable to channel size [9, 87], or interactions of viscous flows with deformable membranes such as biological cells [2]. However, nowhere are these new phenomena more present than in multiphase flows, where the interplay between surface tension, viscosity, and geometry produces a plethora of new and surprising situations.

B – An understanding of fluid mechanical concepts opens the door to the invention of tools that are more creative and better adapted to the tasks at hand. In particular, knowledge of certain analytical solutions to fluid flows and can lead to elegant design solutions. A few striking examples include a passive chaotic mixer [111], a passive particle separator [65], a temperature cycling device based on thermal diffusion [22], or a pump that uses nothing but the Laplace pressure to move fluids in a controlled manner [17]. In all of these devices, complex operations are performed by intelligent system design rather than by software or complicated actions.

1.1 Drops in microchannels

One such bright idea, consisted of using droplets as mobile reactors inside microchannels, as shown in Fig. 1.1 [107, 106]. In this figure, three aqueous solutions are introduced through the top three branches of the channel, while an oil solution is introduced from the left side. The water at the junction breaks up into separate drops due to the shear induced by the oil flow. The oil remains a continuous phase due in part to the geometry of the channel and in large part to the relative wetting properties of the water, oil, and channel walls. Furthermore, if the three aqueous inlets contain reacting species, these will react as they come into contact inside each of the drops. In this way, a large number of microreactors are produced in series and following one drop corresponds to observing the reaction's evolution in time.

This idea was not developed in the microfluidics community, it had already been explored in emulsions in order to "compartmentalize" reactions inside many small parallel volumes [115]. For Tawfik and Griffiths [115], each drop in an emulsion represents an artificial cell which can be characterized by a genotype and a phenotype. In other words, each drop contains a strand of DNA which is allowed to produce the associated proteins during the course of an experiment. If the original DNA population is produced with some controlled variations, each drop will be slightly different from its sisters and will

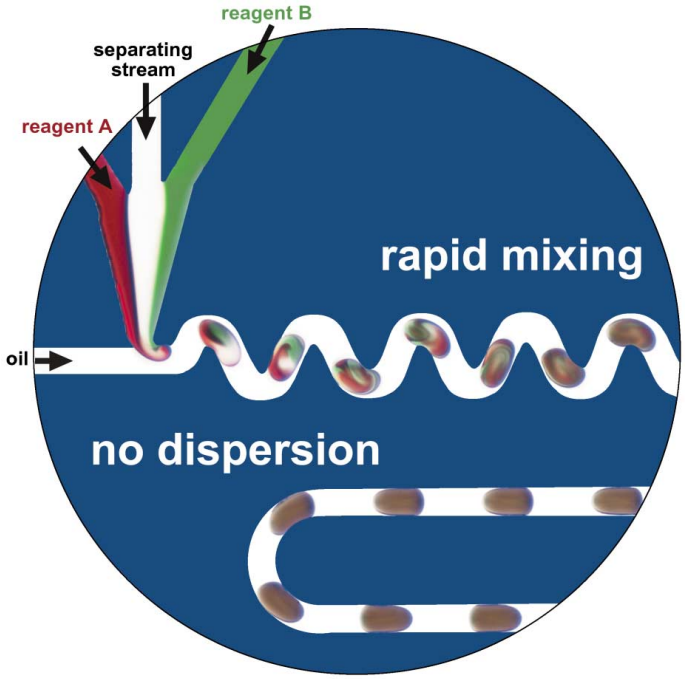

Figure 1.1: Drops used as continuously flowing micro-reactors, carried by an inert oil flow, from [107].

contain a different population of proteins which can later be measured. In this way, the simple passage from a continuous solution to a large number of independent droplets multiplies the total number of experimental realizations, as long as the droplets are well isolated from each other by the continuous phase.

This approach is only useful if two requirements are met: The first is that the volume of each drop is adapted to the experiment that one wishes to perform and the second is that the drops can be manipulated (formed, tested, sorted, or stored) individually. It is therefore a lucky strike that drops measuring a few tens to a few hundreds of microns are well adapted to a large range of experiments and that they can be manipulated rapidly and robustly in microfluidic systems!

By the same token, the use of drops addresses some of the most fundamental problems in microfluidics: dispersion, mixing, and the manipulation of small volumes, as detailed below.

1.1.1 Dispersion

The most obvious problem that is circumvented by drops is the dispersion of species through Brownian diffusion and Taylor-Ariss dispersion, both of which act to reduce the concentration of the flowing species. In the case of droplet microfluidics, a molecule (or cell, or particle) contained inside a drop will remain localized inside the drop, as long as the fluids are properly chosen such that the species is not soluble in the continuous phase. In this way, the initial concentrations inside each drop can be maintained throughout the length of the experiment.

This general statement is only true if care is taken in the choice of fluids because

even very weak miscibility can induce large effects due to the very small volumes at play. For instance, the water contained in the drop can dissolve in the oil phase, due to weak miscibility, if the oil is pure and if the drops are small enough. This effect has been used in order to vary the concentration of a solute in a drop by actively changing its volume [68]. Also, intermediate species during a chemical reaction can be miscible in the oil even if the starting and ending species are not. This may cause problems in the case of complex reactions which rely on a large number of intermediate reaction products. Finally, some species can show micellar solubilization, meaning that the molecules will get trapped in the surfactant micelles even if they are not soluble in the oil itself [121].

However, many systems have already been shown to produce satisfactory results and a few fluid combinations have emerged as standard and robust. While water is the droplet liquid of choice for biological applications, fluorinated oils have been shown to have many attractive features that make them a good carrier fluid for biological samples. They have been successfully used in both molecular and cellular systems [125, 32, 25]. In contrast, silicone oils have also been used to study nucleation kinetics of salts in water drops [77]. Finally, alcanes are often used as cheap and easy substitutes for many fluid mechanical studies [46, 7, 82].

1.1.2 Mixing

Mixing in the absence of turbulence has challenged scientists since the early days of microfluidics. Early on, flows exhibiting Lagrangian chaos were considered for mixing and both passive and active mechanisms were developed for single phase flows, in order to produce the required stretching and folding of material lines [83, 111, 92]. Immiscible interfaces can readily be used to induce flows that display Lagrangian chaos, for example by flowing drops through the zig-zag pattern shown in Fig. 1.1. Here, the presence of the immiscible interface modifies the flow lines, creating recirculation rolls in each fluid which are aligned with the instantaneous direction of the drop. They therefore change as the drop direction is changed in the zig-zag, thus providing a robust way of separating initially close particles [107, 102, 103].

Note however that most of the studies on mixing have been done for ideally shaped drops or bubbles, having several planes of symmetry. However, drops and bubbles can have many different shapes and it has been shown that small changes in the drop shape can strongly modify the mixing efficiency. Shape anomalies can enhance the mixing even in a straight channel [107] but they can also create dead zones inside the drops in which the fluids do not mix [102].

A related effect involves residence time of a fluid particle in the channel. Indeed, the recirculation rolls due to the interface force the liquid from the channel center to the wall regions and vice versa, as shown in Fig. 1.2. Therefore all fluid particles will go through periods in the slow flow regions followed by periods in the fast regions, thus cancelling the variations due to the parabolic flow profile [61]. This “mixing of velocities” is of major importance in the synthesis of materials, for which a good control of the reaction time is crucial in the outcome of the reaction [72].

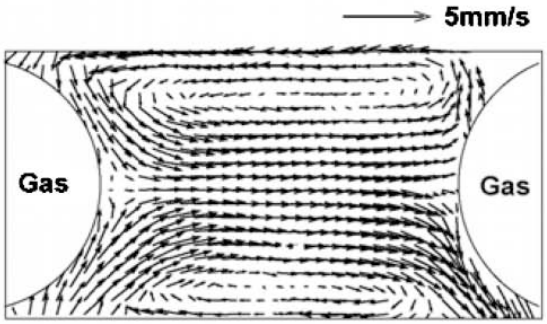

Figure 1.2: Recirculation rolls measured by micro-PIV between two air bubbles, as discussed by Gunther and Jensen [61].

1.1.3 Manipulation

Finally, a more subtle advantage of using droplets is in reducing the gap between the macro-scale lab machines on the one hand, such as syringes and tubes that can be handled by the user, and the microchannels on the other hand. The issue of connecting microchannels whose volume is smaller than 0.1 μL to a syringe and tube whose volume is larger than 200 μL raises important issues in the ability to control the flow in the microchannels. In particular, very minor changes in the tube cross-section can lead to major effects on the flow in the channel so that changes in flowrate must be made on relatively long time scales.

Using microdrops can sometimes be used to circumvent such difficulties by keeping the external forcing constant but using on-chip manipulation of drops. This would in effect move the problem of the manipulation away from the large machines to more precisely tuned micromanipulation tools [33, 5, 4, 96, 12, 11]. The theme of droplet manipulation has been one of the major axes of research in our lab, and will be discussed in detail in Chapter 3.

1.2 The questions that drops raise

As we have seen above, the introduction of drops in microchannels provides an elegant solution to some of the main problems encountered in continuous flow setups. However, this comes at the price of raising a new set of fluid dynamical problems that are due to the deformable interface, the need to take into account surface tension and its variations, in addition to singular events that appear during the merging or splitting of drops.

One approach to dealing with these complications consists of using the tools at our disposal to minimize their practical impact. This is typically the approach taken for chemical applications where the drop is simply a vehicle for transporting reagents. A complementary approach is to tackle the questions in order to elucidate their mechanisms, possibly with the aim of taking advantage of the new understanding for future applications. This is the fluid physicist's niche, one in which innovation can take place.

1.2.1 Motion and shape of clean droplets

Fundamentally, the moving interface introduces new boundary conditions on the fluid flow equations. These conditions add a kinematic and dynamic condition which continually impose a movement of this interface and therefore a new geometry. This coupling between the geometry and the flow constitutes a significant difficulty in looking for analytical solutions to flows of bubbles and drops. It has motivated a large body of research focused on the limit of spherical or nearly spherical drops, starting with the work of G.I. Taylor in 1932, where the underlying symmetries can be used to obtain the flow profile analytically [116, 124]. When the shape departs significantly from sphericity, the recourse is generally experimental, even for G.I. Taylor who moved on to experiments in 1934 in order to study large deformations of his drops [117]. The same coupling between the flow and the geometry has also hindered advances in numerical simulations of drops since they generally require the re-generation of adaptive meshes which follow the drop evolution at each time step and thus become computationally expensive.

Here, we will significantly limit our focus to a subset of the general case. We will concern ourselves with drops (or bubbles) flowing inside confined geometries, and particularly rectangular microchannels. The drops we will consider here have a characteristic length larger than the width and height of the channel and are formed and transported in the microsystem. The formation can be made at a `T`-shaped junction by flowing water into one side and oil into another, as shown in Fig. 1.3. This image shows the typical shape of drops that we are interested in, flowing from left to right in a typical microchannel.

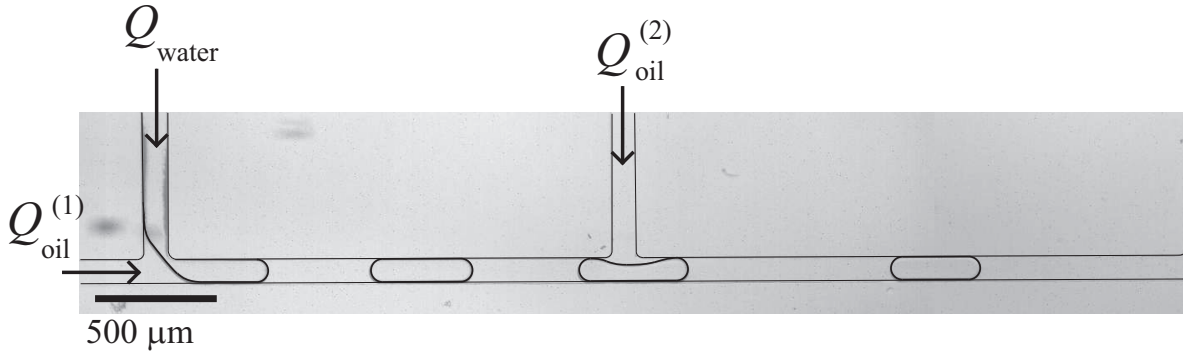

Figure 1.3: Water drops are formed in a Hexadecane phase at the first `T` junction, while a second oil inlet is used to control the total flowrate and spacing between successive drops.

We will also place ourselves in the limit where viscous effects are small compared to surface tension effects. This balance can be quantified through the capillary number $\mathrm{Ca} = \mu U/\gamma$, where μ is the outer fluid viscosity, U its characteristic velocity, and γ the interfacial tension. In the limit of small viscous effects, i.e. $Ca \ll 1$, capillarity implies that the interface shape is a spherical cap.

The first question, whose answer is surprisingly difficult, is to know the relative speed of the drop with respect to the outer fluid. The schematic view of Fig. 1.4, for the case of a channel with square cross-section, begins to show the difficulty of knowing the relative velocities. This is first due to the presence of corners that the drop cannot fill properly, and through which the outer fluid can flow (called "gutters" in Ref. [56]). Depending on the relative velocities of the drop and the carrier fluid, the flow in these

corners can be either forward or backward, in the reference frame of the drop. The effect of this switching of the flow direction strongly affects the recirculation patterns in the inner and outer fluids, thus also changing the mixing and transport characteristics. Indeed, continuity of velocities on the interface implies that the recirculation rolls inside the drop must be different if the flow in the corners is faster or slower than the drop.

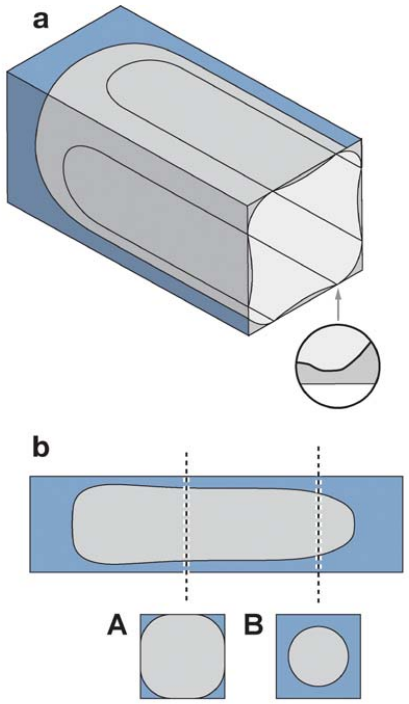

Figure 1.4: Shape of a flowing drop in a square channel, from Ref. [6].

Furthermore, the interface shape can vary as a function of forcing pressure, as shown in part b of Fig. 1.4. Even though this interface retains its spherical shape at the end caps, the radius of curvature will be different at the front and rear, giving the drop the "bullet" shape, also seen in Fig. 1.5. This asymmetry implies that the Laplace pressures at the front and rear of the drop are not balanced, which introduces a supplementary driving term on the drop in addition to the external forcing.

For sufficiently long drops, the magnitude of the curvature change at the front interface is determined by Bretherton's law [24], adapted to the rectangular geometry. This law predicts the thickness of the deposited film, based on a capillary-viscous balance at the transition region between the flat interface near the wall and the curved cap at the front of the drop. In the case of an semi-infinite bubble in a circular tube, Bretherton's law predicts that the thickness of the film (e), normalized by the tube radius (R), should scale as $e/R \sim \mathrm{Ca}^{2/3}$.

As for the rear interface, a modified version of Tanner's law [114] can be used to predict the change in curvature, based on a visco-capillary balance in the corner flow between the drop and the solid wall. The standard result is that the advancing contact angle (θ_a) will increase with increasing capillary number as $\theta_a \sim \mathrm{Ca}^{1/3}$. The net effect of the change in the curvature of the two interfaces is to yield a nonlinear relationship

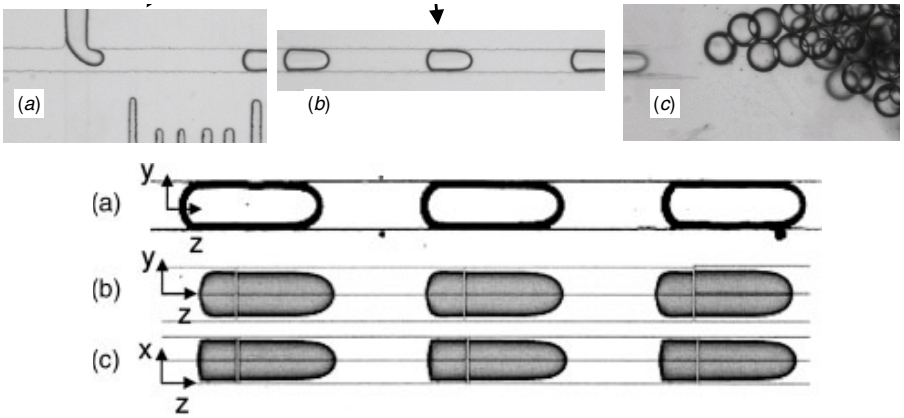

Figure 1.5: Advancing drops take a bullet shape. Top three images show experimental photographs taken from Adzima and Velankar [3]. Bottom three images: Part (a) is an experimental image, while parts (b) and (c) represent numerical solutions of the drop shape, from Sarrazin *et al.* [102].

between the forcing pressure and the velocity of a drop. More practically, in means that the presence of a drop increases the resistance to flow in a given channel, compared to a single phase flow [55, 104].

In our work [91], we have treated a reduction of this problem, by considering the motion of plugs of liquid surrounded by air in a microchannel. These plugs can be taken to represent the space between the drops, for instance the white parts separating the gray bubbles in Fig. 1.5(b); this analysis allowed us to derive an analytical formula for the nonlinear relation between pressure and flowrate and will be treated in detail in Section 2.2.

1.2.2 Presence and transport of surfactants

To this already complex picture one must add the very complex effect of surfactants [81]. The vast majority of droplet microfluidics systems use some surfactants in order to stabilize the wetting conditions, soften the interfaces, and to prevent unwanted mergings of the drops or bubbles. Generally, surfactant is added in large quantities, orders of magnitude above the Critical Micellar Concentration (CMC), which generally still corresponds to a few weight percents. Such large concentrations are necessary since the bulk concentration may drop significantly when the molecules begin to cover the interface, given the large surface to volume ratios involved.

For most practical purposes, simply adding a large concentration of a good surfactant is sufficient for producing beautiful drops. In cases where things do not work properly, one may try several different surfactant molecules and will generally find a combination of fluids and surfactants that provide a satisfactory result, owing to the very large number of available molecules[1]. However, this large variety can be the source of complications when the dynamic situations need to be understood, for example during the creation of a new interface. Indeed, the dynamics of surface tension modification by a

[1]This may be more or less difficult. For instance, there is a limited number of surfactants for fluorinated oils and their performance is not very good.

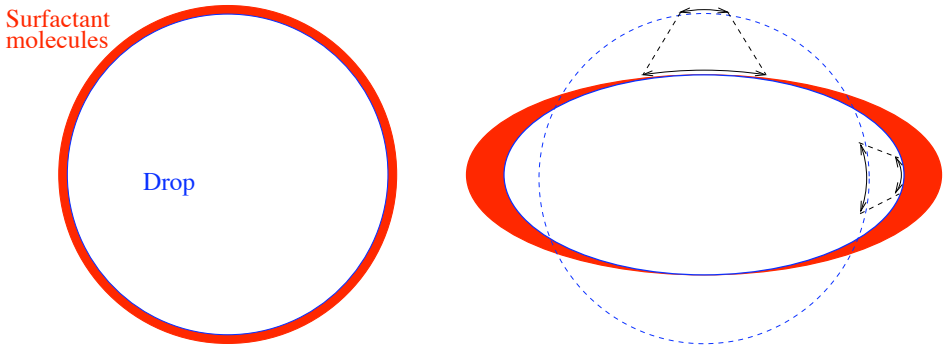

Figure 1.6: Variations of surfactant concentration due to surface dilation and contraction as the drop shape varies. The width of the red region represents the local concentration.

surfactant is an active research subject for stationary interfaces [54, 49, 34]. When the effects of an unstationary flow are added, one quickly reaches many-dimensional parameter spaces where little can be said that is of general use.

For instance, the adsorption/desorption dynamics can vary for different chemical compositions, leading to faster or slower action of the surfactant molecules. Therefore, the amount of surface coverage on the drop detachment shown in Fig. 1.3 may vary for different chemical combinations. In some cases, Marangoni effects will play a role in the drop breakup, while their effects may be negligible in other cases [69].

A more tractable difficulty arises when we allow the surface to dilate: Even though the volume in the drop must remain constant for incompressible and insoluble fluids, a change in the shape of the drop implies that certain regions will go through a surface dilation while other areas will contract (Fig. 1.6). This effect will automatically lead to variations in the surface concentration of surfactant which, in turn, will apply soluto-capillary (Marangoni) stresses [50, 64]. This is shown schematically in Fig. 1.6 where we show a circular drop, initially evenly covered with surfactant, going through a transition to an ellipsoidal shape. The poles of the drop contract and therefore see their surface concentration increase, while regions near the equator see the surface concentration decrease.

Situations in which drops go through large shape changes are very frequent in microfluidics, for example as drops flow through rapid contractions or expansions in the channel geometry. In Fig. 1.7, the relaxation of the drop shape to a circle is used by Hudson et al. [66] to measure the interfacial tension between the drop and the carrier liquid. Although the authors do not address questions of Marangoni effect, it is likely that it will introduce a measurement error in the presence of surface active molecules. This effect was also observed by Bremond et al. [23] when drops were pulled into channel contractions. The authors there observed the creation of "nipples" which favored the merging of drops, in part because those regions were impoverished in surfactant through surface dilation.

Another important effect is due to the surfactant transport along the interface. For instance, the molecules can be swept by the external flow along the drop surface and accumulate at the stagnation points. In the reference frame of the moving drop, the semi-parabolic flow profile in the external fluid must be equal to the drop velocity at two points. This leads to two stagnation points which separate the flow into "external"

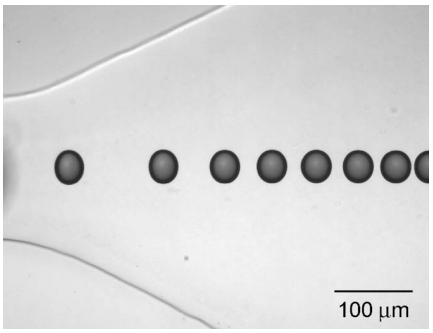

Figure 1.7: Measurements of surface tension by observation the shape relaxation of a drop towards a circle [66].

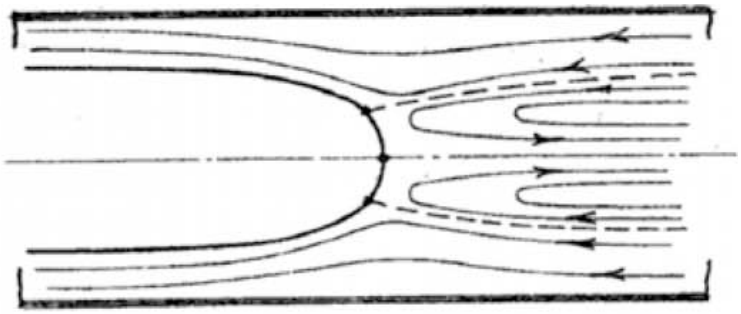

Figure 1.8: Flow profile around stagnation points, proposed by Taylor [118].

and "internal" regions, as shown in Fig. 1.8. If the flow carries with it molecules that energetically prefer adsorbing to the interface, those will display strong adsorption at the stagnation points where the velocities are weak and the molecules spend longer periods. These molecules will then be swept along the interface by the flow, eventually finding themselves trapped at the stagnation points at the rear of the drop. This scenario is true regardless of the relative velocities of the drop and the carrier fluid, since the drop will always travel faster than the outer fluid very close to the walls. For this reason, the front-rear symmetry is always broken.

Since these molecules tend to show a strong asymmetry between adsorption and desorption, they are energetically bound to remain on the interface and we can observe a strong accumulation of surfactants at the rear of the drop. The accumulation effects are especially important in situations where the surfactant is present in weak concentrations because strong surfactant gradients can build up, which lead to drops slowing down significantly with respect to the external flow. Indeed, the superposition of the Marangoni and externally imposed flows yields drops that must travel slower than the external phase, if the Marangoni flow acts on the whole drop. These aspects have not yet been studied in detail in the literature. In our work, we have addressed some related issues, which we discuss in Section 4.1.

A third issue due to the presence of surfactant is the introduction of a surface viscosity term. This effect is well known in the studies of foam drainage [100] but has not been addressed in the microfluidics community specifically. Other exotic two-dimensional

phase transitions can also appear through the accumulation of molecules on the interface, leading to variations in the mobility of the interface [94, 29]. While all of these questions are fascinating, they have not yet been studied and will not be addressed further in this document.

Finally, an effect which we have found to be of major importance has been the effect of heating on surfactant repartition. We have observed anomalous Marangoni flows, i.e. going from the cold to the hot regions, when heating a water-oil interface with a focused laser. The direction of these flows implies that the surface tension has risen due to heating, which is contrary to the traditional statistical mechanical view of interfaces. These aspects will be developed in Chapter 3, where we also show measurements of surfactant transport due to the heating.

1.2.3 Singular events: Formation, merging and splitting

The most violent dynamics happen during singular events, namely those involving breaking or merging of interfaces. The dynamics of these events happen on very short time scales, since they are associated with finite-time singularities, in the case of breaking, and with infinite curvatures at the two touching interfaces, in the case of merging.

During the breakup process, a particularity of microfluidic devices is their confinement, since confined two-dimensional threads cannot break into drops, for example in a Hele-Shaw cell [36]. Therefore, the breakup mechanism that leads to the drop formation can only be based on the Plateau-Rayleigh instability at the very late times, i.e. times when the width of the thread becomes smaller than the channel height.

A geometry for producing drops that has been studied extensively is the flow focusing geometry, shown in Fig. 1.9. Since the initial work of Anna *et al.* [7], several groups have studied in the detail the breakup process of a water or air thread that is confined in a flow-focusing region [58, 45]. It has appeared that the breakup is largely dominated by the imposed flowrate of the external phase, the Plateau-Rayleigh instability only appearing at the very late stages. On a related topic, Guillot *et al.* [60] showed that the confinement of a thread of water in oil could also lead to the complete suppression of the breakup of this thread in a microchannel. The particular geometry of the microchannels therefore plays a major role in the formation of drops, on their size and size dispersion, as well as on the precise location of breakup.

Merging events are different in that they are mainly due to interactions between droplets and are less dependent, a priori, on the geometry. Particularly, the presence of surfactants in the solution is known to stabilize emulsions [18] through several mechanisms, namely through preventing the drainage of the lubrication film that is trapped between two adjacent drops. Significant work has focused on producing droplet merging by manipulating the geometry of the channel and thus manipulating the distance between drops [113], as well as their shapes [23]. However, there does not yet exist a clear picture regarding the mechanisms that passively force droplet merging, although active techniques have been explored, as mentioned below.

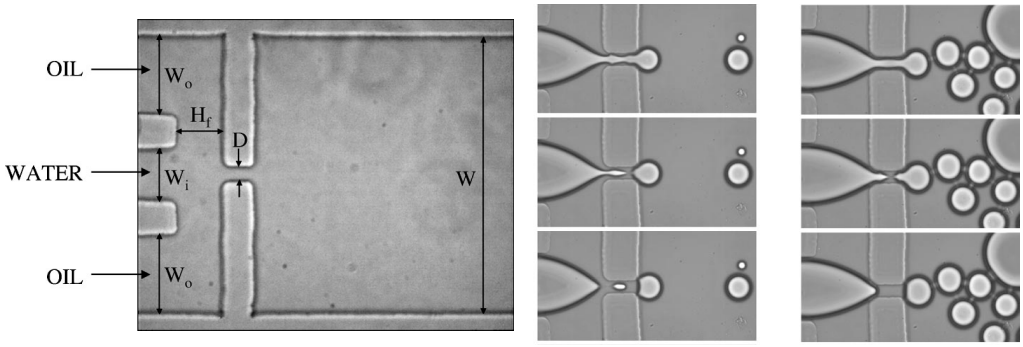

Figure 1.9: A "flow-focusing" geometry is used to produce water drops in oil. The right columns show different regimes that can appear for different forcing conditions. From Ref. [7].

1.3 Manipulating drops

In parallel to all of the fundamentals detailed above, the most important question remains how to manipulate drops in the microchannels in order to perform the necessary operations in a Lab-on-a-Chip (LOC). In a short review article, Joanicot and Ajdari [70] listed a few operations that were necessary in order for droplet microfluidics to live up to its promise. They list *fabrication, sorting, storage, fusion, breakup, and trafficking* as particular operations that must be performed on drops. They also distinguish, with reason, active from passive control, as well as distinguishing external controls from integrated droplet-level controls. Below, we will place in context the different control mechanisms, from the most basic to the most recent. We begin in this section with the two traditional approaches that have been used to provide some control: The microchannel geometry and the external flow variations, e.g. through syringe pumps.

1.3.1 Channel geometry

The channel geometry is the single most important element of the microfluidic control of droplets and this fact, though trivial, should always be kept in mind when designing control mechanisms. Very early on, it became clear that the geometry of the channel could be used to provide many actuation operations. We have already seen above how a zig-zag shaped channel can be used to mix the contents of a drop without any external interference [107] and how droplet formation depended on the geometry in which the drops are formed [46, 7]. Moreover, successive bifurcations were used to break initially large drops into a dense and monodisperse emulsion, as shown in Fig. 1.10 [82].

In these cases, the robustness of this control approach is due to the system functioning in a stable regime, meaning that a small uncertainty in the fabrication or the external control only leads to a small uncertainty in the result. Since nonlinearities are introduced by the presence of drops, for example during the pinch-off of a new drop [45], those can lead to unstable regimes in which the desired flow is not obtained. For instance, the breakup of drops in Fig. 1.10 may become unstable and the liquid may flow through only some branches, for certain operating conditions. This would be the case if the resistance when a drop enters the channel is decreased compared to the resistance of the channel

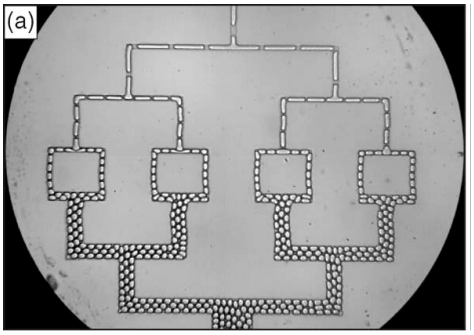

Figure 1.10: A cascade of bifurcations can be used to passively divide droplets into a monodisperse emulsion. From Ref. [82].

with a single phase [14, 51]. We have explored this possibility, which is described in Section 2.1.

The destabilizing effects can however be corrected by robust design of the geometry, for example by shunting two channels together at a location which depends on the distance between drops, in order to equilibrate the pressures in the two branches after the bifurcation [40].

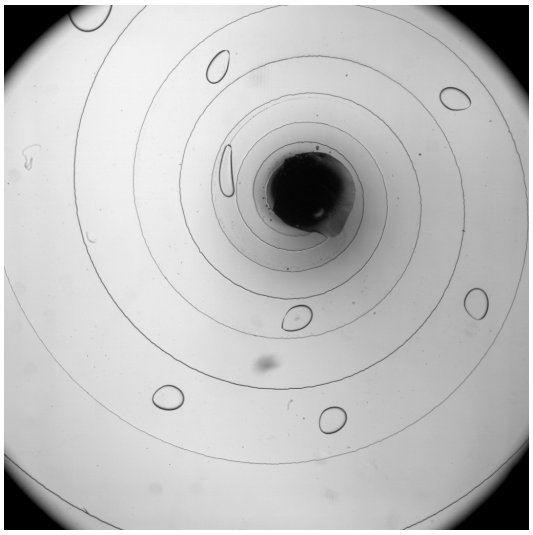

Figure 1.11: A spiral channel is used to impose both elongation and shear on flowing drops. See Section 4.1 for details.

Since the micro-fabrication methods allow any two-dimensional shape to be made, more subtle uses of the channel geometry to control the flow of drops has also been shown, for example in order to increase the space separating the drops or to move them closer together. This may be achieved by reducing or increasing the channel width. In Section 4.1, we will describe the use of circular shaped channels to submit drops to a constant shear, which can be used to elongate drops in a similar fashion to Taylor's four roll mill [117]. Figure 1.11 shows an early version of the experiment where a logarithmic spiral microchannel is used to produce progressively increasing shear and elongation on drops.

1.3.2 Imposed external flow

Along with the channel geometry, the second most important method for controlling droplet operations is by externally controlling the flow. Since most two phase flows in microchannels are produced either with positive displacement pumps (e.g. syringe pumps) or through a controlled pressure source, the magnitude of the forcing is a natural and powerful way to control the way drops are formed, broken, or transported. For instance, the size of drops that are produced in the flow-focusing junction of Fig 1.9 is mainly controlled by the relative flowrates of oil and water, in addition to the geometry of the focusing region. In this way, increasing the water flowrate will increase the size of the drops by "inflating" the drop more during the time that the neck is pinched off. Alternatively, varying the oil flowrate changes the time available for the water to flow and by the same token changes the size of drops thus produced.

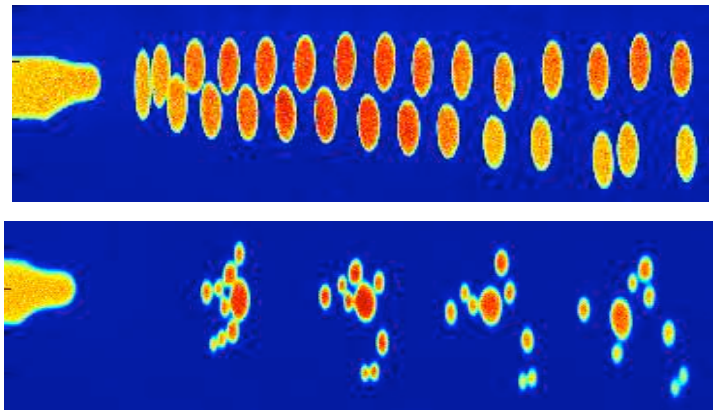

Figure 1.12: A snapshot showing water in oil drops being produced through a flow focusing device showing one drop per period (top) and nine drops per period (bottom). Experimental conditions for the top image: $Q_{oil} = 2$ μL/min and $Q_{water} = 0.5$ μL/min. Conditions for the bottom image: $Q_{oil} = 20$ μL/min and $Q_{water} = 2$ μL/min.

While this approach is very useful in practice, several issues must be kept in mind. The first is that changing the flowrates not only changes the drop size, it also changes the frequency at which they are produced and the velocity at which they travel. One would ideally like to control these parameters independently, particularly when the drop production is coupled with a complex microfluidic device downstream. Furthermore, variations in the flowrates can also produce changes in the flow regime, not only in the size of the drops. Some early measurements, made in our lab, showed that the number of drops produced at each breakup event could be varied by changing the flowrates of the external and internal fluids (oil and water, respectively), as shown in Fig. 1.12.

1.4 Active integrated manipulation

For droplets to be truly viable as Lab on a chip (LOC) vessels, global control through the means presented above will probably not be sufficient. For example, intelligent operations need to be performed based on the drop size, its contents, or other measurable quantities.

These operations can consist of sorting, merging, or dividing the drops asymmetrically. To this end, several approaches have been explored, involving different physical mechanisms.

1.4.1 Drops on an open substrate

It is important to take a small detour here to note that a second approach, parallel to the type of microfluidics we are talking about, has been developed for manipulating drops on a flat substrate or in suspension in a quiescent fluid. Two major categories of manipulation have taken shape. The first and most widely studied is based on using electrical forces to induce a force on the drop through electrophoresis, dielectrophoresis, or electro-wetting (see e.g. [95, 97, 119]). The second approach is to modulate the surface tension of the drop, through heat or chemistry, in order to produce an imbalance in surface stresses which in turn lead to motion [101, 42, 74, 41]. Other approaches were also explored, including the use of Surface Acoustic Waves (SAW) [126, 98], acoustic streaming [86], or optical tweezers [112, 27].

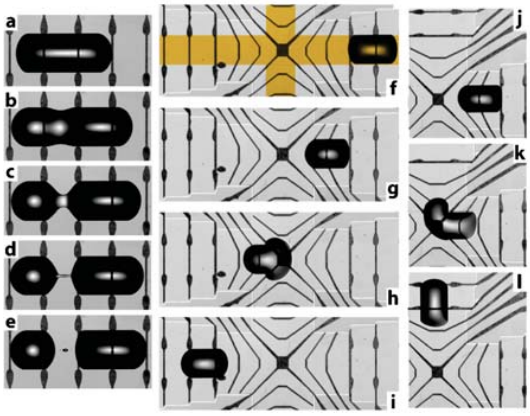

Figure 1.13: A microfabricated array of electrodes is used to manipulate drops on a solid substrate, from Ref. [42]. Drops are shown to move in a straight line, turn, and split

Different operations have been implemented regarding drops on a substrate, including forming, moving, dividing, and fusing drops, as shown in Fig. 1.13, where drops are manipulated using a set of patterned electrodes on the surface [42]. In this approach to manipulating droplets, the fundamental advantage is that each drop can be controlled at every moment, anywhere in the system. However, one loses in the process the helpful effect of geometry in applying standard operations on drops passively, which makes the manipulation much slower and more complex to implement. Furthermore, these systems also suffer from several issues which must be dealt with from a practical point of view such as sensitivity to surface contamination, contact angle hysteresis, and evaporation. Finally, it is not clear that these systems will allow the manipulation of volumes as small as those available for in-channel manipulation, to which we now switch.

1.4.2 Drops in a microchannel

Some of the same physical mechanisms have also been used to manipulate drops inside microchannels. Here, the focus has not been on manipulating a drop at any location and

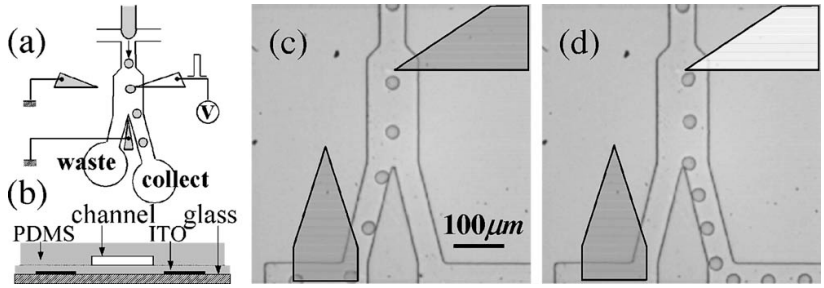

Figure 1.14: Drops of water flowing in an oil flow can be sorted either to the right or left outlet channels through dielectrophoretic forces [5].

at any time; the approach has been instead to allow the geometry to apply the large forces on the drops, passively, and augmenting this passive forcing with the dynamic actuation at particular locations in the microchannel. In this fashion, a train of drops can flow passively through the network of microchannels and intermittent forcing can be used when particular operations are necessary.

Of the operations that were listed by Joanicot and Ajdari, only sorting and fusion had been published by the end of 2006, both through the application of electrical forcing. In the first case, dielectrophoretic forces were shown to be sufficient to sort drops a few tens of microns in size, as shown in Fig. 1.14 [5]. Here, a 1kV power source was used to produce forces in the range of 10 nN, yielding a transverse velocity of about 1 cm/s for a drop 12 μm in diameter [5].

More recent implementations of this technique have shown that it is very easy to include the electrodes along with the fluidic channels, by fabricating a network of "channels" for the electrodes, in parallel to the fluidics, and filling them with a low melting point metal or conducting plastic. In this way, simply connecting the electrodes to an AC power source is sufficient for producing forces on drops. A second advantage of this technique is its rapid reaction time, shorter than 1 ms (the calculation in Ref. [5] is incorrect and underestimates the time to produce the force to a few μs). Note however that the dielectrophoretic force applied on a drop is a body force which decreases as R^3, as the drop radius R decreases.

The second operation that was demonstrated by 2006 was the fusion of drops [33, 4, 96]. The barrier to fusion is generally in the surfactant coverage of the interfaces which prevent the drainage of the lubrication film that separates the two drops. Priest *et al.* demonstrated that the "electrocoalescence" was due to a hydrodynamic instability of the interface, generated by the imposed electrical field. They also showed that two drops could be merged using a few volts and with a good selectivity even in a crowded flow, as shown in Fig. 1.15.

The combination of the two above operations with geometric forcing was sufficient for Raindance Technology, a startup spun out from the Weitz group at Harvard University, to begin its operations (`http://www.raindancetechnology.com/`). Although Raindance probably has a more complete tool set for manipulating drops, those tools have not been published. The remaining operations, namely the control of fabrication, storage, breakup or trafficking, remained unavailable until recently.

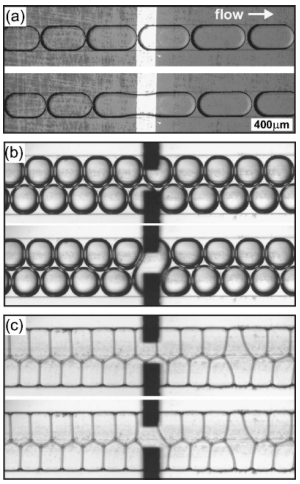

Figure 1.15: Electrocoalescence of droplet pairs in a crowded flow, from Ref. [96].

In this context, two papers originating from our lab were published in 2007 [12, 11] and provided an approach to control the formation and division, in addition to sorting, synchronizing, and fusing drops. The technique is based on inducing a Marangoni flow on the interface, whose net effect is to produce a force pushing the drop. More recently, we have also demonstrated more complex operations such as storing drops, reordering them, and trafficking them in a three-way exit [37]. This technique will be treated in detail in Chapter 3.

1.5 Manuscript organization

The rest of this document is organized as follows: We begin in the next chapter with our work on multiphase flows in complex geometries, treating the problems that we have looked at in chronological order. This is followed by two of the articles we have published on the subject. Chapter 3 then describes the main results on the technology we have developed for manipulating drops using a focused laser, also followed by two reprints on the subject. Finally, some more recent and unpublished work concerning the flow of drops in microchannels is presented.

Chapter 2

Drops in funny channels

Networks of channels are omnipresent in nature. When they are present in animals and plants, they serve the clear purpose of transporting matter (e.g. nutrients or oxygen) to and from organs, as shown for example in the networks of recent interest of Fig. 2.1. These naturally occurring networks can display a very wide range of sizes and can involve different physical interactions between the flowing fluid and the network walls. Furthermore, networks have different topologies and follow different scaling laws; while leaf venation forms a redundant network allowing several routes between two points, the tree itself provides no loops and no redundancies to reach a particular branch.

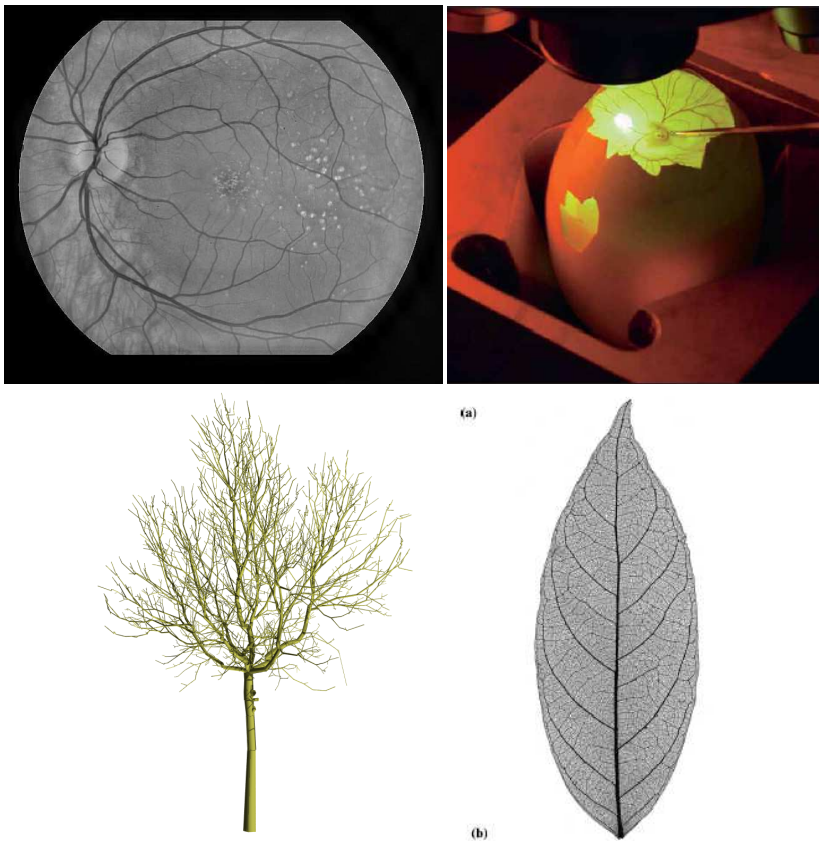

Figure 2.1: Four networks which transport nutrients: The blood circulation in the retina[1], the morphogenesis of the chicken circulatory network [120], a walnut tree [Matthieu Rodriguez, LadHyX], and a venation network in a tree leaf [20].

In other cases, such as for the flow in porous materials, the network representation is a simplification of a structure that may be too complicated to be generalized (see e.g. [26, 109]). In this case, the scientist's job is to produce a simplified representation that accounts for the transport processes in the porous medium while using a geometry that can be described quantitatively. Microfabrication techniques were introduced as an experimental tool to produce some model porous materials by Lenormand in the early 80's [80], as shown in Fig. 2.2, but have not been explored very extensively.

The network that initially motivated our work is the human lung's airway tree, generally modeled as a branching binary tree of circular tubes, as shown schematically in Fig. 2.3. On close inspection, the lung represents a fascinating object for a fluid dynamicist; it begins at the trachea whose diameter is about two cm, where flows reach

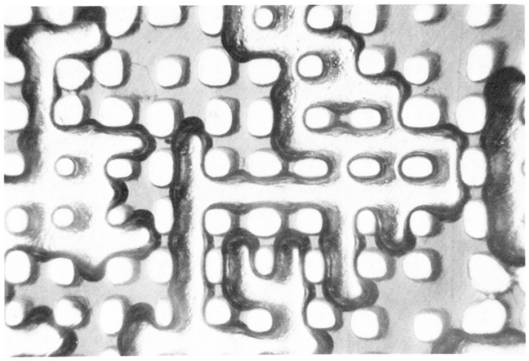

Figure 2.2: Liquid-gas menisci in a microfabricated model porous network, from Ref. [79].

Reynolds numbers of a few thousands and where the flow is typically turbulent. After a succession of bifurcations, the scale of each channel reaches a few millimeters (around generation 5), corresponding to low Re flows. The sizes decrease further until they reach a few hundred microns at the alveoli where the transport of oxygen becomes dominated by diffusion in a rarefied medium rather than by hydrodynamics [122].

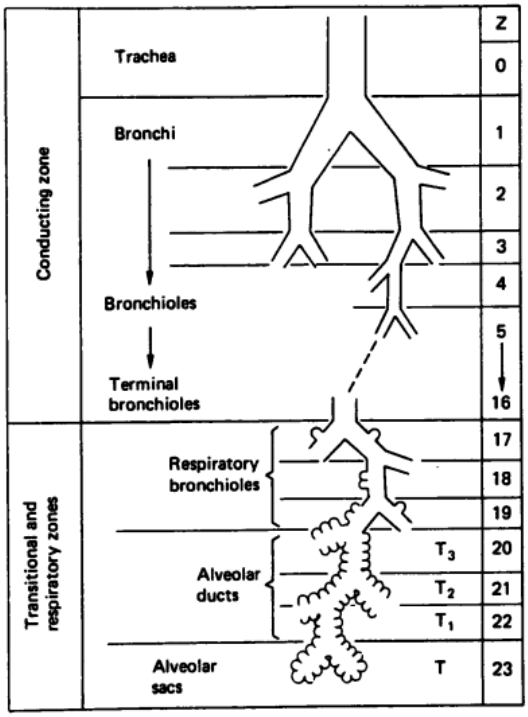

Figure 2.3: Classical image of the successive bifurcations in the human airway tree, from Ref. [122]

The story however is much more complex due to other interactions, of which we will note two: **(i)** The lung also undergoes large deformations during respiration and the flow interacts with the elasticity of the supporting structure. The deformability of the structures and the mechanical characteristics therefore have a major influence on the

distribution of the flow in the branched network. **(ii)** The airway walls are constantly lined with a liquid layer which plays important physiological roles, such as extracting inhaled contaminants or reducing the surface tension of the alveoli in order to prevent lung collapse. The liquid lining can interact with the flowing air in several ways, namely by forming liquid plugs that block the gas flow in the airways during disease.

Below, we will consider experimental models that explore multiphase flows in branching channels and which may involve interactions with elasticity. In doing so, we will also address some questions of interest in microfluidics regarding transport of drops and bubbles.

2.1 Flow of a low viscosity finger through a fluid-filled bifurcation

The results of this section were published in collaboration with Sedina Tsikata and Matthias Heil [14].

The first question we will ask is to know how a low viscosity fluid penetrates in a branched structure that is filled with a high viscosity immiscible fluid. The question of replacing one fluid with another of lower-viscosity is of obvious importance in the case of oil recovery, where high viscosity oil must be pumped out through a porous medium by water. In the case of physiological flows, this situation arises in the case of the first breath a baby takes at birth, where the liquid initially filling in the lung must be replaced with lower viscosity air. A similar situation also arises in the case of an air bubble that flows in the blood stream, for example as a treatment for cancerous regions [30].

A reduction of this problem to a tractable form can be made by considering the splitting of a low-viscosity finger, pushed at constant flowrate Q through a bifurcating channel. The situation is shown schematically in Fig. 2.4, along with the definition of terms used below. The question that will determine the filling of the network can be stated at the level of one bifurcation by asking whether the low viscosity finger will divide symmetrically or asymmetrically.

2.1.1 Linear stability analysis

A linear stability analysis can be made to determine the stability of the symmetric solution to small perturbations. In the case when the two daughter branches are open to the same exit pressure (e.g. atmospheric pressure), the stability arguments are similar to those used to justify the single finger selection in the Saffman-Taylor instability: Suppose that the fingers initially branch symmetrically but that the velocity of the finger in branch 1 increases slightly. This is equivalent to saying that the relative length of viscous fluid ahead of this finger decreases ($L_1 < L_2$), which in turn leads to the velocity difference increasing further, since finger 1 feels less resistance than finger 2. This is an unstable situation which implies that fingers branching into channels open to the atmosphere will always branch asymmetrically. If this bifurcation is one link in a binary network, the low viscosity finger will only open one path through the network, leaving most of the channels full of viscous fluid.

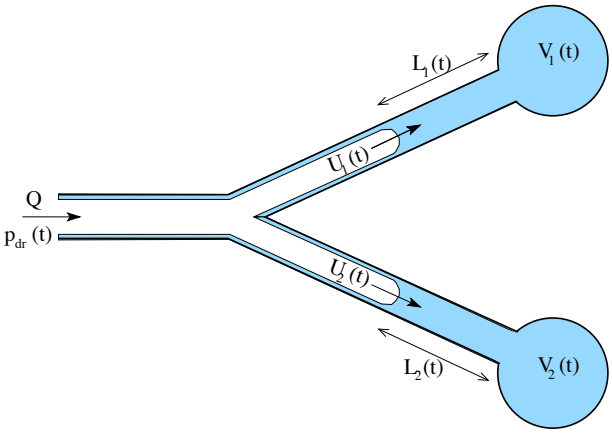

Figure 2.4: A low viscosity finger is pushed at constant flowrate Q and penetrates in a bifurcation filled with a high viscosity immiscible fluid. $L_{1,2}$ denote the length of viscous fluid ahead of the finger, and $U_{1,2}$ the velocities in each branch.

In the case of pulmonary flows, one expects that some mechanism might stabilize the symmetric branching pattern so we consider the role of the lung's elasticity, by lumping the elastic effects into a compliant chamber at the downstream end of each of the daughter branches. The linear stability analysis should now be done carefully. We sketch the main steps below, the details being available in Ref. [14] at the end of this chapter.

In each of the daughter tubes, the pressure drop across the occluded section has three components: **(i)** the Poiseuille pressure drop ahead of the finger tip, $\Delta p_{\texttt{pois}} = \mu \mathcal{R} L_i(t) Q_i(t)$, where the flow resistance $\mathcal{R}$ depends on the tube's cross-section [123]; **(ii)** the pressure drop across the curved tip of the finger, $\Delta p_{\texttt{tip}} = \mathcal{C}(U_i)$, where the function $\mathcal{C}(U_i)$ accounts for the radius of curvature which depends on the velocity of the finger [24, 62]; **(iii)** the pressure $p_{\texttt{elast}}$ in the chambers at the end of the daughter tubes. Provided the membranes that close the (otherwise rigid) chambers are elastic, $p_{\texttt{elast}}$ depends only on the chambers' instantaneous volume and we assume that $p_{\texttt{elast}\,i}(t) = k \int_0^t Q_i(\tau) d\tau + p_{0i}$, where k is an elastic constant and p_{0i} is the pressure in chamber i at time $t = 0$.

Assuming that the viscous pressure drop in the fingers can be neglected, the fingers in both daughter tubes are subject to the same driving pressure $p_{dr}(t)$, and we have

$$p_{dr}(t) = \mathcal{C}(U_i) + \mu \mathcal{R} L_i(t) Q_i(t) + k \int_0^t Q_i(\tau) d\tau + p_{0i} \quad \text{for} \quad i = 1, 2, \tag{2.1}$$

where $Q_i(t) \simeq A\, U_i(t)$, the approximation sign accounting for the fact that there is a liquid film left on the surfaces.

The linear stability analysis can be performed by first differentiating Eq. (2.1) with respect to time and expanding it in terms of the driving pressure. The zero-th order term simply states the conditions for the symmetric solution, for which we can write $L_i(t) = l_0 - \mathcal{U} t$, where $\mathcal{U}$ represents the symmetric solution velocity.

We determine the stability of this solution by writing the velocities as $U_i(t) = \mathcal{U} + \epsilon \widehat{U}_i(t)$, where $\epsilon \ll 1$, with similar expansion for all other quantities. We further simplify the problem by assuming that the capillary jump at the interfaces will not affect the stability, which allows us to write the condition for stability

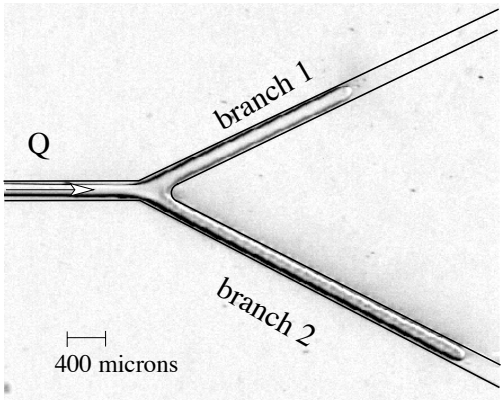

Figure 2.5: Experimental image of the splitting finger at a bifurcation.

$$\int_{\widehat{U}_i(t=0)}^{\widehat{U}_i(t)} \frac{du}{u} = \int_0^t \frac{2\mathcal{U} - k/(\mu\mathcal{R})}{l_0 - \mathcal{U}\tau} d\tau. \tag{2.2}$$

If the right hand side of (2.2) is negative, the perturbation velocities $\widehat{U}_i$ decay, indicating that the symmetrically branching solution is stable. The denominator of the integrand on the right hand side represents the instantaneous length of the fluid-filled part of the daughter tubes and is therefore always positive. Perturbations to the symmetrically branching finger will therefore grow if $\mathcal{U}$ exceeds the critical value $U_c = k/(2\mu\mathcal{R})$. Hence at small velocities, when the flow resistance is dominated by the vessel stiffness, the finger will branch symmetrically. Conversely, at large finger velocities, the resistance to the flow is dominated by the viscous losses and the propagating finger will tend to open a single path through the branching network.

2.1.2 Experimental realization

Experiments were conducted in PDMS microchannels by bonding thin PDMS membranes on top of the exit holes. The channels were initially filled with silicone oil v100 ($\mu = 0.1$ Pa s) and fingers of perfluorodecalin (PFD, viscosity $\mu_{\mathtt{pfd}} \simeq 5 \cdot 10^{-3}$ Pa s) were injected towards the bifurcation at constant flowrate by using a syringe pump. The finger tip positions were located on microscopy images, as shown in Fig. 2.5, and the velocities in each branch were calculated from successive images. In this way, the difference between the velocities of the two fingers were measured as a function of time.

Figure 2.6 shows the evolution of the finger velocity difference as a function of time, for different flowrates Q. The experimental data display a non-zero velocity difference for all flow rates, indicating that the symmetric solution does not necessarily correspond to a zero velocity difference. However, fingers forced at low flowrate show a constant velocity difference while $(U_1 - U_2)$ continuously grows for fingers forced at high flowrate, indicating a transition from symmetric to asymmetric splitting.

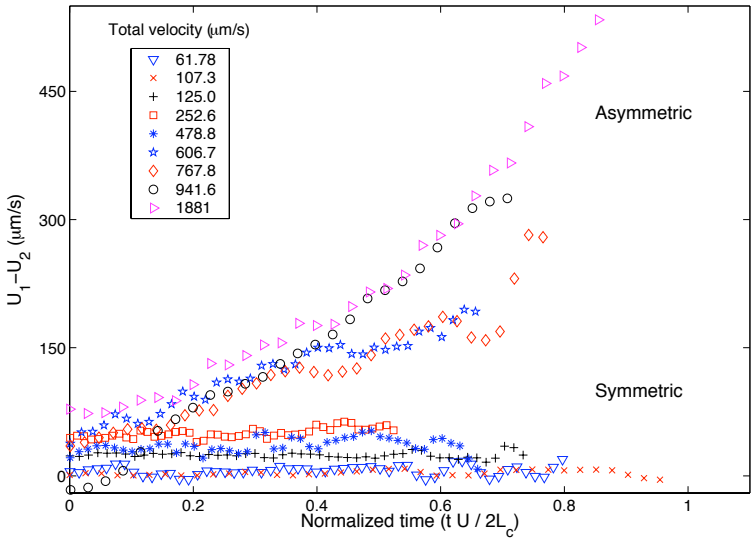

Figure 2.6: Velocity difference in two daughter branches as a function of time. $U_1 - U_2$ is found to continuously increase for $\mathcal{U} > 479$ μm/s, in agreement with the theoretical prediction.

The agreement between experiment and theory is verified by calculating the critical value of the capillary number, using thin shell theory for the chamber stiffness k. Using physical values estimated from the experiments, we calculate the predicted critical capillary number at $\mathrm{Ca}_c = 5 \times 10^{-4}$, which compares favorably with the experimental transition which was observed in the range $4.78 \times 10^{-4} < \mathrm{Ca} < 6.06 \times 10^{-4}$.

2.2 Flow of a plug in a straight channel

The work presented in Sections 2.2 and 2.3 was published in collaboration with Cédric Ody and Emmanuel de Langre [91].

A more common occurrence in pulmonary pathologies is the presence of plugs of liquid that can occlude an airway locally. These plugs can form through the destabilization of the lung's liquid lining through an process similar to the Plateau-Rayleigh instability [47]. They are especially observed in diseases such as asthma, when the diameter of the channels is reduced due to inflammation, or bronchiolitis in children's lungs. Plugs can also be injected into the lung in order to deliver treatment to the distal alveoles, as in the case of Surfactant Replacement Therapy (SRT). During this procedure, surfactant is injected as a plug into a premature baby's lungs in order to replace the molecules that have not formed naturally [52, 31], with the aim to deliver the liquid as far down in the airway tree as possible.

In parallel, many questions remain on the transport of multiphase flows in microchannels, as discussed in Chapter 1. We therefore set up an experimental study to understand the relationship between the driving pressure and the velocity at which a plug of length L_0 travels in a straight microchannel with rectangular cross-section.

The experimental setup consisted of a Y-shaped junction in which plugs of PFD were formed, as shown in Fig. 2.7, connected to a straight channel. The contact angle

between the PFD and the PDMS is small and we consider that the fluid is perfectly wetting in our analysis. The size and position of the plugs as a function of time were measured for different driving conditions, using high-speed video microscopy.

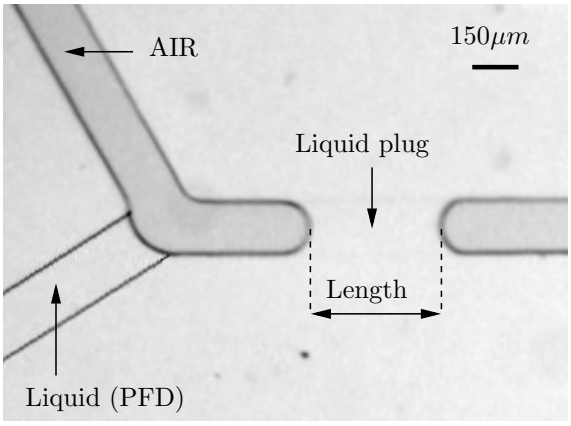

Figure 2.7: Formation of a plug in a microchannel. Air is forced at a constant pressure while a controlled length of liquid is injected from a syringe pump.

2.2.1 Model

Given a constant driving pressure P_{dr}, the steady-state pressure balance across the plug is

$$P_{dr} = \Delta P^r_{cap} + P_{visc} + \Delta P^a_{cap}, \tag{2.3}$$

where ΔP^r_{cap} and ΔP^a_{cap} express the capillary pressure drops at the receding and advancing interfaces of the plug, respectively, while P_{visc} represents the viscous dissipation occurring in the bulk. Using Poiseuille's law, the latter is expressed as

$$P_{visc} = \alpha \mu L_0 U_0, \tag{2.4}$$

with α a dimensional coefficient corresponding to the geometry of the channel. For a rectangular geometry [110], α may be approximated as

$$\alpha \simeq \frac{12}{b^2}\left[1 - 6\frac{2^5 b}{\pi^5 w}\right]^{-1}. \tag{2.5}$$

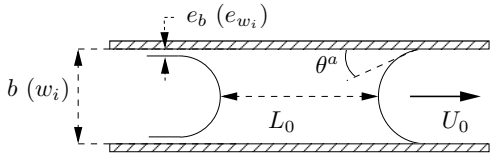

Figure 2.8: Sketch of a plug propagating from left to right in a two-dimensional channel.

When the plug is at rest, static values of ΔP^r_{cap} and ΔP^a_{cap} are given by Laplace's law as $\Delta P^r_{cap} = -\Delta P^a_{cap} = \gamma\kappa$, where $\kappa \simeq 2\left(b^{-1} + w^{-1}\right)$ is the mean curvature of each interface at rest. When the plug is moving, the front and rear curvatures are modified as sketched in Fig. 2.8. At the front interface, the balance between friction and wetting forces at the vicinity of the contact line leads to the existence of a non-zero dynamic contact angle and this flattening of the advancing interface increases the resistance to the motion. By assuming that θ^a has the same value in the two sections, the dynamic capillary pressure drop for the front interface becomes

$$\Delta P^a_{cap} = -\gamma\kappa\cos\theta^a. \tag{2.6}$$

The relation between the contact angle and the velocity of the contact line is known through Tanner's law [19, 63] which states that

$$\theta^a = (6\Gamma \mathrm{Ca})^{1/3}, \tag{2.7}$$

where Γ is a prefactor ($\Gamma \simeq 5$) that accounts for the singularity occurring at the contact line [44].

Using Eq. (2.7) and taking the leading-order term in the Taylor expansion of $\cos\theta^a$ in Eq. (2.6), the front pressure drop becomes

$$\Delta P^a_{cap} \simeq \gamma\kappa\left(-1 + \frac{(6\Gamma \mathrm{Ca})^{2/3}}{2}\right). \tag{2.8}$$

At the rear interface, a thin film is deposited at the channel walls [24], which reduces the rear meniscus radius and thus also increases the resistance to the motion. The dynamic capillary pressure drop at the rear interface may then be written as

$$\Delta P^r_{cap} = \gamma\left(\frac{1}{b/2 - e_b} + \frac{1}{w/2 - e_w}\right), \tag{2.9}$$

where we denote e_b and e_w the thicknesses of the deposited film at the rear of the plug in the thickness and plane sections respectively.

Bretherton's law expresses the thickness e of the deposited film at the rear of a plug as a function of the capillary number Ca and the radius R of a circular capillary tube [19]:

$$e/R = 3.88\mathrm{Ca}^{2/3}. \tag{2.10}$$

Assuming Bretherton's law to be valid in both directions of the rectangular cross section, i.e. $2e_b/b = 2e_w/w = 3.88\mathrm{Ca}^{2/3}$, the rear capillary jump is obtained from Eq. 2.9 as

$$\Delta P^r_{cap} = \gamma\kappa\left(1 + 3.88\mathrm{Ca}^{2/3}\right). \tag{2.11}$$

Finally, by using Eqs. (2.4), (2.8) and (2.11), one derives

$$P_{dr} \simeq \alpha\eta L_0 U_0 + \gamma\kappa\beta\mathrm{Ca}^{2/3}, \tag{2.12}$$

where $\beta = 3.88 + (6\Gamma)^{2/3}/2$ is a nondimensional coefficient obtained from Bretherton's and Tanner's laws.

Equation (2.12) governs the dynamics of a plug of length L_0 moving steadily at speed U_0 in a straight rectangular channel for a constant driving pressure. It can be nondimensionalized by comparing it with the capillary pressure jump $\gamma\kappa$, and we obtain

$$\overline{P_{dr}} \simeq \overline{\alpha}\mathrm{Ca} + \beta\mathrm{Ca}^{2/3}, \tag{2.13}$$

with $\overline{P_{dr}} = P_{dr}/(\gamma\kappa)$ the nondimensional driving pressure and $\overline{\alpha} = \alpha L_0/\kappa$ is the nondimensional length.

2.2.2 Comparison with experiment

A typical experimental velocity vs. length curve is shown in Fig. 2.9 for a particular driving pressure ($P_{dr} = 250$ Pa). The nonlinear dependence of the velocity on the inverse length is evident when the experimental data are compared with the dashed line which represents the prediction for purely viscous flow. This viscous law approximates the travel velocity well for long plugs, i.e. $L_0 \gg w$, but the difference increases as the length of the plug decreases and the losses at the interfaces become the dominant mechanism. The solid line is fitted from Eq. (2.13), using β as a fitting parameter. It yields a value of β that is consistent with the values obtained in the literature for different geometries [19].

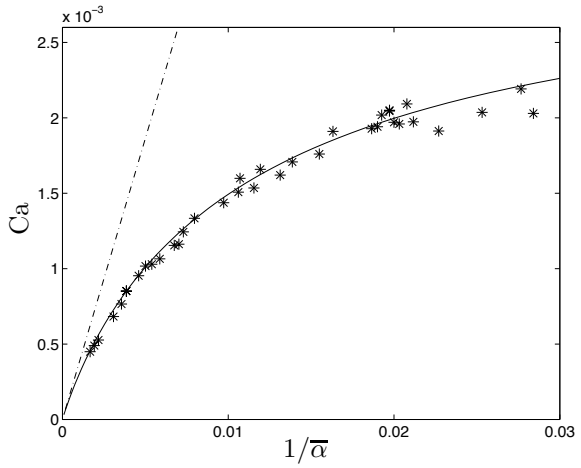

Figure 2.9: Capillary number vs. the inverse plug length. The dashed line shows the Poiseuille law and the continuous line indicates the relation (2.13).

The significance of this result for microfluidics lies in the transport of drops and bubbles. It has been noted by several groups that the presence of drops increases the resistance to flow in a microchannel [3, 56, 104], though no clear mechanism has been described for this increased pressure drop. By looking at the space between the drops rather than the drops themselves, one begins to understand the contribution of the interface deformation on the pressure balance across a train of drops. Although this mechanism does not account for other effects such as flow in the corners or Marangoni retardation, it explains the characteristic "bullet" shape that is often published, which is clear evidence that the change in shape of the front and rear interfaces plays at least a partial role in retarding droplet traffic.

2.3 Flow of a plug in a bifurcation

We now consider a plug flowing through a bifurcation with right angles: a T-junction. We characterize the behavior of this plug for different driving pressures and initial plug lengths, L_0, measured in the straight channel upstream of the bifurcation. Three different behaviors may be observed, as described below.

2.3.1 Blocking

The first feature we can extract is the existence of a threshold pressure P_{thresh} (between 200 & 300 Pa for our experiments) which does not depend on the initial length of the plug. For $P_{dr} < P_{thresh}$, the plug remains blocked at the entrance of the bifurcation as shown in Fig. 2.10, which shows the equilibrium positions of a plug for two distinct pressures, $P_{dr} = 100$ Pa & $P_{dr} = 200$ Pa. While the rear interface has the same shape in both cases, the front interface adapts its curvature to balance the applied pressure, keeping its extremities pinned at the corners of the bifurcation.

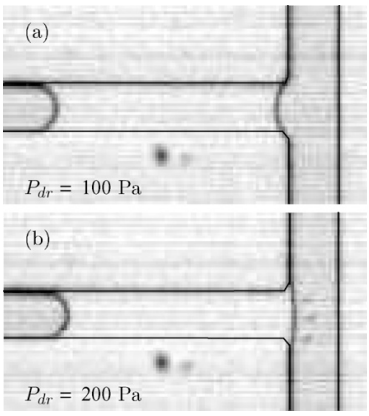

Figure 2.10: Blocking of the plug at the entrance of the T-junction for two distinct pressures with $P_{dr} < P_{thresh}$. The front interface is pinned at the corners of the bifurcation and adapts its curvature to the applied pressure. The shape of the rear interface is independent of P_{dr}.

This simple result can nevertheless be of major importance in the case when the bifurcation is one link in a network, in which case the distribution of pressures may be such that we are below the threshold value locally, even for a large global driving pressure.

2.3.2 Rupture

When the pressure exceeds P_{thresh}, the plug continues its propagation through the bifurcation. If the plug is short, its rear interface catches up with its front interface before the latter reaches the opposite wall. The plug then ruptures, opening the outlet branches of the T-junction to air. A typical sequence of plug rupture is shown in Fig. 2.11. Eventually, the liquid that remains on the channel walls drains slowly through the action of capillary forces and air drag.

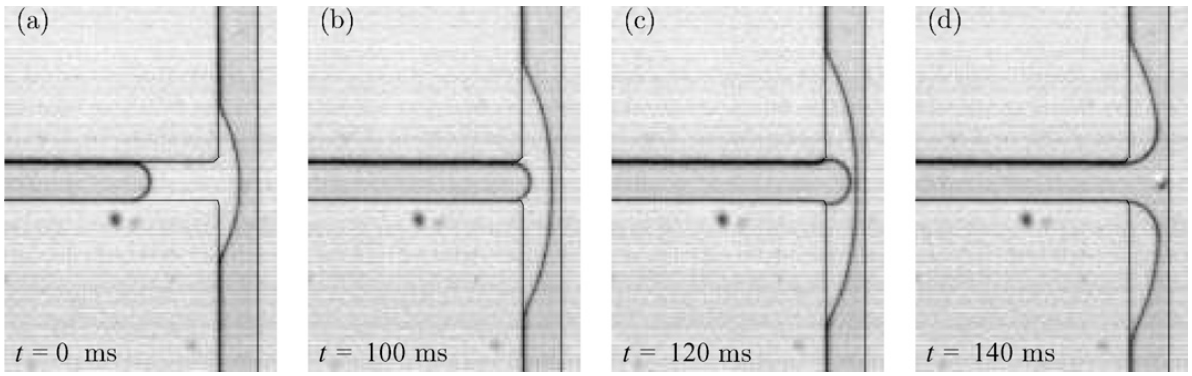

Figure 2.11: Sequence of plug rupture. The plug ruptures in the T-junction, leaving liquid on one side of the outlet channel, and air can flow freely from the pressure source.

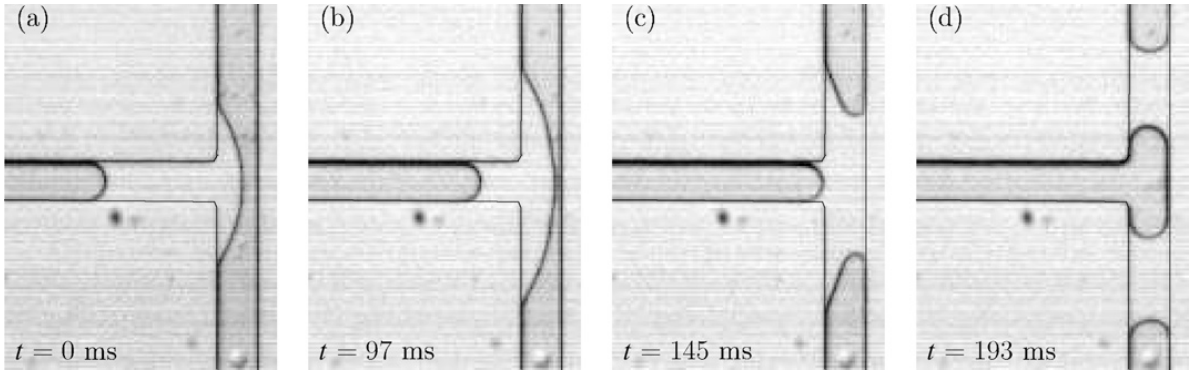

Figure 2.12: Sequence of plug splitting at the T-junction. Splitting leads to symmetric formation of two daughter plugs in the outlet branches of the T-junction.

2.3.3 Splitting into two daughter plugs

When the plugs are sufficiently long that the front interface reaches the opposite wall, two daughter plugs of equal length are formed through a splitting of the initial one, as shown in Fig. 2.12. As soon as the liquid reaches the wall, the transport dynamics becomes dominated by the wetting forces acting between the liquid and solid. These forces act to draw the liquid very rapidly into contact with the wall, as observed between the images (b) and (c) of Fig. 2.12. In part (c), we see that the curvature is not constant along the liquid surface, implying the existence local pressure gradients which pull the liquid into the daughter branches. These wetting forces are dominant compared to the driving pressure, as seen by the rapidity of the advance once the plug has touched the wall.

Note that before rupture or splitting, the evolution of the plug in the bifurcation is similar in both cases: the front interface advances without constraints while the extremities of the rear interface remain pinned by the corners of the bifurcation until process of rupture or splitting is achieved (Fig.2.11-c).

The three behaviors can be summarized in the phase diagram of Fig. 2.13 as a function of plug length and driving pressure. Below, we will develop a physical picture corresponding to the transitions between the three regions.

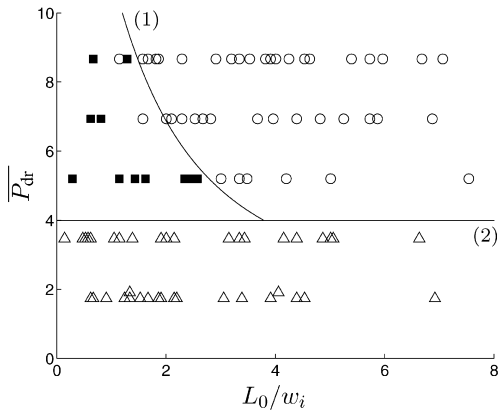

Figure 2.13: Phase diagram showing the breaking □, splitting ∘, and blocking △ regimes. The lines correspond to the theoretically predicted values. The solid lines correspond to the theoretical model developed in the text.

2.3.4 Modeling the transitions

The two parameters that determine the transitions between the three behaviors observed above are plug length and forcing pressure. First, the transition between the blocking and flowing can be understood by writing a pressure balance on the two sides of the plug as it passes the bifurcation, while taking into account the change in curvature at each interface. If we assume that the front interface remains pinned to the corners, we can write the maximum capillary pressure that must be overcome which corresponds to a radius of curvature equal to $w/2$, where w is the width of the entrance channel. In this case, the threshold pressure can be written as

$$P_{thresh} = \frac{4\gamma}{w}, \tag{2.14}$$

which is shown by the solid line (2) on Fig. 2.13.

In order to understand the transition between splitting and rupture, we consider the critical case in which the rear interface catches up with the front interface exactly at the moment when the front interface reaches the opposite wall, as shown in Fig. 2.14(b). In this case, we may reduce the problem to a geometric one in which all the parameters are fixed by the channel design, except the contact angle at the front interface (point E). This angle contains the physics of the problem, since it varies with the velocity of the advancing interface, through a visco-capillary balance.

By assuming that the angle variations are given by Tanner's law as for the case of a straight channel, one may again obtain the relation between the pressure drop and the liquid velocity. This relies on an evaluation of the viscous contribution, which must be estimated since the details of the flow field are unknown. However, a mean value corresponding to gross averaging of the length and velocity of the fluid can be used to yield a relation that uniquely relates the driving pressure and the contact angle. The critical volume to reach the configuration of Fig. 2.14(b) can therefore be computed as a function of driving pressure. This prediction corresponds to the line (1) on Fig. 2.13 and agrees well with the experimental observations.

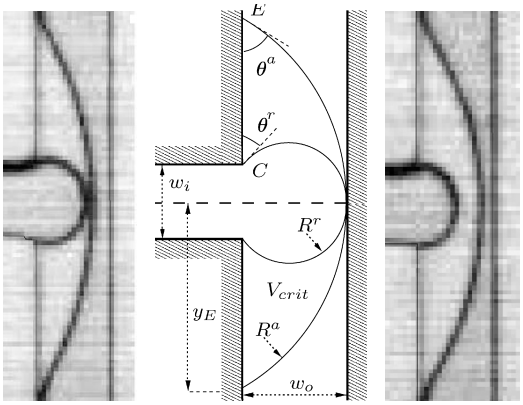

Figure 2.14: Shape of the plugs before **(a)**-rupture and **(c)**-splitting. -**(b)** Schematic of a plug of volume V_{crit} situated on the theoretical boundary between rupture and splitting where front and rear interfaces of a plug meet at the wall.

2.4 Parallel channels

This work was done in collaboration with Jean-Baptiste Masson and Xin Wang [15].

Most recently, we addressed questions of collective behavior that comes about through capillary interactions at the exit of parallel channels. In particular, we looked at the flow of an oil interface exiting from a thin channel into a sudden expansion for three microchannel geometries: (a) Flow through a single channel, (b) through two parallel channels, or (c) through seven parallel channels.

This work was motivated by the desire to understand the flow through a simple porous medium, in which a viscous fluid exits through adjacent pores and spreads while being submitted to a visco-capillary balance. The collective effects of flow through parallel pores can thus be explored and compared with single pore models.

The base state which corresponds to the flow through a single channel is shown in fig. 2.15(inset), which shows a superposition of the interface shape at successive times. Two important facts may be observed from these experiments: First, the visco-capillary balance is verified throughout the experiment, which is shown by measuring the flowrate as a function of time. Indeed, the channel dimensions were chosen such that the main pressure drop occurs in the long and thin "impedance" channel, which yields a constant flowrate at late times. However, the capillary effects are significant at intermediate times (at $t = 2$ s in Fig. 2.15), where a dip in the flowrate appears due to the large curvature which resists flow.

Second, the interface displays a parabolic, rather than circular shape. This "lubrication limit" has been predicted in imbibition studies [93], although the physical origin and the applicability of the lubrication limit in our particular geometry are not yet fully understood. The parabolic shape may be verified by measuring the maximum width transverse to the flow direction, dx, and the position of the apex in the flow direction z_m. The dependence of z_m with dx is linear for the case of a parabolic interface, as verified by the circles in Fig. 2.16.

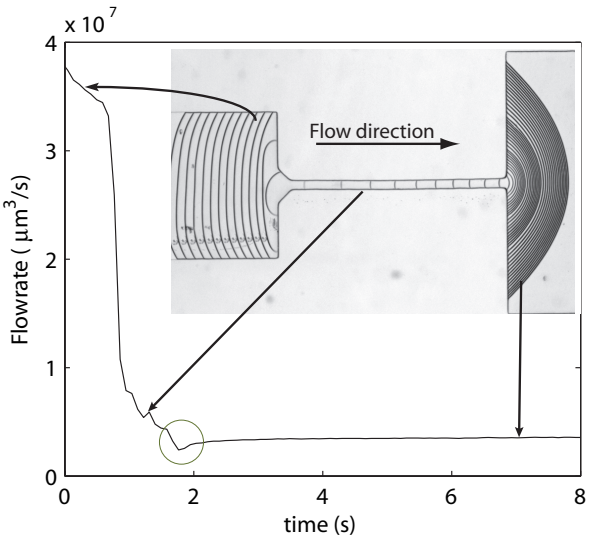

Figure 2.15: Evolution of the flowrate as the fluid exits through a single channel. The driving pressure is $P_{dr} = 785$ Pa. The image shows the location of the oil interface at a succession of times. For clarity, the time step used in the display is dilated as the liquid exits the channel, as seen by the apparent jumps in the interface position. The time step is $dt = 0.1$ s for the first period, $dt = 0.2$ s for the second, and $dt = 0.4$ s for the third.

Next, this base state is compared with the flow through two parallel channels separated by a distance of $d = 200$, 300, or 500 μm. Through similar measurements of the interface shape and position (Fig. 2.16), we uncover the existence of three regimes:

1. At early times, the two separate drops act as independently advancing droplets. This is confirmed in Fig. 2.16(b) where the $z_m(dx - d)$ shows exact collapse of the data for different channel separations.

2. When the two drops begin to interact, a very rapid merging event occurs, which we do not resolve with our experiments, followed by a slower relaxation to the parabolic shape. This relaxation occurs through the redistribution of the flow into the central region between the two exiting droplets. It is also associated with a temporary increase in the total flowrate. In Fig. 2.16(a), the merging event corresponds to the kink in the curves, meaning that the transverse flow is strongly reduced compared to the flow in the axial direction.

3. Finally, a parabolic evolution similar to the case of the single channel is recovered at late times. The time taken to reach the parabola can be predicted by visco-capillary analysis and scales as d^3, which is verified in the experiments.

The interface shape before, during, and after the merging can be seen in Fig. 2.16(c), which gives a visual verification of the global quantities discussed above.

The transient state plays a major role in the case of n parallel channels, as shown in Fig. 2.17, which shows a superposition of images corresponding to the flow through seven parallel channels. While the early and late times reflect again the results obtained in the two-channel case, we observe that the mergings happen mainly on a two-by-two

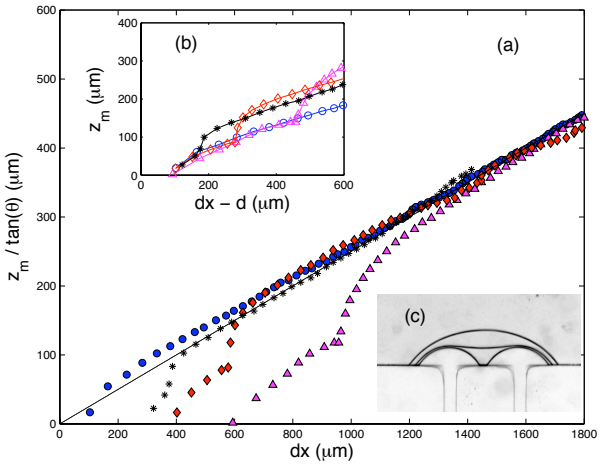

Figure 2.16: (a) Evolution of the modified maximum position ($z_m/\tan(\theta)$) with respect to the lateral width of the interface (dx) for a single channel ($\circ$) and for two channels separated by 200 μm ($*$), 300 μm ($\diamond$), and 500 μm ($\triangle$). The straight line represents $z_m = dx/4$. (b) Same data with the inter-channel distance (d) subtracted. (c) The interface before, during, and after the transition.

basis among exiting drops. This is due to the interactions between adjacent droplets which, when they merge, redirect the fluid to the space between them, thus temporarily preventing further mergings from occurring. For this reason, the transition between n independent drops and a single parabolic shape occurs through a cascade of binary mergings and relaxations. This implies that the channel doublet is the fundamental building block which may be generalized to any number of total channels.

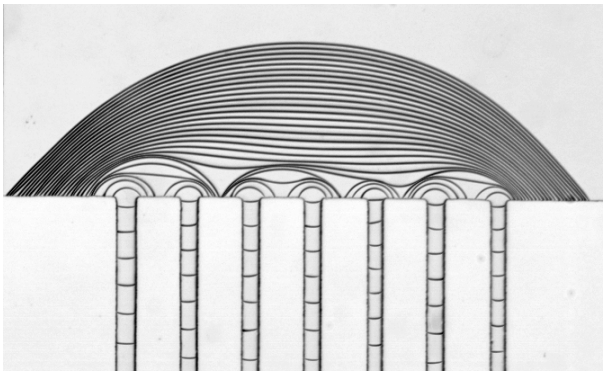

Figure 2.17: Advance of an interface through seven independent channels. The time separating each line is 0.1 s.

J. Fluid Mech. (2006), *vol.* 546, *pp.* 285–294.
doi:10.1017/S0022112005007287 Printed in the United Kingdom

The propagation of low-viscosity fingers into fluid-filled branching networks

By CHARLES N. BAROUD[1], SEDINA TSIKATA[1] AND MATTHIAS HEIL[2]

[1]Laboratoire d'Hydrodynamique (LadHyX), Ecole Polytechnique, 91128-F Palaiseau Cedex, France
[2]School of Mathematics, University of Manchester, Manchester, M13 9PL UK

(Received 12 January 2005 and in revised form 20 June 2005)

We consider the motion of a finger of low-viscosity fluid as it propagates into a branching network of fluid-filled microchannels – a scenario that arises in many applications, such as microfluidics, biofluid mechanics (e.g. pulmonary airway reopening) and the flow in porous media. We perform experiments to investigate the behaviour of the finger as it reaches a single bifurcation and determine under what conditions the finger branches symmetrically. We find that if the daughter tubes have open ends, the finger branches asymmetrically and will therefore tend to reopen a single path through the branching network. Conversely, if the daughter tubes terminate in elastic chambers, which provide a lumped representation of the airway wall elasticity in the airway reopening problem, the branching is found to be symmetric for sufficiently small propagation speeds. A mathematical model is developed to explain the experimentally observed behaviour.

1. Introduction

Flows in which a finger of low-viscosity fluid propagates into a tube and displaces another fluid of larger viscosity are of relevance in many applications, such as oil extraction (Homsy 1987), microfluidic devices for droplet transport (Link *et al.* 2004) and pulmonary biomechanics (Gaver, Samsel & Solway 1990).

For instance, many respiratory diseases, such as respiratory distress syndrome, may cause the occlusion of the pulmonary airways with viscous fluid. Occluded airways are believed to be reopened by a propagating air finger, in a process that involves a complicated interaction between a viscous free-surface flow and the deformation of the elastic airway wall. The mechanics of airway reopening in an individual airway have been investigated by many authors (e.g. Gaver *et al.* 1990; Hazel & Heil 2003), but these studies ignore the fact that the pulmonary airways branch frequently. This raises the question of whether the propagating air finger will reopen the entire pulmonary tree or simply follow a single path, keeping most of the lung occluded. (Cassidy, Gavriely & Grotberg (2001) performed experiments to determine how short liquid plugs propagate through rigid bifurcations.) The question is also of relevance in 'gas embolotherapy', a novel technique aimed at starving tumour cells of their blood supply (see Calderon & Bull 2004).

Similar questions arise in microfluidic technology. Many microfluidic devices are designed to transport samples of fluid through complicated networks of channels in order to perform chemical or bio-chemical tests (Song, Tice & Ismagilov 2003). The use of drops as vehicles for the transport offers many advantages, such as

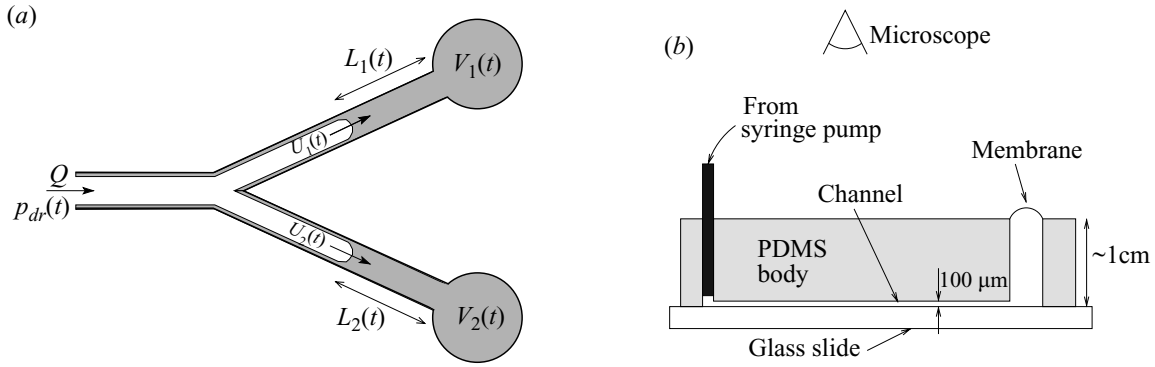

FIGURE 1. (*a*) Model problem: low-viscosity fluid is injected into a branching tube. The propagating fingers displace some of the more viscous fluid that initially filled the tube; the remaining viscous fluid is deposited on the tube walls. The two daughter tubes are terminated by large elastic chambers. (*b*) Sketch of the experimental set-up (not to scale). The total volume of fluid contained in the channel is approximately 0.5 μl while the volume in the end chambers is approximately 50 μl.

the control of dispersion and wall contact, as well as the possibility of activating chemical reactions at controlled locations, e.g. through droplet merging. Other uses of bubbles and drops in microfluidics include the production of controlled micro-emulsions through the breakup of long bubbles as they advance through a branching network of microchannels (Link *et al.* 2004). It is therefore important to understand the dynamics of the drop transport in order to predict the path and the breakup of individual drops.

Here, we study these questions at the level of a single bifurcation and consider the model problem shown in figure 1(*a*). A finger of low-viscosity fluid propagates along a parent tube which branches into two daughter tubes which have identical cross-sections. The finger is driven by the injection of fluid at a constant flow rate, Q, and displaces a viscous fluid of viscosity μ which is much larger than the viscosity of the finger. We denote the surface tension between the two fluids by σ. The daughter tubes terminate in two large elastic chambers which provide a lumped representation of the wall elasticity in the pulmonary airways. We wish to establish the conditions under which the finger continues to propagate symmetrically along the two daughter tubes once it has passed the bifurcation.

2. Experimental set-up

We performed experiments using the set-up sketched in figure 1(*b*). A Y-shaped channel of rectangular cross-section ($W \times H = 200\mu\text{m} \times 100\,\mu\text{m}$) was fabricated using standard microfluidic soft lithography methods (Quake & Scherer 2000). A mould was made by etching a 100 μm layer of photoresist on the surface of a silicon wafer. The mould was then covered with a thick layer of liquid poly(dimethylsiloxane) (PDMS) which was allowed to solidify before we created cylindrical chambers at the ends of the three branches: a thin hole at the end of the parent branch for the fluid injection, and two larger end chambers (holes with 1.6 mm radii) at the ends of the two daughter channels. The large end chambers were sealed with thin elastic membranes of thickness $h = 50\,\mu\text{m}$, also made of PDMS (Young's modulus $E \simeq 9 \times 10^5\,\text{N m}^{-2}$ and Poisson's ratio $\nu = 0.5$). Finally, the PDMS block was bonded onto a glass microscope slide.

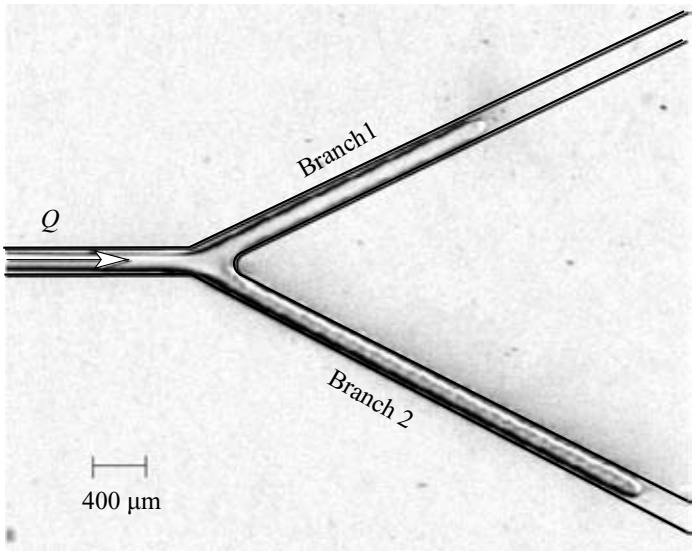

FIGURE 2. Snapshot of the branching finger. The positions of the two tips are recorded over a sequence of successive images, allowing the velocity of the fingers to be determined.

The experiments were conducted by first filling the channels with silicone oil (viscosity $\mu = 100\,\mathrm{cP}$) until the end membranes were taut. PDMS is permeable to gas, therefore the air that initially filled the channels could escape through the thin membranes when the silicone oil was injected. After the membranes were slightly pre-stretched, a finger of perfluorodecalin (PFD; viscosity $\mu_{PFD} = 2.9\,\mathrm{cP}$) was injected. This was done using a syringe pump with a 100 μl glass syringe, at flow rates in the range 1–60 $\mathrm{nl\,s^{-1}}$, resulting in finger velocities of 50–3000 $\mathrm{\mu m\,s^{-1}}$ in the main branch. The choice of fluids was guided by the requirements that the two fluids be incompressible and immiscible, and that they wet the PDMS and the glass surfaces. The surface tension between the two fluids is approximately $\sigma = 50\,\mathrm{mN\,m^{-1}}$.

Image sequences of the advancing fingers were taken through a stereo-microscope at $\times 7.11$ magnification, using a digital camera at 2000×2000 pixel resolution. A typical image is shown in figure 2. We tracked the position of the advancing fingers in the two daughter tubes over a sequence of images to determine the speed of the two finger tips.

3. Experimental results

Figure 3 shows the evolution of the finger velocities in the two daughter tubes for fingers that are driven by the injection of fluid at two different flow rates. At low flow rates the fingers propagate at approximately the same speed, resulting in an approximately symmetric branching pattern. Conversely, at higher flow rates, any small initial difference in the finger speeds increases rapidly as the fingers propagate into the daughter tubes, resulting in strongly asymmetric branching. We observe that in both cases the sum of the two finger speeds remains constant within experimental error. Experiments conducted in open-ended channels, i.e. without the elastic membranes, always displayed strongly asymmetric propagation, regardless of the driving flow rate. Finally, we note that the initial filling of the viscous oil into an air-filled channel always occurred in a symmetric manner, both with and without the elastic membranes. This is consistent with the experiments of Cassidy *et al.* (2001) who found that finite-length plugs of oil branched symmetrically when flowing through a symmetric air-filled bifurcation.

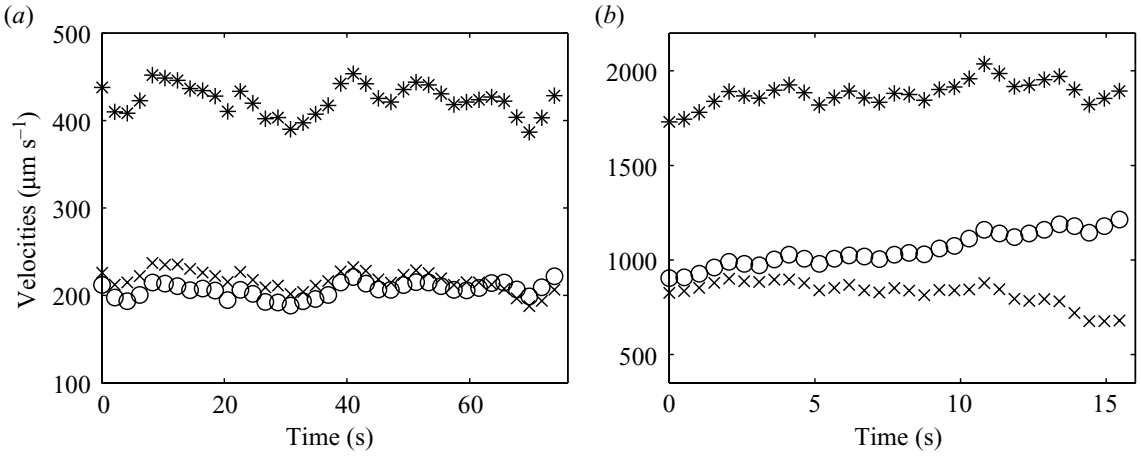

FIGURE 3. Time series of the velocity of the advancing fingers in channels 1 (○) and 2 (×) as a function of time, for two different forcing flow rates. The sum of the two velocities (*) remains approximately constant.

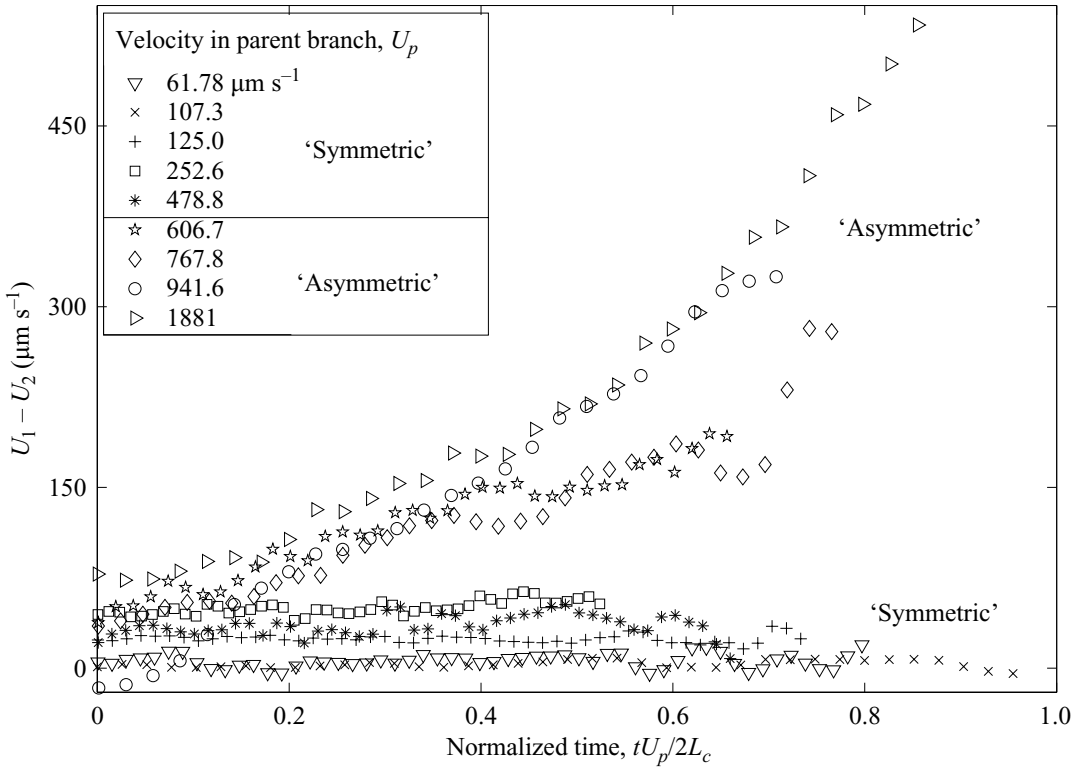

FIGURE 4. Evolution of the velocity difference for the fingers in the two daughter branches. At low flow rates, the velocity differences remain constant. When the velocity in the parent branch exceeds a threshold, the difference in the velocities increases rapidly. We refer to the two regimes as 'symmetric' and 'asymmetric', respectively.

Results for channels with elastic chambers are presented in figure 4 where the symmetry of the branching is characterized by plotting the difference between the finger velocities as a function of the 'normalized distance' $tU_p/2L_c$, where $L_c = 1.7$ cm is the length of the daugther channels. This ordinate facilitates a direct comparison between the different experiments whose duration varies significantly.

At small flow rates, the difference in finger speeds remains approximately constant. When the velocity in the parent channel becomes larger than a threshold, the velocity difference increases rapidly as the fingers propagate along the daughter branches – the

experiment ends when the 'faster' finger reaches the downstream end of its daughter tube. For a given microchannel, the faster finger is always associated with the same branch, suggesting that small imperfections in the fabrication process produce the initial perturbation. These initial perturbations are strongly amplified at high flow rates but remain almost constant if the flow rate is below a threshold. For simplicity, we will refer to the two regimes as 'asymmetric' and 'symmetric', respectively.

The signature of the asymmetric regime is also observed when the low-viscosity finger is not continuous, but made up of discrete drops. These drops may be produced by a splitting of the PFD finger at the entrance of the microchannel, for example if the connecting tube is lined with silicone oil. As the train of drops reaches the bifurcation, each is split into two 'daughter droplets' which travel down the daughter channels. The length ratio of the two daughter drops depends on the relative velocity in the two branches. In the symmetric case, the size ratio remains constant as successive drops arrive at the bifurcation, indicating a constant velocity difference. In the asymmetric case, the velocity difference increases and so does the length ratio of the divided daughter drops. This ratio may eventually diverge as the fast finger approaches the end of the channel and the flow in the other branch slows to a halt.

4. Analysis

We will now develop a simple mathematical model to explain the experimental observations. Since the finger is driven by the injection of fluid at a constant flow rate Q, the pressure, $p_{dr}(t)$, required to drive the finger at this rate varies with time. We denote the lengths of the fluid-filled parts of the daughter tubes ahead of the finger tips by $L_i(t)$ $(i = 1, 2)$ and assume that the daughter tubes have the same cross-sectional area, A.

As the fingers propagate, they displace most of the viscous fluid that initially filled the tube; far behind the finger tips, a thin stationary film of the more viscous fluid is deposited on the tube walls (see Taylor 1961). We denote the flow rate in daughter tube i by $Q_i = U_i\ A_i$, where A_i is the cross-sectional area occupied by the finger which propagates with speed U_i. In the absence of inertial and gravitational effects, a reasonable approximation for microfluidic devices, we have $A_i = A\ \alpha(U_i)$, where the function $\alpha(U_i)$ has been determined for many tube shapes (e.g. Bretherton (1961) and Reinelt & Saffman (1985) for circular tubes; Wong, Radke & Morris (1995) for polygonal tubes; and Hazel & Heil (2002) for tubes of elliptical and rectangular cross-section – we will refer to these references collectively as 'R'). Conservation of mass requires that $Q_1 + Q_2 = Q$.

In each of the daughter tubes, the pressure drop across the occluded section has three components: (i) the Poiseuille pressure drop ahead of the finger tip, $\Delta p_{pois} = \mu \mathscr{R} L_i(t) Q_i(t)$, where the flow resistance $\mathscr{R}$ depends on the tube's cross-section. For instance, for a circular tube of radius a, we have $\mathscr{R} = 8/(\pi a^4)$; values for other cross-sections can be found in the literature (e.g. White 1991); (ii) the pressure drop across the curved tip of the finger, $\Delta p_{tip} = \mathscr{C}(U_i)$, where the function $\mathscr{C}(U_i)$ for many tube shapes is available from the references R (we note that Δp_{tip} includes capillary and viscous contributions); (iii) the pressure p_{elast} in the chambers at the end of the daughter tubes. Provided the membranes that close the (otherwise rigid) chambers are elastic, p_{elast} depends only on the chambers' instantaneous volume and we assume that $p_{elast\,i}(t) = k \int_0^t Q_i(\tau)\,\mathrm{d}\tau + p_{0i}$, where k is a constant and p_{0i} is the pressure in chamber i at time $t = 0$.

Assuming that the viscous pressure drop in the fingers can be neglected, the fingers in both daughter tubes are subject to the same driving pressure $p_{dr}(t)$, and we have

$$p_{dr}(t) = \mathscr{C}(U_i) + \mu\mathscr{R}L_i(t)Q_i(t) + k\int_0^t Q_i(\tau)\,\mathrm{d}\tau + p_{0i} \quad \text{for} \quad i = 1, 2, \tag{4.1}$$

where $Q_i(t) = AU_i(t)\alpha(U_i(t))$. Differentiating the two equations in (4.1) with respect to t yields

$$\frac{\mathrm{d}p_{dr}(t)}{\mathrm{d}t} = \frac{\mathrm{d}U_i(t)}{\mathrm{d}t}\frac{\mathrm{d}\mathscr{C}(U)}{\mathrm{d}U}\bigg|_{U=U_i(t)} + kA\alpha(U_i(t))U_i(t) + \mu A\mathscr{R}\bigg(\frac{\mathrm{d}L_i(t)}{\mathrm{d}t}\alpha(U_i(t))U_i(t) + L_i(t)\frac{\mathrm{d}U_i(t)}{\mathrm{d}t}\frac{\mathrm{d}\alpha(U)}{\mathrm{d}U}\bigg|_{U=U_i(t)} U_i(t) + L_i(t)\,\alpha(U_i(t))\frac{\mathrm{d}U_i(t)}{\mathrm{d}t}\bigg) \quad \text{for} \quad i = 1, 2.$$

Together with the two equations $U_i = -\mathrm{d}L_i/\mathrm{d}t$ (for $i = 1, 2$), this provides a system of four ordinary differential equations, augmented by the algebraic constraint $U_1(t)\alpha(U_1(t)) + U_2(t)\alpha(U_2(t)) = Q/A$. Thus, we have five equations for the five unknowns p_{dr}, U_1, U_2, L_1 and L_2. If $p_{01} = p_{02}$, these equations admit the symmetric solution $L_i(t) = l_0 - \mathscr{U}t$, where the finger velocity $U_i = \mathscr{U}$ in both daughter tubes is given implicitly by

$$\mathscr{U}\alpha(\mathscr{U}) = \frac{1}{2}\frac{Q}{A}. \tag{4.2}$$

We determine the stability of this solution by writing the velocities as $U_i(t) = \mathscr{U} + \epsilon\widehat{U}_i(t)$, where $\epsilon \ll 1$, with similar expansion for all other quantities. A straightforward linear stability analysis then yields the relations $\widehat{L}_1(t) + \widehat{L}_2(t) = 0$ and $\mathrm{d}\widehat{p}_{dr}/\mathrm{d}t = 0$ for the perturbed quantities. The velocity perturbations are governed by

$$\int_{\widehat{U}_i(t=0)}^{\widehat{U}_i(t)} \frac{\mathrm{d}u}{u} = \int_0^t \frac{\mathscr{U}\mathscr{F}(\mathscr{U})}{\mathscr{G}(\mathscr{U}, \tau)}\,\mathrm{d}\tau, \tag{4.3}$$

where

$$\mathscr{G}(\mathscr{U}, t) = (l_0 - \mathscr{U}t)\bigg(\alpha(\mathscr{U}) + \frac{\mathrm{d}\alpha(U)}{\mathrm{d}U}\bigg|_{\mathscr{U}}\mathscr{U}\bigg) + \frac{1}{\mu\mathscr{R}A}\frac{\mathrm{d}\mathscr{C}(U)}{\mathrm{d}U}\bigg|_{\mathscr{U}} \tag{4.4}$$

and

$$\mathscr{F}(\mathscr{U}) = \alpha(\mathscr{U})\bigg(2 - \frac{k}{\mu\mathscr{U}\mathscr{R}}\bigg) + \mathscr{U}\frac{\mathrm{d}\alpha(U)}{\mathrm{d}U}\bigg|_{\mathscr{U}}\bigg(1 - \frac{k}{\mu\mathscr{U}\mathscr{R}}\bigg). \tag{4.5}$$

If the right-hand side of (4.3) is negative, the perturbation velocities $\widehat{U}_i$ decay, indicating that the symmetrically branching solution is stable. To analyse equation (4.3), we first consider the simplifications $\alpha \equiv 1$ (ignoring the presence of the fluid film that the advancing fingers deposit on the channel walls) and $\mathscr{C} \equiv 0$ (ignoring the pressure jump over the air–liquid interface). In this case, (4.3) simplifies to

$$\int_{\widehat{U}_i(t=0)}^{\widehat{U}_i(t)} \frac{\mathrm{d}u}{u} = \int_0^t \frac{2\mathscr{U} - k/(\mu\mathscr{R})}{l_0 - \mathscr{U}\tau}\,\mathrm{d}\tau. \tag{4.6}$$

The denominator of the integrand on the right-hand side represents the instantaneous length of the fluid-filled part of the daughter tubes and is therefore always positive. Perturbations to the symmetrically branching finger will therefore grow if $\mathscr{U}$ exceeds the critical value $U_c = k/(2\mu\mathscr{R})$. Hence at small velocities, when the flow resistance is dominated by the vessel stiffness, the finger will branch symmetrically. Conversely, at

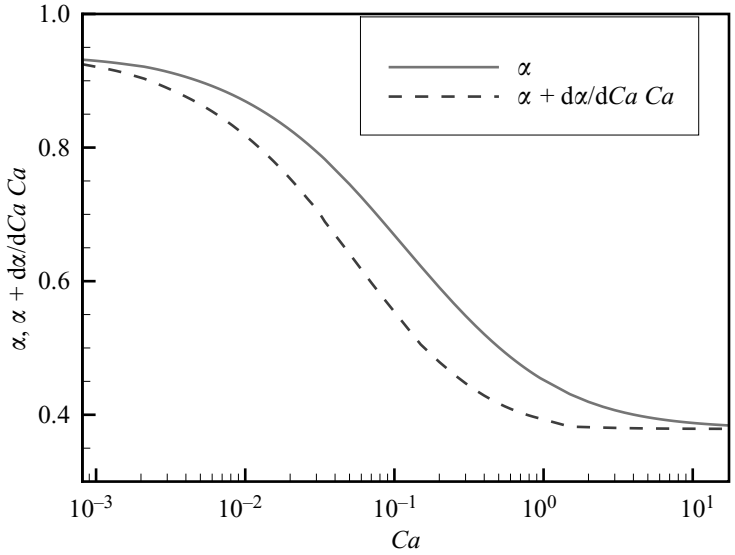

FIGURE 5. The fraction α of the tube's cross-section that is occupied by the propagating finger as a function of the capillary number $Ca = \mu\mathscr{U}/\sigma$ for tubes with square cross-sections. Results for tubes of rectangular, circular and elliptical cross-sections are qualitatively similar.

large finger velocities, the resistance to the flow is dominated by the viscous losses and the propagating finger will tend to open a single path through the branching network.

Without the approximations used in the derivation of (4.6), we must determine the signs of various terms in (4.4) and (4.5). References R show that $\mathrm{d}\mathscr{C}(U)/\mathrm{d}U > 0$ and, using Hazel & Heil's (2002) computational results, we find that $\alpha + \mathscr{U}\,(\mathrm{d}\alpha/\mathrm{d}U)|_{\mathscr{U}} > 0$ (see figure 5 for the case of tubes with square cross-section; the curves for tubes with rectangular, circular and elliptical cross sections are qualitatively similar). Hence $\mathscr{G}(\mathscr{U}, t) > 0$, implying that the growth or decay of the perturbations is determined by the sign of $\mathscr{F}$ which we rewrite in non-dimensional form as

$$\mathscr{F}(Ca) = \alpha(Ca)\left(2 - \frac{\mathscr{K}}{Ca}\right) + Ca\frac{\mathrm{d}\alpha(Ca)}{\mathrm{d}Ca}\left(1 - \frac{\mathscr{K}}{Ca}\right). \tag{4.7}$$

Here, $Ca = \mu\mathscr{U}/\sigma$ is the capillary number based on the propagation speed of the symmetrically propagating fingers and the dimensionless parameter $\mathscr{K} = k/(\mathscr{R}\sigma)$ is a measure of the stiffness of the elastic end chambers.

Figure 6 shows plots of $\mathscr{F}(Ca)$ for square tubes and for a range of values of the parameter $\mathscr{K}$. Also shown (as dashed lines) are the approximations $\mathscr{F}(Ca) \approx 2 - \mathscr{K}/Ca$ which correspond to the simplifications $\alpha \equiv 1$ and $\mathscr{C} \equiv 0$ used in the derivation of (4.6). Figure 6 shows that the critical velocity U_c obtained from the approximate analysis provides an excellent prediction for critical velocity at which the symmetrically branching solution becomes unstable. This is because the capillary pressure jump affects only the magnitude of the growth rate, but not its sign, therefore setting $\mathscr{C} \equiv 0$ does not affect the prediction for U_c. Furthermore, at small capillary number, the thickness of the fluid film that the propagating finger deposits on the channel walls is small, therefore the approximation $\alpha \equiv 1$ becomes more accurate as the capillary number is reduced. This explains why the discrepancy between the exact and the approximate solutions for U_c decreases with Ca. Both analyses show that if $k = 0$, corresponding to the case when the end chambers are open to the atmosphere and

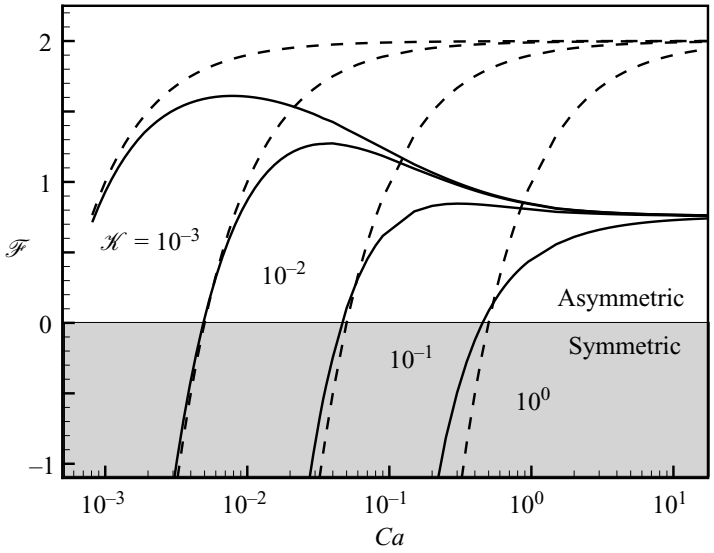

FIGURE 6. The function $\mathscr{F}(Ca)$ for tubes of square cross-section, plotted for various values of the stiffness parameter $\mathscr{K}$. If $\mathscr{F} < 0$ (> 0), the finger branches symmetrically (asymmetrically). The dashed lines represent the approximation $\mathscr{F} = 2 - \mathscr{K}/Ca$ which provides excellent predictions for $\mathscr{F}(Ca) = 0$. Results for tubes of rectangular, circular and elliptical cross-sections are qualitatively similar.

offer no resistance to the flow, we have $\mathscr{F} > 0$, implying that the finger will branch asymmetrically.

5. Comparing theory and experiment

To compare theory and experiment, we must estimate the (volumetric) stiffness k of the end chambers. As discussed in § 2, the end chambers are circular holes of radius $a = 1.6\,\text{mm}$ which are sealed with elastic membranes. Before the start of the experiment, the membranes were pre-stretched by injecting silicone oil until their centres were deflected outwards by approximately $\widehat{w} \approx 400\,\mu\text{m}$. Eschenauer & Schnell's (1986) large-displacement analysis of pressure-loaded circular membranes provides the relation between the chamber pressure and the membrane's maximum deflection, $p_{elast}(\widehat{w})$, and the corresponding chamber volume, $V(\widehat{w})$. Using these results we obtain the volumetric stiffness

$$k = \frac{\mathrm{d}p_{elast}}{\mathrm{d}\widehat{w}}\left(\frac{\mathrm{d}V}{\mathrm{d}\widehat{w}}\right)^{-1} = \frac{6Eh^3}{\pi a^6}\left(\frac{(23-9\nu)}{7(1-\nu)}\left(\frac{\widehat{w}}{h}\right)^2 + \frac{8}{3(1-\nu^2)}\right), \tag{5.1}$$

which has a strong nonlinear dependence on $\widehat{w}$. The volume of PFD injected during the actual experiment is small relative to the total volume of the pressure chambers. Therefore, the injection of the PFD finger causes only small additional deflections and k can be expected to remain approximately constant throughout the experiment. The flow resistance $\mathscr{R}$ of a rectangular channel of width W and aspect ratio 2:1 is given by $\mathscr{R} = 139.93/W^4$ (see White 1991). Using the estimates for the physical parameters given in § 2, we obtain $\mathscr{K} = k/(\mathscr{R}\sigma) \approx 1.0 \times 10^{-3}$, indicating that the transition to non-axisymmetric branching should occur at a capillary number of $Ca \approx \mathscr{K}/2 = 5.0 \times 10^{-4}$. This compares favourably with the experimental data of figure 4 which shows that the transition between symmetric and asymmetric branching occurs for a finger

velocity (in the parent branch) of $U \approx 2\mathscr{U}$ between $478\,\mu\mathrm{m\,s^{-1}}$ and $606\,\mu\mathrm{m\,s^{-1}}$. This corresponds to capillary numbers (based on the velocities in the daughter branches) between $Ca = \mu\mathscr{U}/\sigma = 4.78 \times 10^{-4}$ and 6.06×10^{-4}.

6. Discussion

We have studied the propagation of low-viscosity fingers in a fluid-filled branching network of microchannels and have analysed the behaviour of the finger as it passes a single bifurcation. The behaviour was shown to depend mainly on the relative importance of viscous and elastic forces, characterized by the dimensionless parameter $\lambda = k/(2\mu\mathscr{U}\mathscr{R})$. Viscous effects dominate if the finger velocity and/or the viscous flow resistance are large, so that $\lambda < 1$. In this regime, the finger branches asymmetrically and will tend to open a single path through the network. This is because any perturbation that increases the length of one air finger relative to the length of the other, reduces the viscous flow resistance offered by the column of viscous fluid ahead of the finger tip. This causes the velocity of the longer finger to increase, enhancing the initial difference in finger length even further. We note that the 'inverse' of this mechanism is responsible for the symmetric propagation of the oil fingers that displace the air that initially fills the channel when the experiment is first set up. If a small local imperfection in the channel geometry momentarily allows one of the oil fingers to propagate slightly faster than the other, the resulting increase in the finger length increases the flow resistance and causes the finger to slow down, allowing the other finger to catch up.

Conversely, if the air finger propagates sufficiently slowly and/or if the stiffness of the end chambers is sufficiently large so that $\lambda > 1$, the finger tends to branch symmetrically. This is because the slightly stronger inflation of the elastic end chamber that is connected to the branch conveying the longer finger, creates a strong restoring pressure which reduces the finger velocity until the volumes of both end chambers are approximately equal again.

In the context of the pulmonary airway reopening problem, our results suggest that the reopening of occluded airways should be performed at small speeds to encourage symmetric branching of the air finger as it propagates into the bronchial tree, though it is important to re-iterate that our model provides an extreme simplification of the conditions in the pulmonary airways. For instance, our model is based on a highly idealized geometry; our lumped representation of the wall elasticity ignores the fact that the wall deformation interacts with the fluid flow near the finger tip. Furthermore, while symmetric branching of the propagating air finger is clearly desirable, any attempt to optimize airway reopening procedures will be subject to many additional, and possibly conflicting, constraints. For instance, Bilek, Dee & Gaver (2003) showed that airway reopening at small flow rates may result in cellular damage owing to an increase in the stresses on the airway wall. Finally, we assumed the finger to be driven by an imposed flow rate rather than a controlled driving pressure. In § 4, we showed that $\mathrm{d}\widehat{p}_{dr}/\mathrm{d}t = 0$, implying that there is no difference between the two cases, within the framework of a linear stability analysis. However, nonlinear effects are likely to become important when the deviations in the finger velocities become large. It is therefore conceivable that changes to the driving mechanism could affect the behaviour of the asymmetrically branching solution (see e.g. Halpern *et al.* 2005).

As for microfluidic flows, the results suggest that some limitations exist on the ability to fill a network of channels evenly or to divide drops. For this reason, it will be important to explore ways of stabilizing the symmetric branching in lab-on-a-chip

applications, for example, by introducing an increased resistance to the flow as the finger advances, through the use of elastic forces.

M. H. was supported in part by an EGIDE visiting fellowship at Ecole Polytechnique. S. T. was supported in part by the MIT-France program. The authors acknowledge technical help from José Bico.

REFERENCES

Bilek, A. M, Dee, K. C. & Gaver, D. P. 2003 Mechanisms of surface-tension-induced epithelial cell damage in a model of pulmonary airway reopening. *J. Appl. Physiol.* **94**, 770–783.

Bretherton, F. P. 1961 The motion of long bubbles in tubes. *J. Fluid Mech.* **10**, 166–188.

Calderon, A. J. & Bull J. L. 2004 Homogeneity of bubble transport through a bifurcation for gas embolotherapy. *FASEB J.* **18**, A373.

Cassidy, K. J., Gavriely, N. & Grotberg, J. B. 2001 Liquid plug flow in straight and bifurcating tubes. *J. Biomech. Engng* **123**, 580–589.

Eschenauer, H. & Schnell, W. 1986 *Elastizitätstheorie I*. B. I.-Wissenschaftsverlag, Mannheim.

Gaver, D. P., Samsel, R. W. & Solway, J. 1990 Effects of surface tension and viscosity on airway reopening. *J. Appl. Physiol.* **69**, 74–85.

Halpern, D., Naire, S., Jensen, O. E. & Gaver, D. P. III 2005 Unsteady bubble motion in a flexible-walled channel: predictions of a viscous stick–slip instability. *J. Fluid Mech.* **528**, 53–86.

Hazel, A. L. & Heil, M. 2003 Three-dimensional airway reopening: the steady propagation of a semi-infinite bubble into a buckled elastic tube. *J. Fluid Mech.* **478**, 47–70.

Hazel, A. L. & Heil, M. 2002 The steady propagation of a semi-infinite bubble into a tube of elliptical or rectangular cross-section. *J. Fluid Mech.* **470**, 91–114.

Homsy, G. 1987 Viscous fingering in porous media. *Annu Rev. Fluid Mech.* **19**, 271–311.

Link, D., Anna, S., Weitz, D. & Stone, H. 2004 Geometrically mediated breakup of drops in microfluidic devices. *Phys. Rev. Lett.* **92**, 054503.

Quake, S. R. & Scherer, A. 2000 From micro- to nano-fabrication with soft materials. *Science* **290**, 1536–1540.

Reinelt, D. & Saffman, P. 1985 The penetration of a finger into a viscous fluid in a channel and tube. *SIAM J. Sci. Stat. Comput.* **6**, 542–561.

Song, H., Tice, J. & Ismagilov, R. 2003 A microfluidic system for controlling reaction networks in time. *Angew. Chem., Intl Edn* **42**.

Taylor, G. I. 1961 Deposition of a viscous fluid on the wall of a tube. *J. Fluid Mech.* **10**, 161–165.

White, F. 1991 *Viscous Fluid Flow*. McGraw-Hill.

Wong, H., Radke, C. J. & Morris, S. 1995 The motion of long bubbles in polygonal capillaries. Part 1. Thin films. *J. Fluid Mech.* **292**, 71–94.

Available online at www.sciencedirect.com
ScienceDirect
Journal of Colloid and Interface Science 308 (2007) 231–238
JOURNAL OF Colloid and Interface Science
www.elsevier.com/locate/jcis

Transport of wetting liquid plugs in bifurcating microfluidic channels

Cédric P. Ody, Charles N. Baroud *, Emmanuel de Langre

Laboratoire d'Hydrodynamique (LadHyX), Ecole Polytechnique-CNRS, 91128 Palaiseau Cedex, France

Received 16 August 2006; accepted 5 December 2006

Available online 12 December 2006

Abstract

A plug of wetting liquid is driven at constant pressure through a bifurcation in a microchannel. For a plug advancing in a straight channel, we find that the viscous dissipation in the bulk may be estimated using Poiseuille's law while Bretherton and Tanner's laws model the additional dissipation occurring at the rear and front interfaces. At a second stage, we focus on the behavior of the plug flowing through a T-junction. Experiments show the existence of a threshold pressure, below which the plug remains blocked at the entrance of the junction. Above this required pressure, the plug enters the bifurcation and either ruptures or splits into two daughter plugs, depending on the applied pressure and on the initial length of the plug. By means of geometrical arguments and the previously cited laws, we propose a global model to predict the transitions between the three observed behaviors.

Keywords: Microfluidic bifurcation; Plug rupture; Threshold pressure; Splitting

1. Introduction

Microfluidic fabrication techniques provide new ways to handle fluids in complex geometries at sub-millimeter scale. While the transport of a single fluid is well understood in the laminar "Stokes" regime, two-phase flows present important challenges due to the nonlinear effects at the moving interfaces. Indeed, even the transport of liquid plugs in a straight channel involves a nonlinear pressure–velocity relationship that results from the balance between viscous and capillary effects [1]. This balance operates near the triple lines at which the liquid and gas phases meet the solid substrate; the details of this balance depend strongly on the wetting properties of the solid and the liquid [2].

The transport of plugs in a complex geometry, such as a network of channels, is of interest for microfluidics but also in geological and biological situations. For instance, an understanding of the transport of plugs through bifurcations is necessary for applications in drug delivery in the pulmonary airway tree [3], or in the extraction of oil from porous rocks [4], where one is interested in the transport of a volume of a liquid (mucus or petroleum) bounded by two liquid–gas interfaces. Since the liquid usually wets the solid in these situations, this will be represented at rest by a zero contact angle between the two phases.

The aim of the present work is to study the transport of such plugs in rectangular microchannels, when both inertia and gravity are negligible. This is done by driving plugs at constant pressure through straight and bifurcating microchannels and by developing corresponding theoretical models. A combined theoretical and experimental study of the straight and bifurcating cases will therefore provide the essential building block for understanding the dynamics of a two-phase flow in a channel network, which in turn will allow the modeling of concrete situations.

The paper is structured as follows: Section 2 presents the experimental setup and protocol. It is followed in Section 3 by the development of a theoretical model for a plug in a straight channel which is validated experimentally. Finally, Sections 4 and 5 provide the experimental and theoretical study of the flow of a plug through a T-junction, respectively.

* Corresponding author.
E-mail address: baroud@ladhyx.polytechnique.fr (C.N. Baroud).

0021-9797/$ – see front matter
doi:10.1016/j.jcis.2006.12.018

2. Experimental setup

A schematic of the experimental setup used in our study is shown in Fig. 1. The experiments were conducted in rectangular cross section microfluidic channels made of polydimethylsiloxane (PDMS) by using soft lithography techniques [5]. These channels are integrated in a microfluidic chip, composed of two parts. To obtain the upper part in which the channel is etched, a thin layer of photosensitive resin (Microchem, SU8-2035) is first spin-coated on a silicon wafer and patterned by standard photolithography. The speed of spin-coating sets the thickness b of the future channels, while the widths and the shapes are controlled by the design of the patterned masks which are used during the UV exposure. The photoresist is then developed yielding the mold on which a thick layer of PDMS (Dow Corming, Sylgard 184) is poured and allowed to partially cure. The resulting cast is finally removed from the mold and inlet/outlet holes are punched for later connections. In parallel, the lower part of the microchannel is obtained by spin-coating and partially curing a flat layer of PDMS on a glass microscope slide. At a final stage, the two PDMS parts are brought into contact and the whole is cured completely, thus forming a microfluidic chip. As seen in Fig. 1, the microchannel consists of an entrance region (Y-junction) used to form the liquid plugs, an initial straight channel and a final T-junction. We note that w_i and w_o are the widths of the inlet and outlet branches of the T-junction. Typical values for the thickness and the width of the straight channel were $b \simeq 25$–50 μm and $w_\mathrm{i} \simeq 200$–300 μm. The different dimensions were measured on the resin mold with a profilometer (Dektak).

A constant driving pressure P_dr was applied using a water column connected to a sealed air bottle as shown in Fig. 1; the air flowing out of the bottle was then driven to one inlet of the Y-junction while the other inlet was used for liquid introduction. Outlets of the T-junction were at atmospheric pressure P_0. Different values of the driving pressure P_dr were obtained by varying the height of water in the column and calculating the corresponding hydrostatic pressure, ranging from 100 Pa (≃1 cm of water) up to 600 Pa (≃60 cm of water). The precision on the water height pressure was 2 mm, giving a maximum error of 20% for the lowest pressure value. All pressure losses in the external tubing were neglected.

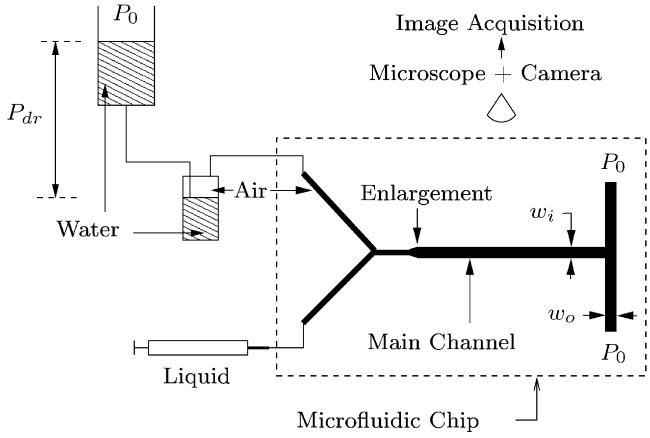

Fig. 1. Experimental setup. A constant pressure P_dr is applied at the upper left inlet branch of the Y-junction. The lower left branch is used to introduce the wetting liquid from a syringe pump. The motion of the plug is recorded with a camera through a microscope. Note the enlargement of the inlet channel downstream of the Y-junction.

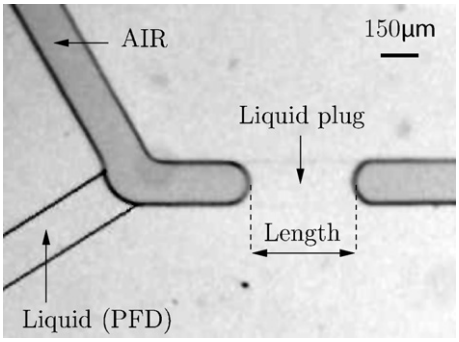

Fig. 2. A liquid plug after its formation within the Y-junction. The plug moves from left to right. The upper branch is connected to the constant pressure source (air) and the lower branch contains the wetting liquid which is injected using a syringe pump. Length and speed are calculated from the measured positions of the menisci at the advancing (front) and receding (rear) interfaces, detected along the centerline of the channel.

The plugs were formed with perfluorodecalin (PFD), a fluorinated liquid with dynamic viscosity $\eta = 5$ cP and surface tension $\gamma = 15$ mN/m [6]. In addition to wetting the solid substrate, the PFD also has the advantage of not swelling the PDMS [7]. To obtain the typical plug shown in Fig. 2, the liquid was forced into one inlet of the Y-junction by actuating a syringe pump for a given interval of time while a manual valve cut off the air entrance from the pressure source. Once the plug was formed, the syringe pump was switched off, and the pressure was applied. By controlling the duration of the syringe pump actuation, plugs of different lengths were obtained. However, since the minimal length of the plugs was fixed by the characteristic size of the Y-junction, the channel was enlarged downstream of the Y-junction to allow the study of shorter plugs, resulting in lengths as small as the width w_i of the inlet channel. There was no upper limit for the size of the plugs.

Experiments were recorded with a high speed camera (resolution 1024×256 pixels, 1 pixel for 10 μm, sampled at 10–100 fps) through a microscope (Leica, MZ 16). For each image of the sequences thus obtained, the positions (x_f and x_r) of the menisci at the advancing (front) and receding (rear) interfaces of the traveling plug were manually located along the centerline of the channel. These measurements yielded the length and the speed of the plug during its transport as, respectively, $L_\mathrm{plug} = x_\mathrm{f} - x_\mathrm{r}$ and $U_\mathrm{plug} = \mathrm{d}x_\mathrm{c}/\mathrm{d}t$ with $x_\mathrm{c} = (x_\mathrm{f} + x_\mathrm{r})/2$. Note that before starting data acquisition, several plugs of PFD were introduced in order to prewet the channel walls.

A sketch of a plug moving in a rectangular microchannel is shown in Fig. 3. In this schematic, plane A ("in-plane" section) represents the projected view as seen through the microscope, e.g., Fig. 2. We will also refer later to plane B as the "in-thickness" section.

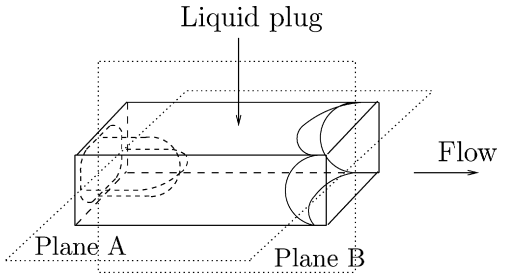

Fig. 3. Schematic of a plug in a rectangular channel. Planes A and B correspond respectively to "in-plane" and "in-thickness" sections.

3. Visco-capillary regime in straight channels

We first consider the transport of a liquid plug of length L_0 moving with a steady velocity U_0 in the straight microchannel upstream of the T-junction. By taking a characteristic length scale $D \sim 50$ μm and typical velocities $U_0 \sim 5$ mm/s, one obtains a Bond number $\mathrm{Bo} = \rho g D^2/\gamma \sim 5 \times 10^{-3}$ and a Reynolds number $\mathrm{Re} = \rho U_0 D/\eta \sim 2 \times 10^{-2}$, where $\rho \sim 1000$ kg/m^3 and $g = 9.81$ m/s^2 are, respectively, the density of the liquid and the acceleration of gravity. Therefore, one may neglect gravity and inertial effects, expecting the plug dynamics to be governed by a visco-capillary regime as mentioned in [8]. Here, we use an approach similar to the one developed by Bico and Quéré [1]. Given a constant driving pressure P_{dr}, the steady-state pressure balance across the plug is

$$P_{\mathrm{dr}} = \Delta P^{\mathrm{r}}_{\mathrm{cap}} + P_{\mathrm{visc}} + \Delta P^{\mathrm{a}}_{\mathrm{cap}}, \tag{1}$$

where $\Delta P^{\mathrm{r}}_{\mathrm{cap}}$ and $\Delta P^{\mathrm{a}}_{\mathrm{cap}}$ express the capillary pressure drops at the receding and advancing interfaces of the plug, respectively, while P_{visc} represents the viscous dissipation occurring in the bulk. Using Poiseuille's law, the latter is expressed as

$$P_{\mathrm{visc}} = \alpha \eta L_0 U_0, \tag{2}$$

with α, a dimensional coefficient, corresponding to the geometry of the channel. For a rectangular geometry [9], α may be approximated as

$$\alpha \simeq \frac{12}{b^2}\left[1 - 6\frac{2^5 b}{\pi^5 w_{\mathrm{i}}}\right]^{-1}. \tag{3}$$

When the plug is at rest, static values of $\Delta P^{\mathrm{r}}_{\mathrm{cap}}$ and $\Delta P^{\mathrm{a}}_{\mathrm{cap}}$ are given by Laplace's law as $\Delta P^{\mathrm{r}}_{\mathrm{cap}} = -\Delta P^{\mathrm{a}}_{\mathrm{cap}} = \gamma\kappa$, where $\kappa \simeq 2(b^{-1} + w_{\mathrm{i}}^{-1})$ is the mean curvature of each interface at rest. Here, we neglect the flow of liquid along the corners of the channel that slightly deforms the shape of the interfaces [10]. When the plug is moving, the front and rear curvatures are modified as shown in Fig. 4. At the front interface, the balance between friction and wetting forces at the vicinity of the contact line leads to the existence of a non-zero dynamic contact angle and this flattening of the advancing interface increases the resistance to the motion. By assuming that θ^{a} has the same value in the two sections, the dynamic capillary pressure drop for the front interface becomes

$$\Delta P^{\mathrm{a}}_{\mathrm{cap}} = -\gamma\kappa\cos\theta^{\mathrm{a}}. \tag{4}$$

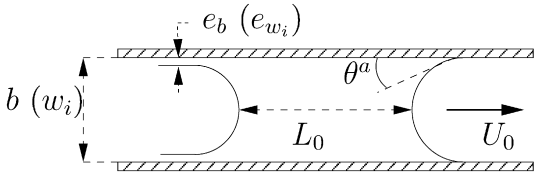

Fig. 4. Sketch of the plug (sections A and B). Here, θ^{a} is the dynamic contact angle at the front interface and e_{b} ($e_{w_{\mathrm{i}}}$) is the thickness of the deposited film at the rear of the plug in the thickness (width).

The relation between the contact angle and the velocity of the contact line is known through Tanner's law [1,11] which states that

$$\theta^{\mathrm{a}} = (6\Gamma\mathrm{Ca})^{1/3}, \tag{5}$$

where $\mathrm{Ca} = \eta U_0/\gamma$ is the capillary number and Γ is a logarithmic prefactor that accounts for the singularity occurring at the contact line, where the usual no-slip boundary condition at the solid surface leads to a logarithmic divergence in the shear stress [12].

Using Eq. (5) and taking the first-order term in the Taylor expansion of $\cos\theta^{\mathrm{a}}$ in Eq. (4), the front pressure drop becomes

$$\Delta P^{\mathrm{a}}_{\mathrm{cap}} \simeq \gamma\kappa\left(-1 + \frac{(6\Gamma\mathrm{Ca})^{2/3}}{2}\right). \tag{6}$$

At the rear interface, a thin film is deposited at the channel walls [13], which reduces the rear meniscus radius and thus, also increases the resistance to the motion. We note that e_{b} and $e_{w_{\mathrm{i}}}$ are the thicknesses of the deposited film at the rear of the plug in the in-thickness and in-plane sections, respectively. The dynamic capillary pressure drop at the rear interface may then be written as

$$\Delta P^{\mathrm{r}}_{\mathrm{cap}} = \gamma\left(\frac{1}{b/2 - e_{\mathrm{b}}} + \frac{1}{w_{\mathrm{i}}/2 - e_{w_{\mathrm{i}}}}\right). \tag{7}$$

Bretherton's law expresses the thickness e of the deposited film at the rear of a plug as a function of the capillary number Ca and the radius R of a circular capillary tube [1]:

$$e/R = 3.88\mathrm{Ca}^{2/3}. \tag{8}$$

Assuming Bretherton's law to be valid in both directions of the rectangular cross section, i.e., $2e_{\mathrm{b}}/b = 2e_{w_{\mathrm{i}}}/w_{\mathrm{i}} = 3.88\mathrm{Ca}^{2/3}$, the rear capillary jump is obtained from Eq. (7) as

$$\Delta P^{\mathrm{r}}_{\mathrm{cap}} = \gamma\kappa\left(1 + 3.88\mathrm{Ca}^{2/3}\right). \tag{9}$$

Finally, by using Eqs. (2), (6) and (9), one derives

$$P_{\mathrm{dr}} \simeq \alpha\eta L_0 U_0 + \gamma\kappa\beta\mathrm{Ca}^{2/3}, \tag{10}$$

where $\beta = 3.88 + (6\Gamma)^{2/3}/2$ is a nondimensional coefficient obtained from Bretherton's and Tanner's laws.

Equation (10) governs the dynamics of a plug of length L_0 moving steadily at speed U_0 in a straight rectangular channel for a constant driving pressure. Equation (10) can be nondimensionalized by comparing it with the capillary pressure jump $\gamma\kappa$, and we obtain

$$\overline{P_{\mathrm{dr}}} \simeq \bar{\alpha}\mathrm{Ca} + \beta\mathrm{Ca}^{2/3}, \tag{11}$$

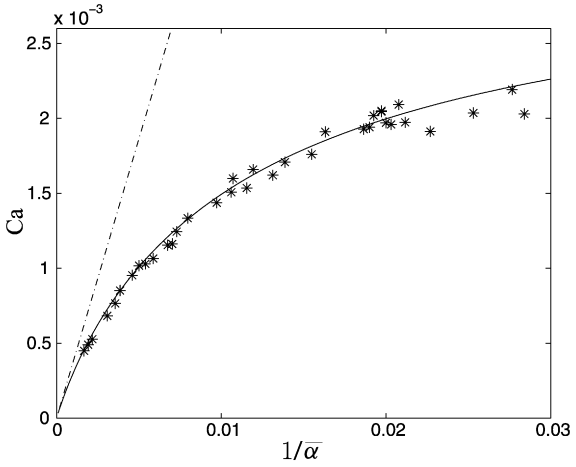

Fig. 5. Capillary number of a liquid plug as a function of its inverse nondimensional length $1/\bar{\alpha}$ for a pressure $P_{\mathrm{dr}} = 250$ Pa ($\overline{P_{\mathrm{dr}}} = 0.2$). The dashed line corresponds to Poiseuille's law, $\mathrm{Ca} \propto 1/\bar{\alpha}$. The full line corresponds to Eq. (11) with $\beta = 16$.

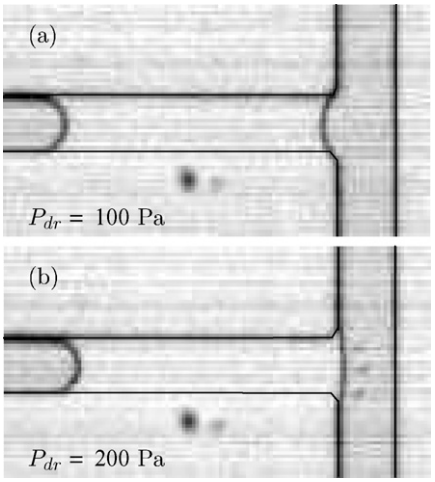

Fig. 6. Blocking of the plug at the entrance of the T-junction for two distinct pressures with $P_{\mathrm{dr}} < P_{\mathrm{thresh}}$. The front interface is pinned at the corners of the bifurcation and adapts its curvature to the applied pressure. The shape of the rear interface is independent of P_{dr}.

with $\overline{P_{\mathrm{dr}}} = P_{\mathrm{dr}}/(\gamma\kappa)$ is the nondimensional driving pressure and $\bar{\alpha} = \alpha L_0/\kappa$ is the nondimensional length.

Experiments were conducted in a microchannel to verify the applicability of Eq. (11) to our rectangular geometry. The cross section of the microchannels used here was $w_{\mathrm{i}} \times b = 210 \times 25$ μm. Single plugs of various lengths were introduced and forced at constant pressure following the protocol of Section 2. For all driving pressures, we observed that the measured lengths and speeds of the plugs remained constant within 5% throughout the channel and average length L_0 and speed U_0 were determined.

A sample of experimental results is plotted in Fig. 5. Data corresponding to long plugs asymptote to Poiseuille's law (dashed line, $\overline{P_{\mathrm{dr}}} = \bar{\alpha}\mathrm{Ca}$ from Eq. (2)). For shorter plugs, the data exhibit a nonlinear Ca vs $(\bar{\alpha})^{-1}$ relationship due to an additional dissipation occurring at the interfaces. The theoretical curve (full line) obtained from Eq. (11) is plotted with $\beta = 16$ and is in good agreement with the experimental data. The corresponding value of $\Gamma = 20$ is higher than experimental values reported in millimetric circular tubes [1]. However, the coefficient $(6\Gamma)^{1/3} = 4.9$ appearing in Tanner's law (Eq. (5)) is in close agreement with Hoffman's data [11] for which the previous coefficient is of order 4–5 for a dry tube. A more precise estimate of the Tanner's constant would require a specific study by keeping track of both the microscopic and macroscopic physics involved in our configuration, as described in [12].

Thus, although Bretherton's and Tanner's laws are not strictly applicable to the rectangular geometry, our results show the possibility of using the previous laws to model the dynamics of plugs in our channels.

4. Blocking, rupture or splitting at the T-junction

We now consider a plug flowing through the T-junction for different driving pressures and initial plug lengths, L_0, measured in the straight channel upstream of the bifurcation. Experiments were conducted with channel dimensions $w_{\mathrm{i}} \times w_{\mathrm{o}} \times b = 260 \times 260 \times 46$ μm. Three different behaviors were observed depending on the driving pressure and on the initial length of the plug as described below.

4.1. Blocking

The first feature extracted from the observations of a plug getting to the T-junction is the existence of a threshold pressure P_{thresh} (between 200 and 300 Pa for our experiments) which does not depend on the initial length of the plug. For $P_{\mathrm{dr}} < P_{\mathrm{thresh}}$, the plug remains blocked at the entrance of the bifurcation as presented in Fig. 6, which shows the equilibrium positions of plugs for two distinct pressures ($P_{\mathrm{dr}} = 100$, 200 Pa). While the rear interface has the same shape in both cases, the front interface adapts its curvature to balance the applied pressure keeping its extremities pinned at the corners of the bifurcation.

4.2. Rupture

When the pressure exceeds the threshold pressure P_{thresh}, the plug continues its propagation through the bifurcation. If the plug is short, its rear interface catches up with its front interface before the latter reaches the wall opposite to the entrance channel. The plug then ruptures, opening the outlet branches of the T-junction to air. A typical sequence of plug rupture is shown in Fig. 7. Eventually, the liquid that remains on the channel walls drains slowly through the action of capillary forces and air drag.

4.3. Splitting into two daughter plugs

When the plugs are sufficiently long that the front interface reaches the opposite wall, two daughter plugs of equal length are formed through a splitting of the initial one, as shown in Fig. 8. As soon as the liquid reaches the wall, the transport

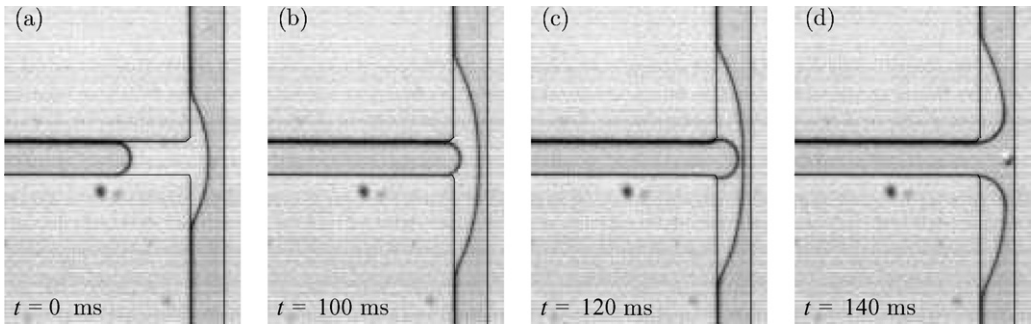

Fig. 7. Sequence of plug rupture. The plug ruptures in the T-junction, leaving liquid on one side of the outlet channel, where air can flow freely from the pressure source.

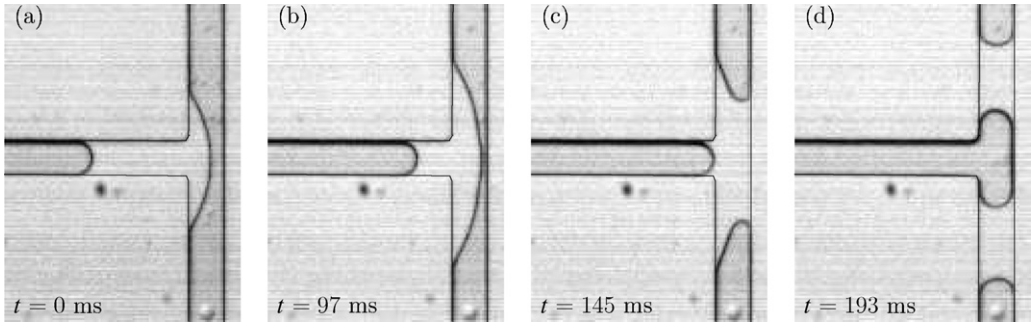

Fig. 8. Sequence of plug splitting at the T-junction. Splitting leads to symmetric formation of two daughter plugs in the outlet branches of the T-junction.

dynamics becomes dominated by the wetting forces acting between the two phases. These forces act to draw the liquid very rapidly into contact with the wall, as observed between the images (b) and (c) of Fig. 8. In part (c), we see that the curvature is not constant along the liquid surface, implying local pressure gradients in the fluid which pull it into the daughter branches. These wetting forces are dominant compared to the driving pressure, as seen by the rapidity of the advance once the plug has touched the wall.

Note that before rupture or splitting, the evolution of the plug in the bifurcation is similar in both cases: the front interface advances without constraints while the extremities of the rear interface remain pinned by the corners of the bifurcation until process of rupture or splitting is achieved (Fig. 7c).

4.4. Phase diagram

We summarize the three cases discussed above (blocking, rupture and splitting) in the experimental phase diagram shown in Fig. 9. As stated above, we observed the blocking (△) of the plug below a threshold pressure, P_{thresh}, whose value is seen to be independent on the length of the plug. Above P_{thresh}, experimental data show that the transition between rupture (■) and splitting (○) depends on the applied pressure and on the length of the plug: as the pressure increases, the length of liquid required to create two daughter plugs becomes smaller.

5. Theoretical model

In this section, the two transitions appearing in the phase diagram of Fig. 9 are explained theoretically. We first establish a

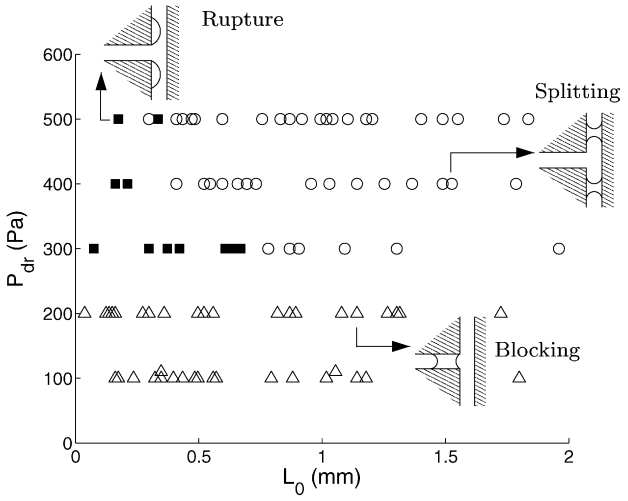

Fig. 9. Phase diagram for plug behavior at the T-junction.

2D pressure balance to derive the value of the blocking pressure after which we develop a model to predict the transition between rupture and splitting.

5.1. Threshold pressure

Since the plug is at rest in the blocking case, the viscous term in Eq. (1) is zero and the new pressure balance may be written as

$$P_{\text{dr}} = \Delta P^{\text{r}}_{\text{cap}} + \Delta P^{\text{a}}_{\text{cap}}. \tag{12}$$

Here, the terms $\Delta P^{\text{r}}_{\text{cap}}$ and $\Delta P^{\text{a}}_{\text{cap}}$ express static pressure drops and Eq. (12) may be simplified by distinguishing in-plane and

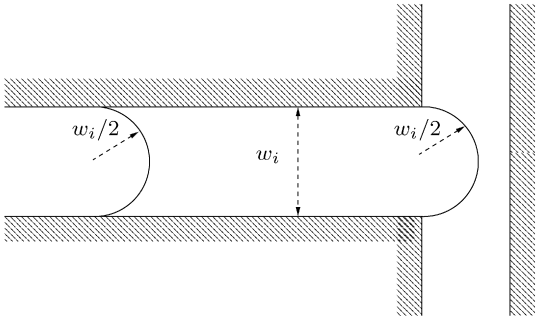

Fig. 10. The shapes of the rear and front interfaces at the threshold pressure (in-plane section).

in-thickness contributions of the capillary pressure jumps which are related via Laplace's law to the corresponding principal curvatures of the interfaces. Since the channel thickness does not vary at the bifurcation, we assume that the in-thickness components of the pressure drops at the rear and front interfaces cancel each other, the radii of curvature in the thickness being $b/2$ in absolute value. Therefore, the problem is reduced to a 2D pressure balance of in-plane components of pressure drops, leading to

$$P_{\mathrm{dr}} = \gamma\left(\frac{1}{R^{\mathrm{r}}} + \frac{1}{R^{\mathrm{a}}}\right), \tag{13}$$

where R^{r} and R^{a} are the radii of curvature of the rear and front interfaces in plane A, respectively.

The experimental observations shown in Fig. 6 provide the information to derive the value of the threshold pressure. For $P_{\mathrm{dr}} < P_{\mathrm{thresh}}$, the receding interface is seen to keep a constant in-plane radius of curvature $R^{\mathrm{r}} = w_{\mathrm{i}}/2$ while the advancing interface adapts its in-plane curvature to the applied pressure and its radius R^{a} varies such that $|R^{\mathrm{a}}| \geqslant w_{\mathrm{i}}/2$. The situation in which $R^{\mathrm{a}} = +w_{\mathrm{i}}/2$ is illustrated in Fig. 10 and leads to the threshold pressure, which is the highest pressure that can be sustained across the plug, reading finally

$$P_{\mathrm{thresh}} = \frac{4\gamma}{w_{\mathrm{i}}}. \tag{14}$$

For our experimental conditions ($w_{\mathrm{i}} = 260\,\mu\mathrm{m}$ and $\gamma = 15\,\mathrm{mN/m}$), we obtain $P_{\mathrm{thresh}} \simeq 230\,\mathrm{Pa}$, in agreement with the measured value ($200\,\mathrm{Pa} < P_{\mathrm{thresh}} < 300\,\mathrm{Pa}$).

5.2. Rupture or splitting

We now propose to explain the critical plug length, L_{crit}, for getting rupture or splitting when the pressure exceeds the threshold pressure. Our aim here is not to model the complete dynamics of the plug but to derive a global model which clarifies the dependence of L_{crit} on the driving pressure P_{dr} by taking into account the fundamental mechanisms involved in the plug evolution. We first consider a plug of length L_{crit} theoretically situated on the transition curve. A geometric condition is then obtained from the shape of such a plug in the T-junction. Finally, a dynamic argument is used to map this geometric condition onto the experimental L_0–P_{dr} diagram.

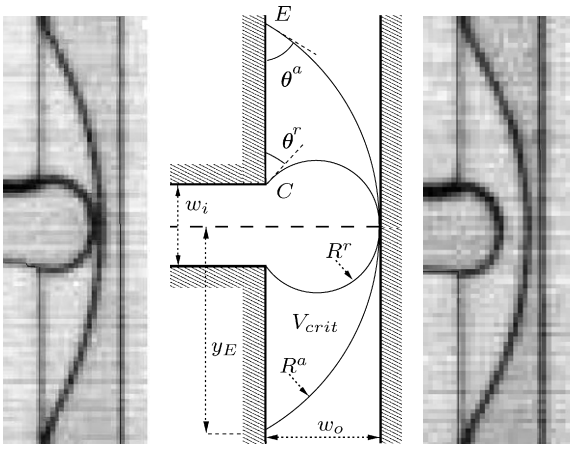

Fig. 11. Shape of the plugs before (a) rupture and (c) splitting. (b) Schematic of a plug of volume V_{crit} situated on the theoretical boundary between rupture and splitting where front and rear interfaces of a plug meet at the wall.

5.2.1. Geometric condition

The diagram of Fig. 9 exhibits a L_0–P_{dr} dependent boundary between the rupture or splitting cases. We consider the shape of the plugs just before rupture or splitting, as shown in Figs. 11a and 11c. In Fig. 11a, the rear interface catches up with the front interface before the latter reaches the wall, leading to rupture of the plug. Conversely, in Fig. 11c, the front interface is about to touch the wall before the rear interface catches up with it, resulting in the splitting of the plug and the formation of two daughter plugs. In the limiting case, a plug of length L_{crit} sees its front and rear interfaces meeting at the wall. Approximating the shape of both interfaces with circular sections leads to the sketch of Fig. 11b. Here, the critical volume of the plug is noted V_{crit} and is completely defined by θ^{a}, θ^{r}, w_{o} and the thickness b of the microchannel. At point C, the rear contact angle θ^{r} is defined geometrically as $\theta^{\mathrm{r}} = 2\arctan(w_{\mathrm{i}}/2w_{\mathrm{o}})$. In contrast, the contact angle θ^{a} at point E may take different values depending on the velocity of the advancing interface. As a result, the critical volume decreases as θ^{a} increases for a given T-junction, down to a zero volume when $\theta^{\mathrm{a}} = \pi - \theta^{\mathrm{r}}$.

The volume of liquid contained between the two interfaces in the critical configuration corresponding to Fig. 11b is obtained as

$$V_{\mathrm{crit}} = bw_{\mathrm{o}}^2\big[f\big(\theta^{\mathrm{a}}\big) - g\big(\theta^{\mathrm{r}}\big)\big], \tag{15}$$

where

$$f\big(\theta^{\mathrm{a}}\big) = \big(\theta^{\mathrm{a}} - \cos\theta^{\mathrm{a}}\sin\theta^{\mathrm{a}}\big)\big(1 - \cos\theta^{\mathrm{a}}\big)^{-2} \tag{16}$$

and

$$g\big(\theta^{\mathrm{r}}\big) = \big(\pi - \theta^{\mathrm{r}} + \cos\theta^{\mathrm{r}}\sin\theta^{\mathrm{r}}\big)\big(1 + \cos\theta^{\mathrm{r}}\big)^{-2}. \tag{17}$$

This volume corresponds to a plug of length L_{crit} in the entrance channel such that

$$V_{\mathrm{crit}} = b\big[L_{\mathrm{crit}}w_{\mathrm{i}} + (1 - \pi/4)w_{\mathrm{i}}^2\big], \tag{18}$$

with the correction term $b(1 - \pi/4)w_{\mathrm{i}}^2$ taking into account the volume contained in the circular menisci. Therefore, the critical

length is such that

$$\frac{L_{\text{crit}}}{w_{\text{i}}} = \left(\frac{w_{\text{o}}}{w_{\text{i}}}\right)^2 \left[f\left(\theta^{\text{a}}\right) - g\left(\theta^{\text{r}}\right)\right] - \left(1 - \frac{\pi}{4}\right). \tag{19}$$

For a given contact angle θ^{a}, a plug of initial length $L_0 < L_{\text{crit}}$ will rupture in the bifurcation while a plug such that $L_0 > L_{\text{crit}}$ will produce two daughter plugs.

Since θ^{r} is a function of the ratio $w_{\text{o}}/w_{\text{i}}$, the value of L_{crit} depends on θ^{a} and $w_{\text{o}}/w_{\text{i}}$. Therefore, Eq. (19) will provide different values of L_{crit} as θ^{a} varies, the other quantities being constant for a given geometry. The problem is now to understand the mechanisms involved in the determination of θ^{a}.

5.2.2. Dynamic condition

Although the propagation in the bifurcation is unsteady, the dynamics is still governed by a visco-capillary regime. Therefore, at a given time, we may use Eq. (1) on a specific fluid streamline. For simplicity, we choose the streamline linking points C and E.

Close to point C, the speed of the rear interface is nil since it is pinned at the corners of the junction. Thus, the capillary drop at the receding interface is approximated as

$$\Delta P^{\text{r}}_{\text{cap}} = \gamma\left(\frac{1}{R^{\text{r}}} + \frac{2}{b}\right), \tag{20}$$

where R^{r} is the in-plane radius of the receding interface (see Fig. 11b) and is expressed as

$$R^{\text{r}} = \frac{w_{\text{o}}}{1 + \cos\theta^{\text{r}}}. \tag{21}$$

For the front interface, we assume that the speed of the contact line at point E establishes the contact angle θ^{a} and that θ^{a} is the same in the thickness and in the plane. Therefore, the capillary drop at the advancing interface reads

$$\Delta P^{\text{a}}_{\text{cap}} = \gamma\left(\frac{1}{R^{\text{a}}} - \frac{2\cos\theta^{\text{a}}}{b}\right), \tag{22}$$

where R^{a} is the in-plane radius of the advancing interface, calculated from geometry as

$$R^{\text{a}} = \frac{w_{\text{o}}}{1 - \cos\theta^{\text{a}}}. \tag{23}$$

The viscous term in Eq. (1) is approximated as a dissipation term in a Hele–Shaw geometry (since $b/w_{\text{o}} \simeq 0.18$), leading to

$$P_{\text{visc}} = \frac{12\eta}{b^2} L_{\text{m}} V_{\text{m}}, \tag{24}$$

where L_{m} is the length of the streamline C–E and V_{m} the mean speed of the fluid particles between points C and E. As stated above, the speed at point C is nil and the speed at point E is related to the contact angle by Tanner's law (Eq. (5)) as

$$V_{\text{E}} = \frac{\gamma}{\eta}\text{Ca}_{\text{E}} = \frac{\gamma(\theta^{\text{a}})^3}{6\eta\Gamma}. \tag{25}$$

We estimate the quantities V_{m} and L_{m} to first order as $V_{\text{m}} = (V_{\text{E}} + V_{\text{C}})/2$ and $L_{\text{m}} = y_{\text{E}} - w_{\text{i}}/2$, where $y_{\text{E}} = w_{\text{o}}/\tan(\theta^{\text{a}}/2)$ is the distance from point E to the centerline of the inlet channel (see Fig. 11b).

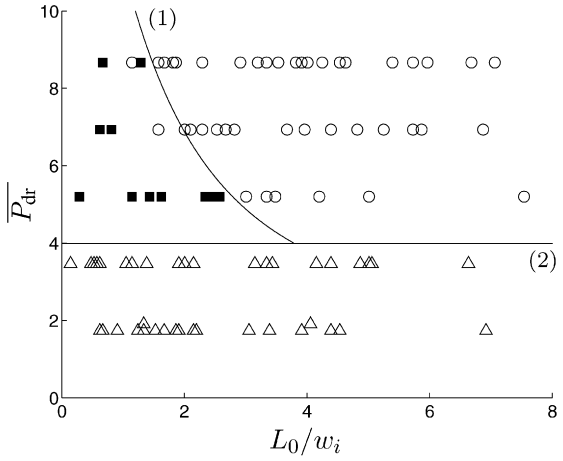

Fig. 12. Experimental $\overline{P_{\text{dr}}}$–L_0/w_{i} diagram and theoretical transitions. (1) Rupture-splitting transition corresponding to Eq. (27) with θ^{a} varying from $\pi/6$ to $\pi/3$ and $(6\Gamma)^{1/3} = 4.9$. (2) Threshold pressure (Eq. (14)).

Finally, combining the terms above leads to the pressure balance across the plug

$$P_{\text{dr}} \simeq \gamma\left[2\frac{y_{\text{E}} - w_{\text{i}}/2}{\Gamma b^2}\left(\theta^{\text{a}}\right)^3 + \frac{1}{R^{\text{a}}} + \frac{1}{R^{\text{r}}} + \frac{2}{b}\left(1 - \cos\theta^{\text{a}}\right)\right], \tag{26}$$

which accounts for the dynamic relation between θ^{a} and P_{dr}.

Using a reference pressure γ/w_{i} and expressing the different quantities as functions of θ^{a}, $w_{\text{i}}/w_{\text{o}}$, w_{o}/b and w_{i}/b, Eq. (26) reads in a nondimensional form

$$\begin{aligned}\overline{P_{\text{dr}}} \simeq{}& \left[2\frac{w_{\text{o}}}{b}\frac{w_{\text{i}}}{b}\left(\tan\frac{\theta^{\text{a}}}{2}\right)^{-1} - \left(\frac{w_{\text{i}}}{b}\right)^2\right]\frac{(\theta^{\text{a}})^3}{\Gamma} \\ &+ \left[1 + \cos\left(2\arctan\frac{w_{\text{i}}}{2w_{\text{o}}}\right)\right]\frac{w_{\text{i}}}{w_{\text{o}}} \\ &+ \left[\frac{2w_{\text{i}}}{b} + \frac{w_{\text{i}}}{w_{\text{o}}}\right]\left(1 - \cos\theta^{\text{a}}\right).\end{aligned} \tag{27}$$

5.2.3. Summary of the model

The geometrical condition provides a relation between L_{crit} and θ^{a} (Eq. (19)) while θ^{a} may be related to P_{dr} using the pressure balance of Eq. (26). For a given value of θ^{a}, we are now able to estimate the value of P_{dr} corresponding to L_{crit}. By varying θ^{a} from $\pi/6$ to $\pi/3$, we obtained the results plotted in their dimensionless form in Fig. 12, using $\Gamma = 20$ which is the value obtained from straight channel experiments. The quantitative and qualitative behaviors of the theoretical transition are in good agreement with the experimental data.

6. Conclusion

Our experiments on plug propagation in straight microchannels of rectangular cross section showed good agreement with previous studies in capillaries with circular sections [1], in spite of the large aspect ratio of our channels. In particular, the two principal radii of curvature could be used to account for the capillary effects at the advancing and receding interfaces and

effects of draining in the corners could be ignored for sufficiently fast propagation of the plugs.

Experiments through bifurcations show three distinct behavior regimes: blocking of the plugs at the bifurcation for small driving pressures, rupture and channel reopening, or splitting into two daughter plugs. The transitions between these three behaviors may be explained by invoking geometric constraints combined with capillary effects for the case of blocking, or a visco-capillary balance for the rupture vs splitting transition.

These results reproduce some of the known phenomenologies in pulmonary airway flows and geological flows, such as the existence of threshold pressures [10,14,15] or the different mechanisms of transport of a liquid bolus [16,17]. However, they benefit from having a well described geometry and direct access to the complete plug dynamics at all times. Combined with the advantages of microfluidic fabrication techniques, this study will lead to new experimental models of network dynamics, with implications in biofluid or porous media flows.

Acknowledgment

The authors acknowledge helpful discussions with José Bico and Matthias Heil.

References

[1] J. Bico, D. Quéré, J. Colloid Interface Sci. 243 (2001) 262–264.
[2] P.G. de Gennes, Rev. Mod. Phys. 57 (1985) 827–863.
[3] D. Halpern, O.E. Jensen, J.B. Grotberg, J. Appl. Physiol. 85 (1998) 333–352.
[4] R. Lenormand, C. Zarcone, SPE Proc. (1984) 13264.
[5] S.R. Quake, A. Scherer, Science 290 (2000) 1536–1540.
[6] H. Song, J.D. Tice, R.F. Ismagilov, Angew. Chem. Int. Ed. 42 (2003) 768–772.
[7] J.N. Lee, C. Park, G.M. Whitesides, Anal. Chem. 75 (2003) 6544–6554.
[8] P. Aussillous, D. Quéré, Phys. Fluids 12 (2000) 2367–2371.
[9] H.A. Stone, A.D. Stroock, A. Ajdari, Annu. Rev. Fluid Mech. 36 (2004) 381–411.
[10] R. Lenormand, J. Fluid Mech. 135 (1983) 337–353.
[11] R.L. Hoffman, J. Colloid Interface Sci. 50 (1975) 228–241.
[12] C. Treviño, C. Ferro-Fontán, F. Méndez, Phys. Rev. E 58 (1998) 4478–4484.
[13] F.P. Bretherton, J. Fluid Mech. 10 (1961) 166.
[14] A. Majumdar, A.M. Alencar, S.G. Buldyrev, Z. Hantos, Z.H. Stanley, B. Suki, Phys. Rev. E 67 (2003) 031912.
[15] B. Legait, C. R. Acad. Sci. Paris, Sér. II 292 (1981) 1111–1114.
[16] F.F. Espinosa, R.D. Kamm, J. Appl. Physiol. 86 (1999) 391–410.
[17] K.J. Cassidy, N. Gavriely, J.B. Grotberg, J. Biomech. Eng. 123 (2001) 580–590.

Chapter 3

Droplet manipulation through localized heating

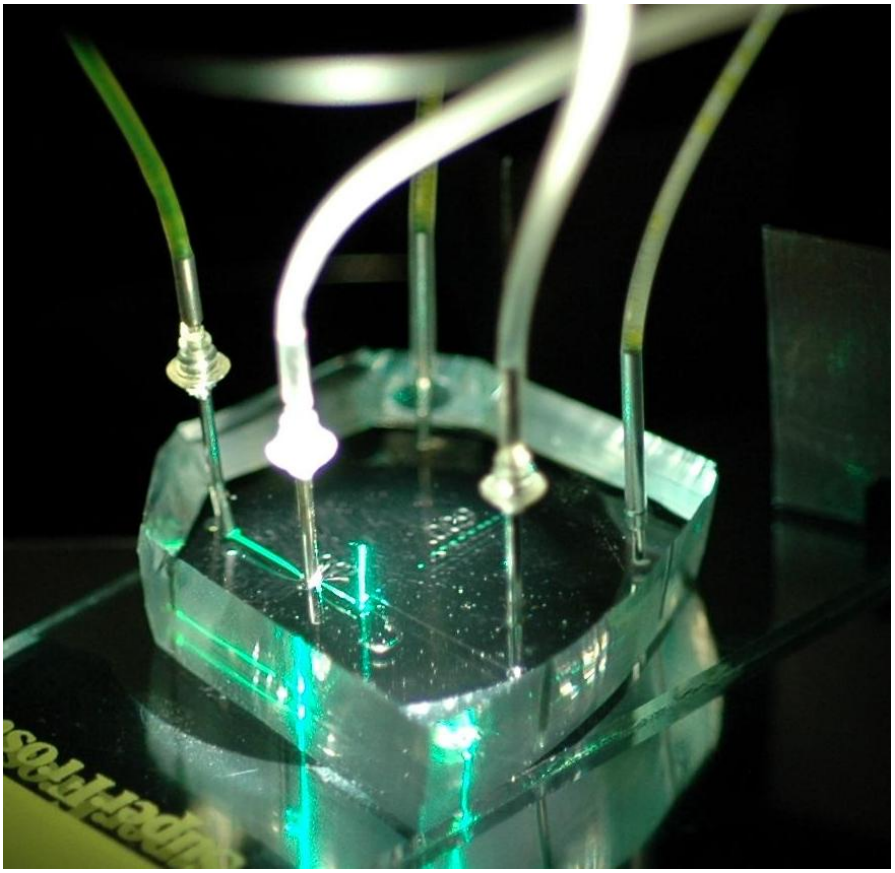

The work presented in this chapter is the result of several years of research and many collaborations. It is not presented in chronological order. The external collaborators who participated on this work were Jean-Pierre Delville, Matthieu Robert de Saint Vincent, Régis Wunenburger (all from U. Bordeaux I); François Gallaire (U. Nice); David McGloin and Dan Burnham (U. Saint Andrews). At LadHyX, the quantitative experiments were performed by Maria-Luisa Cordero and Emilie Verneuil.

3.1 Manipulating drops with a focused laser

We now focus on the manipulation of droplets in microfluidic circuits. Two guiding principles seemed important in developing manipulation techniques which lead to our early experimenting with lasers in microchannels. The first principle was to take advantage of scaling laws favorable to miniaturization such as by using surface phenomena, rather than body forces which become weak at small scales. Second, our design strategy was to simplify the microfabrication and minimize the cost of the channels, which is achieved by fabricating the simplest PDMS channels and not requiring electrode deposition nor multi-layer lithography.

With these general principles in mind, the approach that we converged upon was the use of a laser to induce Marangoni flows on the surface of droplets, thus satisfying the two above criteria. Furthermore, since optical manipulation techniques are well developed, namely for the use with optical tweezers [59], the approach seemed technically feasible, even though it was rather risky. Indeed, no one had demonstrated the manipulation of microfluidic drops larger than a few microns with lasers at the time when our project was initially proposed (and funded). Optical forces, which generate less than nanoNewtons, seemed too weak to be used as a backup in case the Marangoni effect was not obtained.

The first effect that was observed, once we applied laser-heating to a water-oil interface, is shown in Fig. 3.1. This figure shows a cross-shaped microchannel in which oil is forced from the top and bottom channels and water from the left channel. In the absence of laser forcing, water drops in oil are produced in a regular fashion, much like the flow-focusing devices that have become standard. When the laser is illuminated, however, the water-oil interface is completely blocked for times much longer than a typical drop detachment time. In the case shown here, the water is forced at a constant flowrate such that the neck connecting the drop to the water input grows as the drop is held in place, meaning that the drop that finally detaches is larger than the drop produced without the laser action.

The time that the drop is blocked depends on the laser power and its location, though the blocking works equally well for any drop formation geometry. This is shown in Fig. 3.2, where the blocking time is measured as a function of laser position and power, for a cross and T geometries. We observe a linear increase in blocking time with laser power in both cases, with a threshold value below which the drops are not held. Finally, we also observe that the drop size increases linearly with holding time, at least for certain blocking positions for an imposed flowrate.

Note however that the experiments of Figs. 3.1 and 3.2 were all performed using a visible laser (Argon Ion, wavelength $\lambda = 514$ nm). In this case, heating the water is

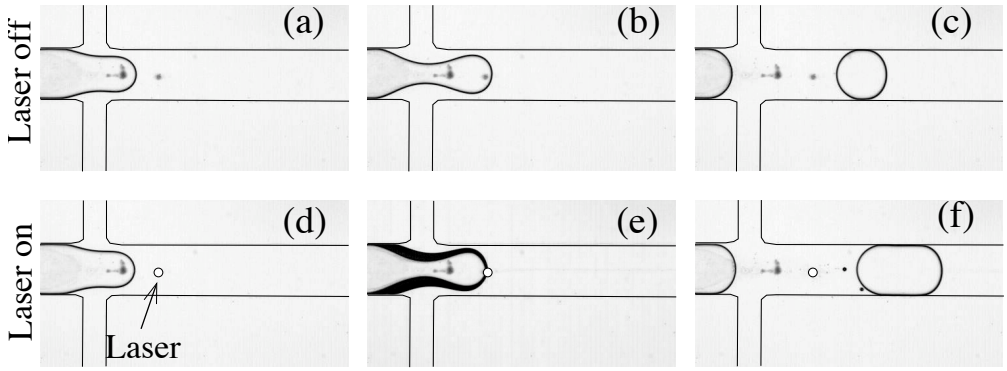

Figure 3.1: Microfluidic valve: In the absence of a laser, water drops are produced in a regular fashion. When the laser is illuminated, the shedding is delayed and the drop that finally forms is larger.

only possible if a dye is dissolved in it; this set of experiments was done using fluorescein because it absorbs at 514 nm. For this reason, it is not clear if the blocking time is determined by intrinsic effects in the drops or by photo-bleaching of the sensitive fluorescein molecules. In later experiments where the water was flowed at constant pressure and where an infrared laser was used with no dye in the water, we were able to achieve blocking times larger than one minute in a true flow-focusing device, although systematic studies were not performed.

These initial experiments seemed extremely promising from a practical point of view since they represented (and still represent) the only available method for modulating the shedding frequency and size of drops, without the need to vary the external flow controls. This lead the CNRS and Ecole Polytechnique to deposit a patent on the manipulation

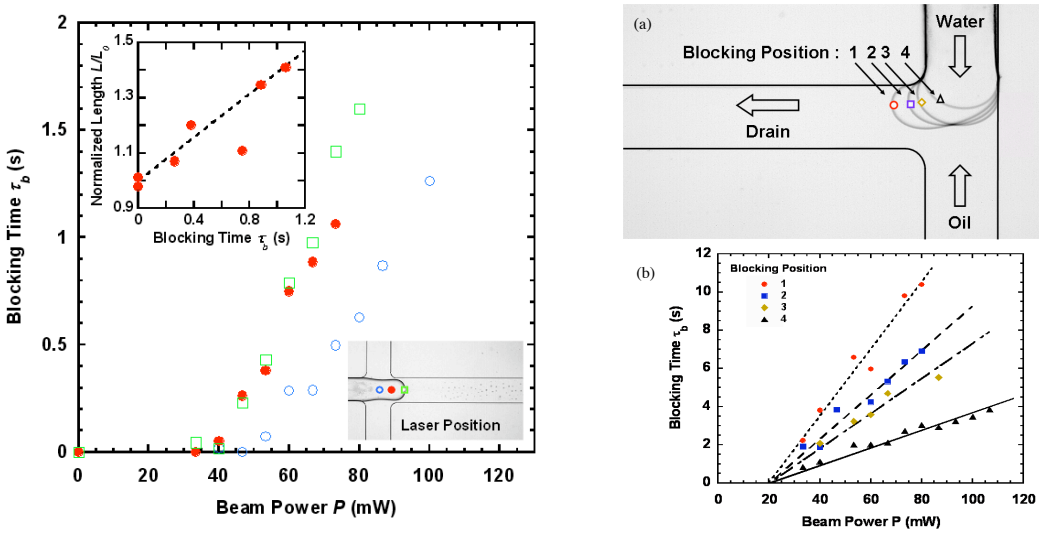

Figure 3.2: Characterization of the blocking time as a function of laser position and power, for two different geometries, using an Argon Ion laser. Note that the phenomenon does not depend strongly on the geometry but the blocking time increases with laser power.

technique of drops and microfluidic systems through laser heating. At the same time, the observed effects also raised a large number of questions, many of which remain open at the time of writing of this memoir, although some advance has been made on certain fronts and will be described below. The next sections describe the theoretical models we have developed and the detailed experimental measurements which allow us to make predictions on the limits of the technique. These are followed, in Section 3.4, by some examples of what can be done with this approach, first with a simple Gaussian laser spot, then using more complex beam-shaping and dynamic holographic techniques in Section 3.5.

3.2 How does it work?

The initial observations were difficult to understand since the physical origin of the force holding the drop were unknown. Indeed, the classical Marangoni forcing, as described for example by Young *et al.* [124], is shown in Fig. 3.3. In this standard picture, the surface tension decreases at the hot region relative to the cold region, which leads to a flow along the surface of the drop that is directed from the hot to the cold side. This drives the outer fluid to travel towards the cold side and the drop to migrate up the temperature gradient, by reaction. This forcing has been demonstrated by experiments and simulations [124, 88, 75] and it was not clear to us how the Marangoni effect could generate a pushing rather than a pulling force on the interface. Moreover, optical forces were ruled out for being too weak to trap a drop with a radius of a few hundred microns.

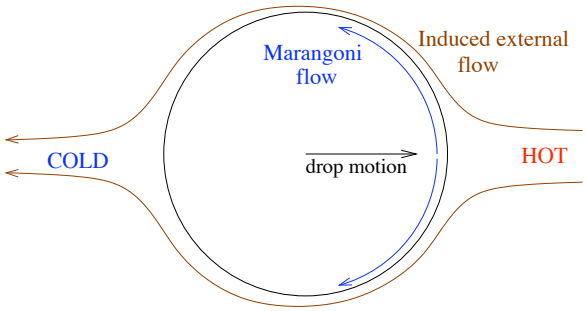

Figure 3.3: Classical view of a "swimming drop" which is subject to a temperature gradient. In the classical picture, drops migrate to the hot side.

However, the puzzle begins to clarify when particles are suspended in the fluids in order to trace the flows, as shown in Fig. 3.4. Surprisingly, the flows are directed towards the hot region, indicating an anomalous Marangoni effect which causes an increase in surface tension with temperature. Owing to the linearity of the Stokes equations, one therefore expects that changing the sign of the Marangoni flow will lead to changing the sign of the force on the drop. This indicates that the origin of the repulsive force on the drop may be of Marangoni origin, given that the flows are directed towards the hot region along the interface.

The hydrodynamic model that was developed assumes a circular water drop placed in a narrow gap with infinite lateral extent. This is similar to the Hele-Shaw model, although we will look for the effects of shear on the drop, meaning that we will look for

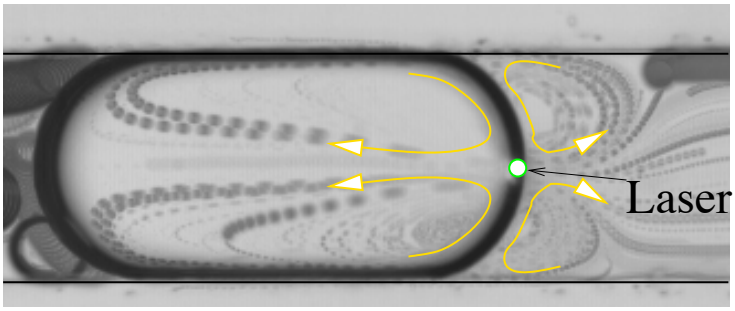

Figure 3.4: Streaklines, inside and outside the drop, of the flows induced by the laser heating. The arrows show that the flows are directed towards the hot regions along the interface, indicating an anomalous Marangoni effect.

departures from potential flow theory. The basic image we would like to understand is sketched in Fig. 3.5, which shows a drop submitted to an external flow going from the left to the right. If the laser is able to stop the drop, the net effect due to the heating needs to exactly counterbalance the drag force felt due to the external flow.

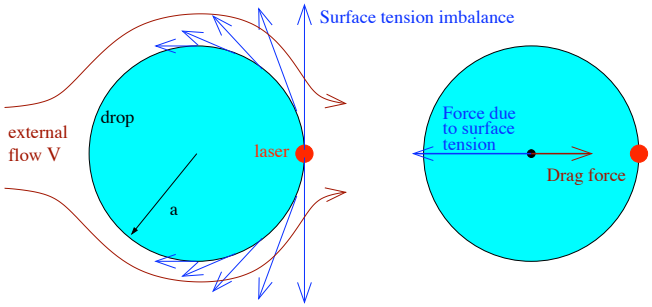

Figure 3.5: A drop is submitted to an external flow from left to right. The net effect due to the Marangoni effect balances the drag due to this flow.

An estimate of the necessary force can therefore be obtained by estimating the drag force on a drop in a narrow gap. This can be obtained from Ref. [90], where the force acting on the drop is given as

$$F_{\mathtt{drag}} \simeq \frac{\pi \mu_{\mathtt{oil}} R^2}{h} \left[1 + \lambda + \frac{h}{4R} \left(\frac{2\lambda}{1+\lambda} \right) \right] V, \tag{3.1}$$

where $\lambda = \mu_{\mathtt{water}}/\mu_{\mathtt{oil}}$ is the viscosity ratio, R is the drop radius, h is the gap height, and V is the velocity of the oil at infinity. A numerical application of typical values $R = 100$ μm, $h = 10$ μm, and $V = 1$ mm/s, yields a drag force of about 1 μN. This force is many orders of magnitude larger than forces produced by optical techniques, thus completely ruling out the possibility of an optical gradient origin of the force. It is also several orders of magnitude larger than forces produced by dielectrophoresis [5].

The force generated by the thermocapillary convective flow on a droplet is investigated through the depth-averaged Stokes equations, since our channels have a large width/height aspect ratio. We limit ourselves to the main features of the flow, the detailed derivations being left as an exercise to the reader [21, 29]: a circular drop of radius

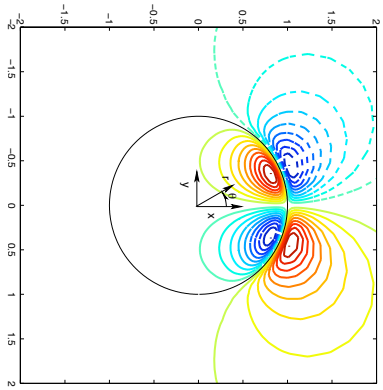

Figure 3.6: Streamfunction contours obtained from the depth-averaged model described in the text. Blue and red contours indicate counterclockwise and clockwise flows, respectively.

R is considered in an infinite domain and the flow due to the Marangoni stresses is evaluated. Assuming a parabolic profile in the small dimension (h) and introducing a streamfunction for the mean velocities in the plane of the channel, the depth averaged equations, valid in each fluid, are

$$\left(\frac{1}{r}\frac{\partial}{\partial r}r\frac{\partial}{\partial r}+\frac{1}{r^2}\frac{\partial^2}{\partial\theta^2}\right)\left(\frac{1}{r}\frac{\partial}{\partial r}r\frac{\partial}{\partial r}+\frac{1}{r^2}\frac{\partial^2}{\partial\theta^2}-\frac{12}{h^2}\right)\psi=0, \tag{3.2}$$

where the depth-averaged velocities may be retrieved from $u_\theta = -\partial\psi/\partial r$ and $u_r = 1/r(\partial\psi/\partial\theta)$. The kinematic boundary conditions at the drop interface ($r = R$) are zero normal velocity and the continuity of the tangential velocity. The normal dynamic boundary condition is not imposed since the interface is assumed to remain circular, which is consistent with our experimental observations, e.g. Fig. 3.4. Finally, the tangential dynamic boundary condition, which accounts for the optically-induced Marangoni stress, is

$$\mu_1 r\frac{\partial}{\partial r}\left(\frac{u_\theta^1}{r}\right)-\mu_2 r\frac{\partial}{\partial r}\left(\frac{u_\theta^2}{r}\right)=-\frac{\gamma'}{r}\frac{dT}{d\theta}, \tag{3.3}$$

where $\mu_{1,2}$ are the dynamic viscosities and $u_\theta^{1,2}$ are the velocities in the drop and the carrier fluid, respectively. $\gamma' = \partial\gamma/\partial T$ is the surface tension to temperature gradient, which is positive in our case.

For simplicity, we approximate the steady state temperature distribution using a Gaussian form $T(x,y) = \Delta T\exp[-((x-R)^2+y^2)/w^2]$, where ΔT is the maximum temperature difference between the hot spot and the far field and w corresponds to the size of the diffused hot spot, which is significantly larger than the laser waist ω_0 (see Sec. 3.3). The equations are nondimensionalized using ΔT as temperature scale, R as length scale, $R\gamma'\Delta T$ as force scale and $\frac{R(\mu_1+\mu_2)}{\gamma'\Delta T}$ as time scale, the remaining nondimensional groups being the aspect ratio h/R, the nondimensional hot spot size w/R and the viscosity ratio $\bar{\mu} = \mu_2/(\mu_1+\mu_2)$.

A typical predicted flow field solving the above numerical formulation is shown in Fig. 3.6, in which the four recirculation regions are clearly visible. The velocity gradients display a separation of scales in the normal and tangential directions, as observed from

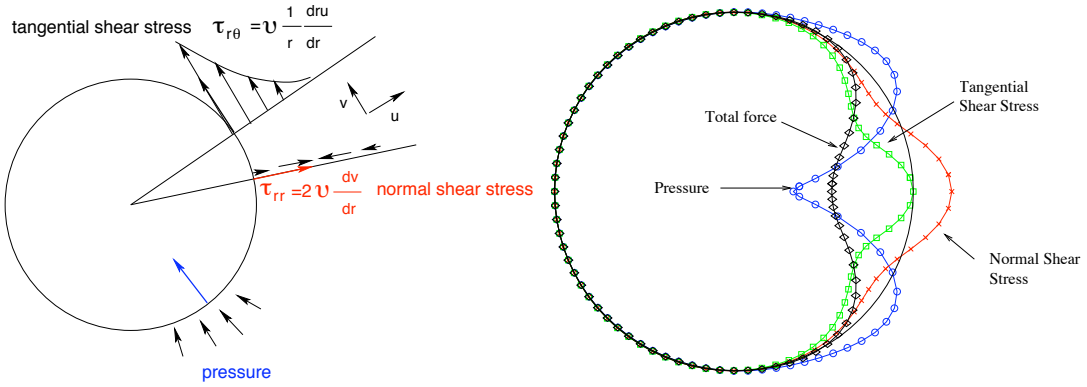

Figure 3.7: Left figure: Definition of the three stress fields that contribute to applying a force on the drop. Right figure: Projections of the three fields along the x direction, along with their sum. The solid black circle represents the zero level.

the distance between the streamlines in the two directions. Indeed, it may be verified that the velocities vary over a typical length scale h/R in the normal direction, while the tangential length scale is given by w/R.

Along with this flow field, we compute the pressure field, as well as the normal ($\bar{\sigma}_{\bar{r}\bar{r}} = 2\bar{\mu}\partial\bar{u}_{\bar{r}}/\partial\bar{r}$) and tangential ($\bar{\sigma}_{\bar{r}\theta} = \bar{\mu}\left(1/\bar{r}\partial\bar{u}_{\bar{r}}/\partial\theta + \partial\bar{u}_{\theta}/\partial\bar{r} - \bar{u}_{\theta}/\bar{r}\right)$) viscous shear stresses in the external flow, defined in Fig. 3.7(left). These projections on the x axis, shown in Fig. 3.7(right), are then summed and integrated along θ to yield the total dimensionless force ($\bar{F}$) on the drop. Note that the global x component of the force is negative and therefore opposes the transport of the drop by the external flow. The y component vanishes by symmetry and the integral of the wall friction may be shown to be zero since the drop is stationary.

Numerically computed values of $\bar{F}R/h$ are shown by the isolated points in Fig. 3.8 as a function of w/R, for different values of the aspect ratio h/R. The points all collapse on a single master curve, displaying a nondimensional scaling law $\bar{F} \propto wh/R^2$, for small w/R.

The dimensional form of the force can be obtained from scaling arguments, for small h/R and w/R, by considering the three contributions separately and noting that the velocity scale in this problem is imposed by the Marangoni stress. Using the separation of scales along the azimuthal and radial directions, Eq. 3.3 becomes

$$(\mu_1 + \mu_2)\frac{U}{h} \sim \frac{\Delta T\gamma'}{R}\frac{R}{w}, \tag{3.4}$$

where the '$\sim$' is understood as an order-of-magnitude scaling. This yields the characteristic tangential velocity scale

$$U \sim \frac{\Delta T\gamma'}{\mu_1 + \mu_2}\frac{h}{w}. \tag{3.5}$$

The force due to the tangential viscous shear is then obtained by multiplying $\sigma_{r\theta} \sim \mu_2 U/h$ by $\sin\theta \simeq w/R$ and integrating on the portion $w \times h$ of the interface,

$$F_t \sim \mu_2\frac{U}{h}\frac{w}{R}wh = \frac{\mu_2}{\mu_1 + \mu_2}\Delta T\gamma'\frac{hw}{R}. \tag{3.6}$$

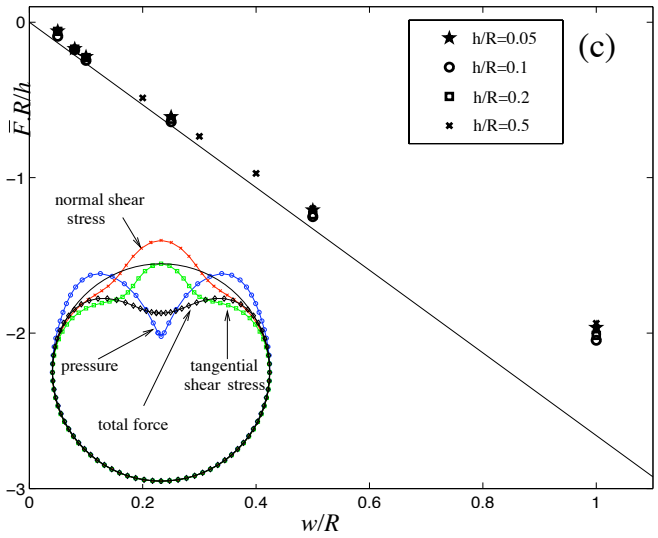

Figure 3.8: Calculated force (numerical and analytical values) as a function of the hot region size. Note that the force is negative (pushing the drop left) and increases with decreasing drop size.

The force due to the normal viscous shear can be shown to scale like $F_n \sim \frac{h}{R} F_t$ and is therefore negligible. The pressure force, on the other hand, derives from a balance between the pressure gradient and the radial second derivative of velocity. In the present circular geometry, similar scaling arguments yield a law for the contribution of the pressure force F_p, which follows the same scaling as F_t, resulting in the same scaling law for the total force F. A rigorous derivation [57] yields the final form of the force including the prefactor:

$$F = -2\sqrt{\pi}\frac{\mu_2}{\mu_1 + \mu_2}\Delta T \gamma' \frac{hw}{R}. \tag{3.7}$$

This expression is represented (once non-dimensionalized) by the straight line on Fig. 3.8 and agrees very well with the numerically computed values.

The theoretical treatment brings out two length scales, h/R and w/R. While h and w can be thought of as determining the typical scales for velocity variations in the radial and azimuthal directions, R enters the force scaling as a local radius of curvature rather than the actual size of the drop. It is therefore not surprising that the blocking force should *increase* as R decreases. On the other hand, the drag force due to the external flow scales as R^2 [90], implying that the laser power necessary to counterbalance the drag quickly decreases with the drop size.

3.3 Detailed measurements

Although the analytical study above provides support for the thermocapillary origin of the force, many questions remain open regarding the applicability of the technique and on the detailed physical mechanisms at play. For this, we undertook a series of measurements in order to determine three parameters: **(i)** the dynamics and statics of the thermal field, **(ii)** the dynamics of the flow field setup, and **(iii)** the distribution of surfactant in the oil phase.

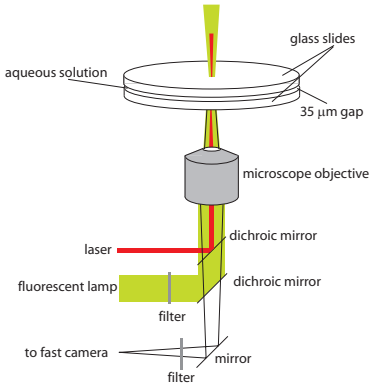

Figure 3.9: Temperature measurement setup.

These studies were undertaken at LadHyX using an infrared laser (wavelength $\lambda = 1480$ nm) which directly heats the water molecules, therefore not requiring the addition of a dye to provide the heating. This allowed us to use fluorescence to obtain physical measurements. This work is currently being written up for publication [38, 121].

3.3.1 Temperature field measurements

The temperature fields were measured in a quiescent water layer, sandwiched between two glass plates, as shown in Fig. 3.9. For these measurements, we took advantage of the sensitivity of the quantum yield of Rhodamine B to temperature, which decreases with increasing temperature of the solution [99]. The calibration of the thermal response of the Rhodamine fluorescence was first made by imposing a known temperature with a water bath, after which we could map directly the fluorescent intensity to temperature.

For the temperature profile measurements, the aqueous solution of Rhodamine was heated with the laser and images were taken at 500 frames per second, in order to observe the temperature increase at the laser position. Care had to be taken, however, to account for the depletion of the dye molecules due to thermophoresis (Soret effect) [48]. This was achieved by normalizing the fluorescence of Rhodamine B with images of Rhodamine 101, a similar molecule which is not sensitive to temperature.

The temperature profiles, as a function of distance r from the laser and time t, were well fitted with a Lorentzian curve

$$T(r,t) = T_0 + \frac{\Delta T(t)}{1 + (r/\sigma(t))^2}, \tag{3.8}$$

where $\sigma(t)$ gives the width of the profile at half height and $\Delta T(t)$ is the maximum temperature rise as shown on Fig. 3.10, which also shows the evolution of ΔT and σ as a function of time. We observe a rapid response of the maximum temperature, which reaches its steady-state value after less than 10 ms, due to the small volume being heated. The final Lorentzian profile is set up over a longer time scale, requiring a few tens of ms.

The steady state temperature profile was also measured and provided the value of the maximum temperature as a function of distance from the laser beam. The values of σ ranged between 10 and 30 μm for the laser powers used in our experiments.

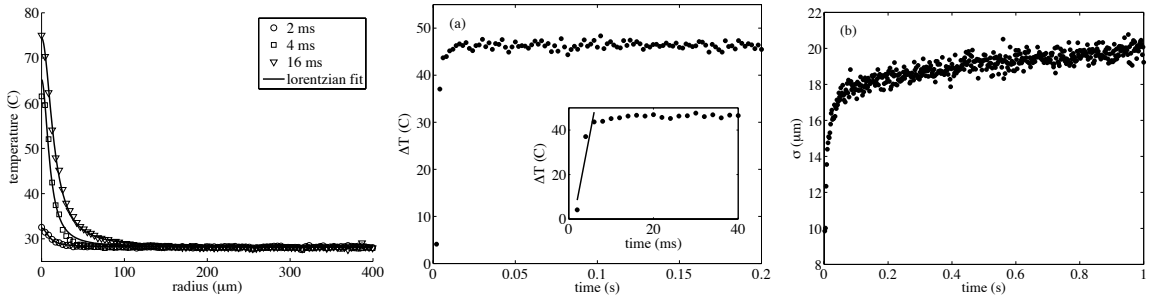

Figure 3.10: Profile of the temperature rise for the initial few milliseconds of heating (left). Transient increase in the maximum temperature (middle) and the width of the Lorentzian curve (right) as a function of time.

3.3.2 Time scale for activation

A fundamental limit on the applicability of the technique depends on the time required for the activation of the thermocapillary process. One measure of this time scale may be to ask how fast the drops can flow past the laser and still be stopped. This was tested in the channel of Fig. 3.11, where drops are formed at the first T junction and transported into the "test section", where they are stopped by the laser, while the oil is allowed to continue flowing through the bypass. A second oil inlet is used to vary the velocity of the drops without affecting the formation frequency and size.

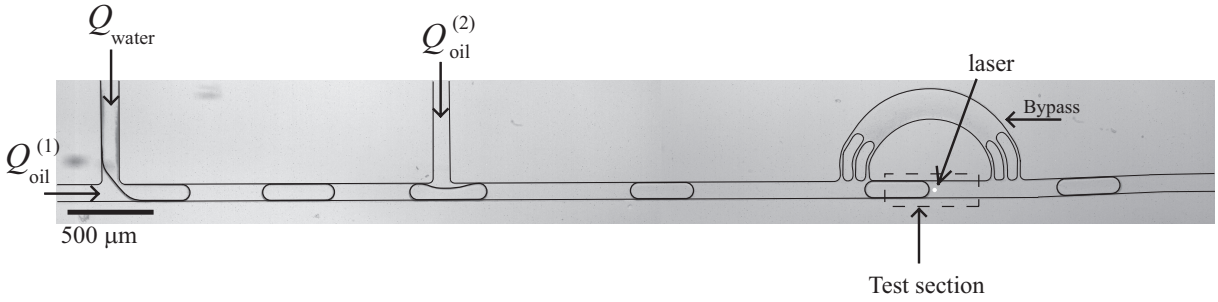

Figure 3.11: Channel for measuring force and roll formation time scale.

The experiment consists of blocking the drop advance in the test section for different total flowrates, $Q = Q^1_{\texttt{oil}} + Q^2_{\texttt{oil}} + Q_{\texttt{water}}$. The drops were seeded with fluorescent particles and velocity fields inside the drops were measured using Particle Image Velocimetry (PIV), as shown in Fig. 3.12 where the steady state velocity field (Fig. 3.12(b)) is compared with a streak photo showing the recirculation rolls (Fig. 3.12(a)). We see that the PIV captures well the flow field far from the laser position but gives poor results near the hot spot, partly because of the very high velocities and in part due to the decline if the fluorescence intensity.

In order to extract a time scale for the setup of the rolls, the flux $\varphi(t)$ is measured across the line ℓ, drawn on Fig 3.12(b). By continuity, we know that the flux passing through ℓ must return through the the region d near the interface (Fig. a). Noting furthermore that the geometry of the rolls does not seem to vary, the measurement of $\varphi(t)$ yields a time scale for the setup of the thermocapillary flow near the interface.

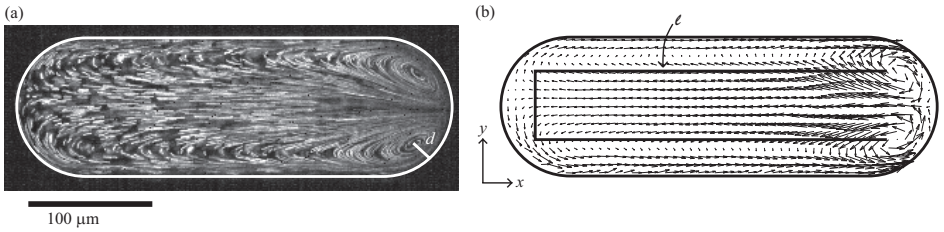

Figure 3.12: Sample PIV field and measurement region.

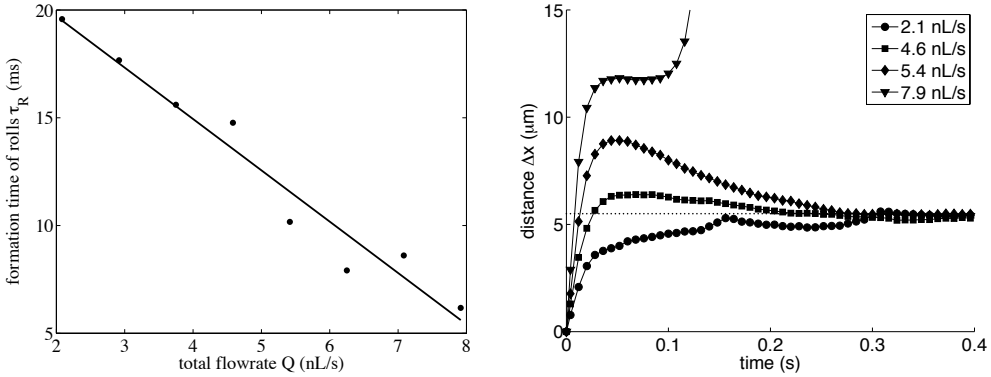

Figure 3.13: Time scale for setup of rolls (left) and mean position of the drop from integrated PIV field (right).

This time scale, τ_R, is plotted on Fig. 3.13(left) for a fixed laser power ($P = 76$ mW) and different flowrates Q. In this figure, we observe that the characteristic time decreases as the drop velocity increases, which suggests that the time to form the rolls is dictated by the time required to enter the Gaussian laser spot. Furthermore, the fastest drop that can be stopped displays a flow setup time of 6 ms, which is close to the time required to reach the maximum temperature from the heating experiments discussed above. These results suggest that the limit on the speed of actuation of a drop is given by the time required to heat the liquid enough to create the Marangoni rolls.

The PIV data can also be used to obtain the position of the drop's center of mass, as shown in Fig. 3.13(right) for a few representative drops, by integrating the velocity data in time. The position thus measured is precise since it relies on the average of many velocity vectors. We see that drops that approach slowly are slowed down continuously to a stop (circles), while drops advancing more quickly go through an overshoot before retracting back to their final position. Finally, the ultimate drop that is held remains stationary for only about 100 ms, but never relaxes back to the equilibrium position.

Detailed analysis of these results suggests that, in addition to the heating and the creation of a Marangoni flow, the drop must also adapt its shape to the flow conditions, which involves a second, slower, time scale. This can be used to explain why the fastest drop is stopped for a short period, but doesn't remain blocked: If the front interface has passed most of the laser spot, the shape adaptation will lead to the laser moving further into the drop and therefore reducing the temperature gradient along the interface, thus de-blocking the drop.

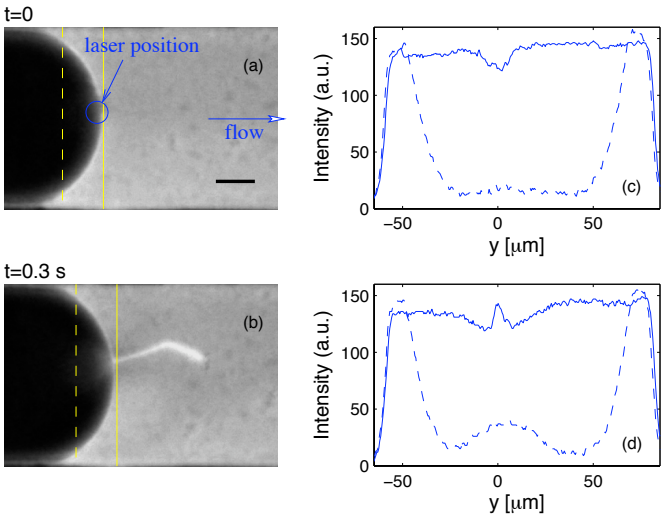

Figure 3.14: Fluorescence images showing the surfactant concentration as the drop begins to be heated. Parts (a) and (b) show the drop at the moment of heating and 300 ms later. Parts (c) and (d) show fluorescence intensity cuts at the positions marked by the solid and dashed lines on the images.

3.3.3 Surfactant transport

Finally, the third limitation on the technique is to understand the dependence on the particular fluids and surfactants. For this, we had to understand the source of the anomalous Marangoni flow and the relation between the heating and the surfactant transport. Measurements made using the pendant drop technique confirmed the classical linear decrease of the interfacial tension with temperature for our fluid solutions. This motivated us to look at transient effects.

In the same test section of Fig. 3.11, we performed an experiment where the surfactant micelles were marked with Rhodamine 101, which acts as a co-surfactant to the Span 80. As discussed in Section 3.3.1, Rhodamine 101 is not sensitive to temperature changes. Furthermore, it was observed that the dye is not soluble in pure hexadecane but that it was strongly solubilized when the hexadecane contained a large concentration of surfactant. This "micellar solubility" implies that the surfactant molecules could be used as tracers of the micelles. Furthermore, it was observed that the partition between the oil and the water phases was very strongly biased towards the oil phase, which means that the drops appear as dark regions in a fluorescent oil phase.

In Fig. 3.14, two snapshots are shown at the moment at which the drop reaches the laser and 300 ms later. The drop, which travels from left to right, displays an initial decrease in fluorescence very close to the laser, as shown by the solid line in part (c). We interpret this decrease in fluorescence as a decrease in the surfactant concentration at this location, which is coherent with the increase in surface tension. At later times, the fluorescence field becomes strongly inhomogeneous, indicating strong redistributions of the surfactant molecules. In particular, the rolls transport a thin highly concentrated jet away from the drop interface.

These results do not to provide a complete scenario of surfactant redistribution,

which would be highly nonlinear and would involve several coupled phenomena. Instead, they point to significant redistributions in surfactant concentration, which confirms that the dynamics of the redistribution can play a major role in the surface tension variations.

3.4 What can you do with it?

Going back to the applications of the technique in real microfluidics situations, we now focus on the droplet operations that can be achieved by locally heating a water-oil interface with a focused laser. Recall that Joanicot and Ajdari had identified certain key operations that had to be controlled in order for droplets to be viable as microfluidic reactors: *fabrication, sorting, storage, fusion, breakup, and trafficking.* Above, we have seen that fabrication of drops could be controlled, namely by controlling the frequency and size of drops dynamically. The rest of this section demonstrates the implementation of the other operations, to which we may add synchronization, an important operation when drops must interact. In the next section, we also introduce more complex operations, such as order switching, by using more complex optical techniques.

3.4.1 Drop fusion

The simplest operation to understand is the one that leads to the fusion of two droplets, shown in Fig. 3.16. Drops in microchannels are stabilized by the presence of surfactant through several mechanisms. Particularly, the presence of a large concentration of surfactants introduces an increased resistance to flow between the two interfaces, which thus prevent the trapped oil film from draining. Other interactions between the surfactants on the two interfaces can also retard the merging, for example through electrostatic or steric repulsion.

The localized heating can play two major roles in inducing the fusion of two drops. The first role is to deplete the surfactant molecules from the surface, as we have seen above, while the second role is to produce recirculation rolls which can actively drain the lubrication film between the two drops, as shown schematically in the sketch of Fig. 3.15. Here, we show the arrows pointing away from the laser spot; although the flow in the plane of the channel is pointing towards the hot region, it will be associated with a secondary recirculation flow, normal to the plane, which drains the fluid near the interface away from the hot spot.

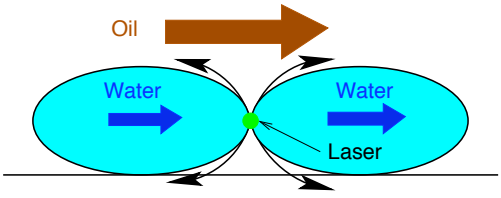

Figure 3.15: Sketch of the fusion mechanism: The laser drains the lubrication oil film.

We observe that the heating may be used to induce droplet merging, either in the case of isolated drops (left sequence in Fig. 3.16) or in the case of a compact flow of droplets, as shown in the right sequence of the same figure. In the case of isolated drops,

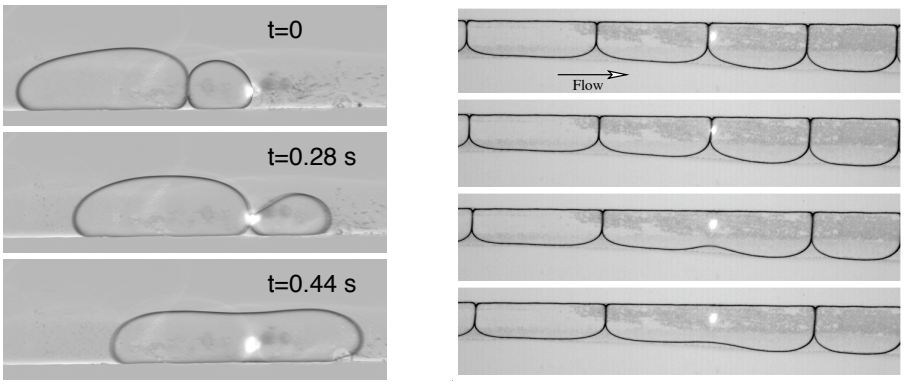

Figure 3.16: Fusion in the case of isolated drops (left) and a train of drops (right). Note that the localized heating produces localized fusion events and this compares favorably with the results of Priest et al. [96]

the laser is first used to block the advance of the initial drop until the second one collides with it, at which point the two drops advance together, merging when the interfaces pass the laser spot. In the case of the compact flow of drops, the drops do not need to be synchronized and a lower laser power can be used to induce the merging event.

3.4.2 Synchronization

Furthermore, the synchronization of drops in order to combine their contents is a major challenge for lab-on-a-chip operations. Passive synchronization and alternation of drops from two sources was demonstrated by finely tuning the different water and oil flowrates [4]. This approach, however, is only useful in the simplest cases where only two droplet streams are involved and the downstream conditions are constant. A more robust approach would be for a downstream drop to delay its formation and wait for the upstream drop to catch up with it, at which point the two merge together. This corresponds, in our terms, to a combination of a valve and a fusion mechanism; once the two building blocks exist, combining them becomes a simple matter as shown in Fig. 3.17.

Here, drops are formed at successive T-junctions and flow down the same exit channel. In the absence of the laser forcing (Fig. 3.17-left), the drop formation is not synchronized and neither do they merge if they do come into contact. The situation is different in the presence of the laser, which holds the downstream interface in place (Fig. 3.17a) until the upstream drop is formed and collides with it (Fig. 3.17b). Since the upstream drop completely blocks the channel, the hydrodynamic drag on the two-drop system becomes too large and the two drops start to flow again (Fig. 3.17c), merging together when their touching interfaces pass the laser (Fig. 3.17d).

The valve and fusion actions here are performed with only one laser spot, showing how the different building blocks may be superposed by combining the laser action with a geometric constraint. This is done with no overhead in power or complexity with respect to a single operation, demonstrating how the technique may be scaled to a complex lab-on-a-chip involving many operations.

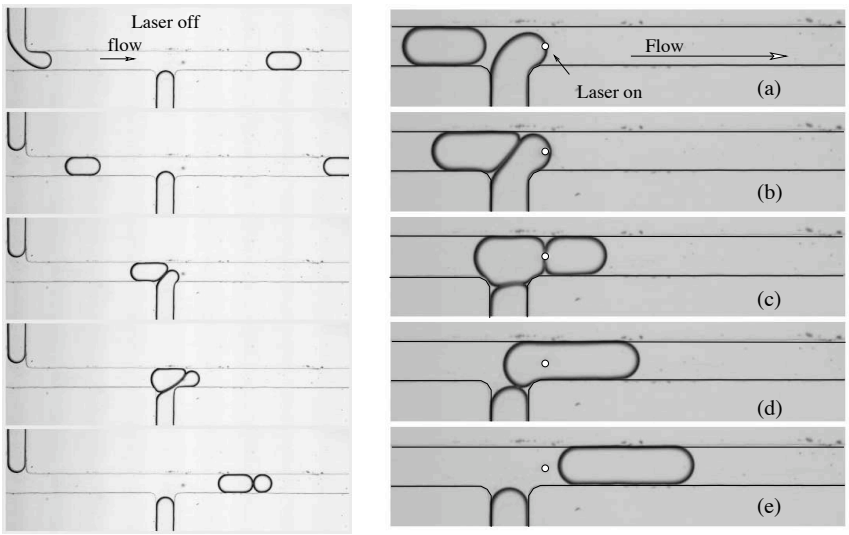

Figure 3.17: A forming drop is blocked by the laser-valve (a) until a second drop, formed upstream, collides with it (b). The collision liberates the front drop (c) and the two merge when their interfaces pass the laser(d). Operating conditions are $Q_{\texttt{water}} = 0.1$ μL/min, $Q_{\texttt{oil}} = 1$ μL/min, $P = 67$ mW and $\omega_0 = 5.2$ μm. The laser position is represented by the white circle.

3.4.3 Routing

The remaining steps after the formation and merging of drops are their transport and division, which involve control over the route they follow at bifurcating channels. Two operations are demonstrated below: sampling a drop, i.e. dividing it into unequal daughter droplets of calibrated size, and sorting. A sampler which uses a combination of channel geometry and laser forcing is shown in Fig. 3.18. We see in it drops that are longer than the channel width and that arrive at a symmetric bifurcation, carried by the oil phase. At the bifurcation, the drops divide into two parts whose lengths in the daughter channels we label L_1 and L_2. We are interested in the ratio $\lambda \equiv \langle (L_1 - L_2)/(L_1 + L_2) \rangle$ which yields $\lambda = 0$ for symmetric drops and $\lambda = 1$ for complete sorting. The brackets $\langle \cdot \rangle$ here denote an average over several drops.

In the absence of the laser (Fig. 3.18a), we measure $\lambda = 0.022 \pm 0.01$ for our microchannel, corresponding to a slight asymmetry in the microfabrication. When the laser is applied in front of one of the two exits, the water-oil interface is asymmetrically blocked at the laser position for a time τ_b, while the other side continues to flow (Fig. 3.18b). After τ_b, both sides of the drop continue forward into their respective channels, but the retardation of the right hand droplet tip produces an asymmetry in the breaking, measured by an increase in λ. Since the blocking time τ_b increases with the laser power, so does the asymmetry in the division, as shown in Fig. 3.18c.

Above a critical power (approximately 100 mW for the present configuration), the drop does not divide but is always diverted into the opposite branch, as shown in Fig. 3.19. This sorting operation may be understood by considering the length of the droplet upstream of the laser: If the upstream length decreases below a critical size of approximately the channel width (corrected by the displacement of the laser with respect to the channel center), the drop takes a circular shape and loses contact with the right hand wall. In

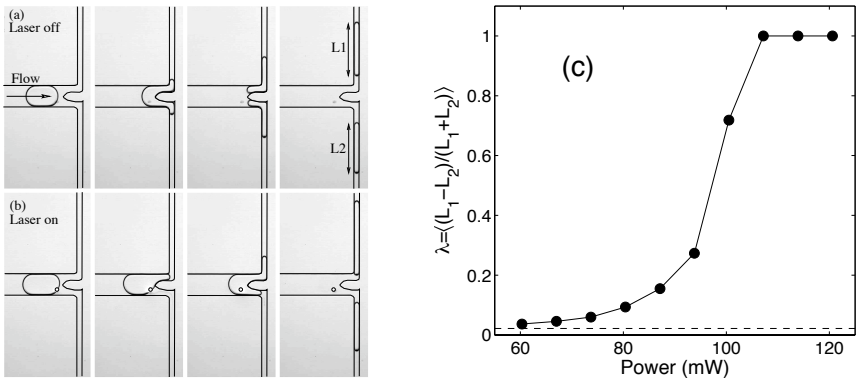

Figure 3.18: Dividing drops asymmetrically: (a) Without laser forcing, a drop at a bifurcation divides into approximately equal daughter droplets. (b) By controlling the laser power (here $P = 93$ mW), we control the pinning time of one side of the interface and thus the asymmetry of the division. Main channel width is 200 μm and the time between images is 0.2 s. Operating conditions are $Q_{\texttt{water}} = 0.02$ μL/min, $Q_{\texttt{oil}} = 0.2$ μL/min, and $\omega_0 = 5.2$ μm. (c) Daughter droplet size dependence on laser power ($\lambda = 0$ is for symmetric drops and $\lambda = 1$ is for the sorter). The dashed line corresponds to the mean value of λ in the absence of the laser.

this case, a tunnel opens for the oil to flow between the drop and the wall and the drop does not divide anymore but is pushed into the left hand channel, as shown in Fig. 3.19.

Finally, a more useful sorting operation can be achieved as shown in Fig. 3.20. Here, the channel outputs are designed asymmetrically, such that drops all passively flow to the top exit channel in the absence of active manipulation. When the laser is applied, the drop can be pushed downward such that its center of mass is now located in the streamlines flowing into the other exit channel. In this way, drops can be selected based on their content, size, or their number.

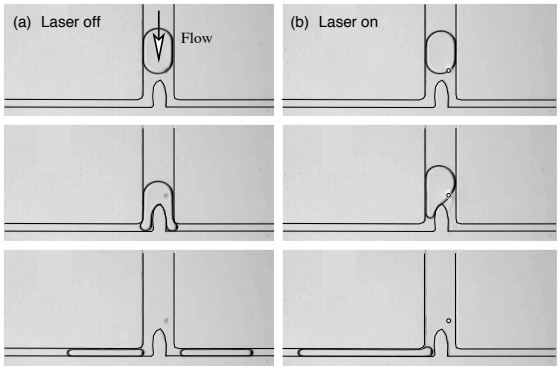

Figure 3.19: A drop without laser heating divides into equal parts. If the laser heating is sufficiently strong, the drop can be completely redirected into one of the two channels.

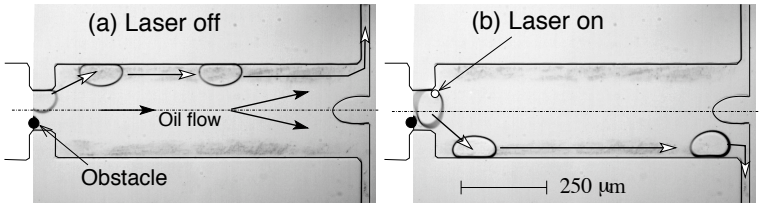

Figure 3.20: Drops naturally flow into the upper channel due to a geometric asymmetry. If the laser is applied, the drops can be sent to the lower channel.

3.5 More advanced manipulation

The possibilities of droplet manipulation can be extended by combining microfluidics with optical holographic techniques, thus taking advantage of the contactless nature of optical manipulation. Indeed, we show below that the use of different laser patterns allows the implementation of complex operations which are not possible with any other methods. We begin by exploring the effect of the shape of the laser focus on the blockage of droplets, while further we demonstrate implementations which show conceptually new operations on drops in microchannels.

Holographic beam shaping was employed to generate the desired patterns of light [28]. We first investigated the minimum optical power, $P_{\min}$, required to block the advance of a drop, for three different shapes: a Gaussian spot with a 1 μm waist, a straight line aligned with the flow direction, and a straight line perpendicular to the flow direction. Both lines were 2 μm in width and 200 μm in length. In these experiments, the microchannels were similar to those shown in Fig. 3.11 with three inlets, two for oil and one for water. Droplet size was determined by the ratio between the flow rates of the first oil inlet $Q_{\text{oil}}^{(1)}$ and the water inlet Q_{water}, which were both kept constant. The second oil flow rate $Q_{\text{oil}}^{(2)}$ was used to tune the total flow rate $Q_{\text{tot}} = Q_{\text{oil}}^{(1)} + Q_{\text{oil}}^{(2)} + Q_{\text{water}}$, keeping in this way the size of the droplets constant while their velocity varied with Q_{tot}.

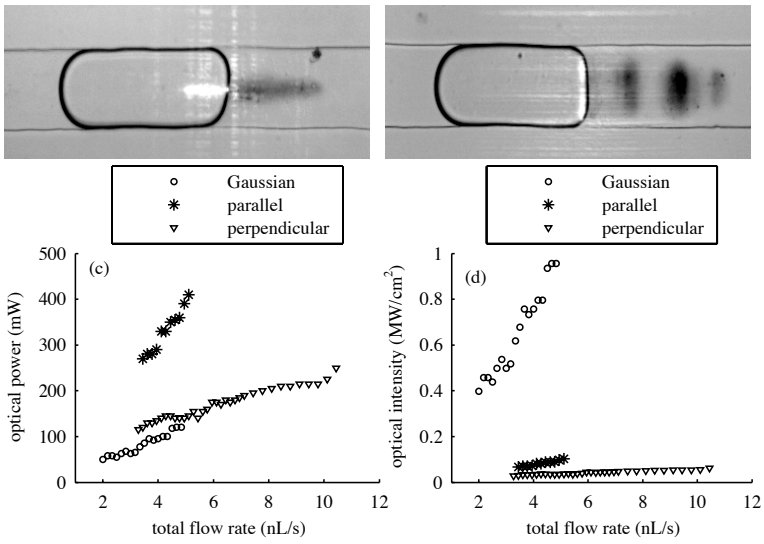

Figure 3.21: Influence of the shape of the laser action.

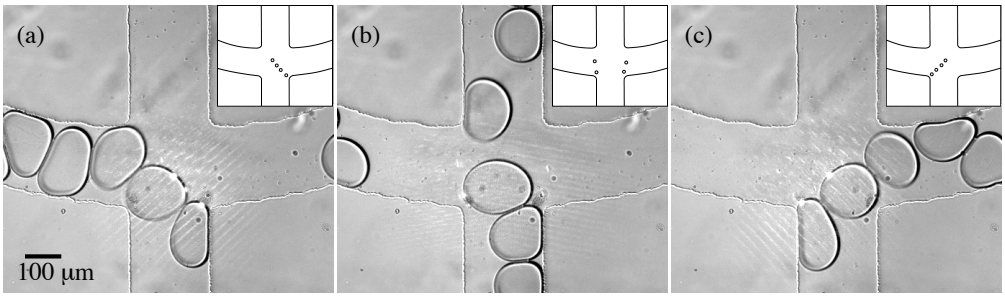

Figure 3.22: Routing drops through three separate exit channels. By changing the holographic pattern, the drops can be directed into the left, right, or front channel.

The first observation, as the drops reach the laser beam, is that the water-oil interface adapts to the laser forcing, as seen in Fig. 3.21(a) and (b). When the line is parallel to the direction of flow, the front interface is flattened and the drop stops after advancing through a significant portion of the line. In the case of a line perpendicular to the flow direction, the surface of the drop is even flatter than in the previous case, taking on the shape of the line.

The minimum laser power for each of the laser distributions is plotted as a function of the total flow rate in Fig. 3.21(c). It scales approximately linearly with the total flow rate but the slopes of the curves and the values of $P_{\min}$ differ for the three cases. The use of a line perpendicular to the flow allows the blocking of drops at higher flow rates, up to more than 10 nL/s. Conversely, even though a lower laser power is necessary to hold the droplets in the case of a Gaussian spot, it was not possible to hold droplets for flow rates higher than about 5 nL/s. This was also the case for the line parallel to the flow.

Moreover, if the pattern intensity is studied instead of the total laser power, the minimum intensity $I_{\min}$ necessary to block a drop is found to be several times higher for a Gaussian spot than for a line distribution (Fig. 3.21(d)). The perpendicular line is found to block the drop for the lowest value of $I_{\min}$. Note that in the case of line patterns, the image is only fully formed in the focal plane of the microscope objective, i.e. measuring a few microns in depth. For the Gaussian spot however, the pattern propagates through the whole sample.

We now consider the applications of such holographic beam shaping and how single spot applications can be extended. The first application is droplet routing, or actively sending droplets into different directions at a trifurcation. Making use of the ability to both dynamically switch the optical patterns projected into the microfluidic channel and the ability to create extended patterns (in this case four spots) we can deflect droplets through large angles and send them into preferred channels. This is shown using a four way cross channel in Figs. 3.19(a)-(c) which shows the droplets being moved to the left, straight, or to the right, respectively. The switching time of the droplets into a given channel is limited only by the update speed of the Spatial Light Modulator (SLM), which ranges from 30 to 60 Hz. It would be straightforward to extend this technique to active sorting, by including some video processing and combining it with the hologram switching (the holograms are pre-calculated and are merely changed based on which direction the droplets need to move in). One could imagine the sorting being based on droplet size, chemical composition, fluorescence measurements or simply the contents of a drop.

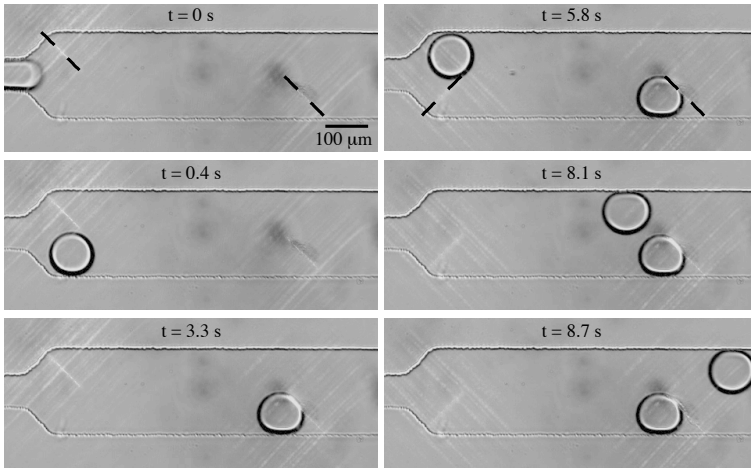

Figure 3.23: The ability to change the hologram and to hold drops for long times allows the switching of droplet order. Note that the lower drop can be held for very long times.

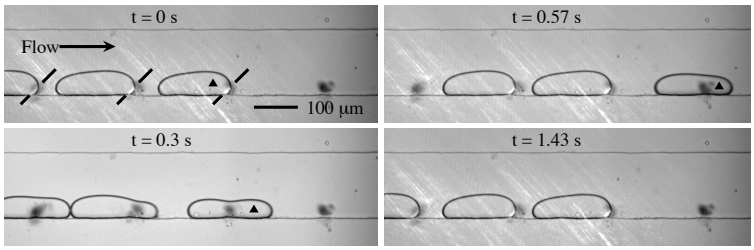

Figure 3.24: Drops arrive from the left and can be shuttled between three laser positions.

The second example uses two line patterns to store droplets at a given point in the channel while rerouting other droplets to move past the stored droplet. The first line upstream is set to move a droplet into one side of the larger channel. The droplet is then stored by the downstream line further along the channel. The first line is then changed so as to move subsequent droplets in the flow past the first droplet, as shown in Fig 3.23. Thus we can store and could interrogate the first droplet without the need to stop the flow, which is important in order to obtain longer interrogation times. Note that the ability to focus the laser to a small area on the drop allows real droplet-level manipulation, contrary to electrical fields which produce a uniform forcing on a region of the microchannel [4]. This is what allows the drop order to be inverted in this case.

The third example, shown in Fig. 3.24, is an extension of the second. Here we are able to trap several droplets at once, first one, then two and finally three using three lines of light. Again this is in the presence of droplets flowing through the channel. We are then able to shuttle the droplets through the pattern, by turning the whole pattern on and off, so the first droplet is lost and the second droplet takes its place and so on. This allows large scale storage and controlled movement of many droplets simultaneously which may be useful for offline analysis of many droplets, droplet re-ordering or droplet "memory" applications.

Thermocapillary valve for droplet production and sorting

Charles N. Baroud,[1,*] Jean-Pierre Delville,[2,†] François Gallaire,[3] and Régis Wunenburger[2]
[1]*LadHyX and Department of Mechanics, Ecole Polytechnique, F-91128 Palaiseau cedex, France*
[2]*CPMOH, UMR CNRS 5798, Université Bordeaux 1, 351 Cours de la Libération, F-33405 Talence cedex, France*
[3]*Laboratoire J.A. Dieudonné, Université de Nice Sophia-Antipolis, 06108 Nice cedex, France*
(Received 27 July 2006; published 5 April 2007)

Droplets are natural candidates for use as microfluidic reactors, if active control of their formation and transport can be achieved. We show here that localized heating from a laser can block the motion of a water-oil interface, acting as a microfluidic valve for two-phase flows. A theoretical model is developed to explain the forces acting on a drop due to thermocapillary flow, predicting a scaling law that favors miniaturization. Finally, we show how the laser forcing can be applied to sorting drops, thus demonstrating how it may be integrated in complex droplet microfluidic systems.

DOI: 10.1103/PhysRevE.75.046302 PACS number(s): 47.61.−k, 47.55.dm

Microfluidic droplets have been proposed as microreactors with the aim to provide high performance tools for biochemistry. Individual drops may be viewed as containing one digital bit of information and the manipulation of a large number of slightly differing drops would allow the testing of a large library of genes rapidly and with a small total quantity of material [1]. In microchannels, drops are produced and transported using a carrier fluid [2] and typical channel sizes allow the manipulation of volumes in the picoliter range. Surfactant in the carrier fluid prevents cross-contamination of the drops through wall contact or fusion [3,4]. However, while the geometry of the microchannel may be used to determine the evolution of drops and their contents [3–5], the implementation of real lab-on-a-chip devices hinges on the active control of drop formation and its evolution, which remains elusive.

In this paper, we remedy the situation by demonstrating experimentally how a focused laser can provide precise control over droplets through the generation of a thermocapillary flow. In doing so, we develop the first theoretical model of a droplet subjected to localized heating, yielding a general understanding of the forces acting on the drop and a scaling law which favors miniaturization. A carrier fluid is still used for the formation and transport of drops but the effects of geometry are augmented with a local thermal gradient produced by the laser beam, focused through a microscope objective inside the microchannel.

Indeed, moving drops with heat has been a preoccupation of fluid mechanicians since the initial work of Young *et al.* [6]. Although originally motivated by microgravity conditions where surface effects are dominant [6,7], microfluidics has opened up a new area where bulk phenomena are negligible compared to surface effects. Recently, thermal manipulation of drops or thin films resting on a solid substrate has received the attention of the microfluidics community either through the embedding of electrodes in the solid [8,9] or through optical techniques [10–12]. However, the physical mechanisms in the transmission of forces when the liquid touches a solid wall are fundamentally different from the case of drops suspended in a carrier fluid, away from the boundaries [13]. The latter case has received little attention despite the advantages that microchannels offer over open geometries.

Our experimental setup consists of a microchannel fabricated using soft lithography techniques [14]. Water and oil (hexadecane +2% w/w Span 80, a surfactant) are pumped into the channel at constant flow rates, Q_{water} and Q_{oil}, using glass syringes and syringe pumps. Channel widths are in the range 100–500 μm and the height h is in the range 25–50 μm. Local heating is produced by a continuous argon-ion laser (wavelength in vacuum $\lambda_{Ar^+}=514$ nm), in the TEM_{00} mode, focused inside the channel through a $\times 5$ or $\times 10$ microscope objective to a beam waist $\omega_0=5.2$ or 2.6 μm, respectively. The optical approach can be reconfigured in real time and it allows the manipulation inside small microchannels with no special microfabrication. The absorption of the laser radiation by the aqueous phase is induced by adding 0.1% w/w of fluorescein in the water.

A surprising effect is observed when the water-oil interface reaches the laser spot: In the cross-shaped microchannel of Fig. 1, we produce water drops in oil through the hydrodynamic focusing technique in which two oil flows pinch off water droplets at the intersection of the channels. In the absence of the laser, drops of water are produced in a steady fashion and are transported along with the oil down the drain channel, as shown in Figs. 1(a)–1(c). When the laser is illuminated, however, the oil-water interface is blocked in place as soon as it crosses the beam. While the typical drop pinching time is $\tau_d \sim 100$ ms in the absence of the laser, we find that we can block the interface for a time τ_b, which may be of several seconds, as shown in Figs. 1(d)–1(f) (see Ref. [15] for video sequences). During the time τ_b, the drop shedding is completely inhibited and the volume in the water tip increases until the viscous stresses finally break it off. The drop thus produced is larger, since it has been "inflated" by the water flow.

In the microchannel shown in Fig. 2, we measured the variation of the blocking time τ_b with respect to laser power and forcing position. We observe that τ_b increases approximately linearly with the power, above an initial threshold,

*Electronic address: baroud@ladhyx.polytechnique.fr
†Electronic address: jp.delville@cpmoh.u-bordeaux1.fr

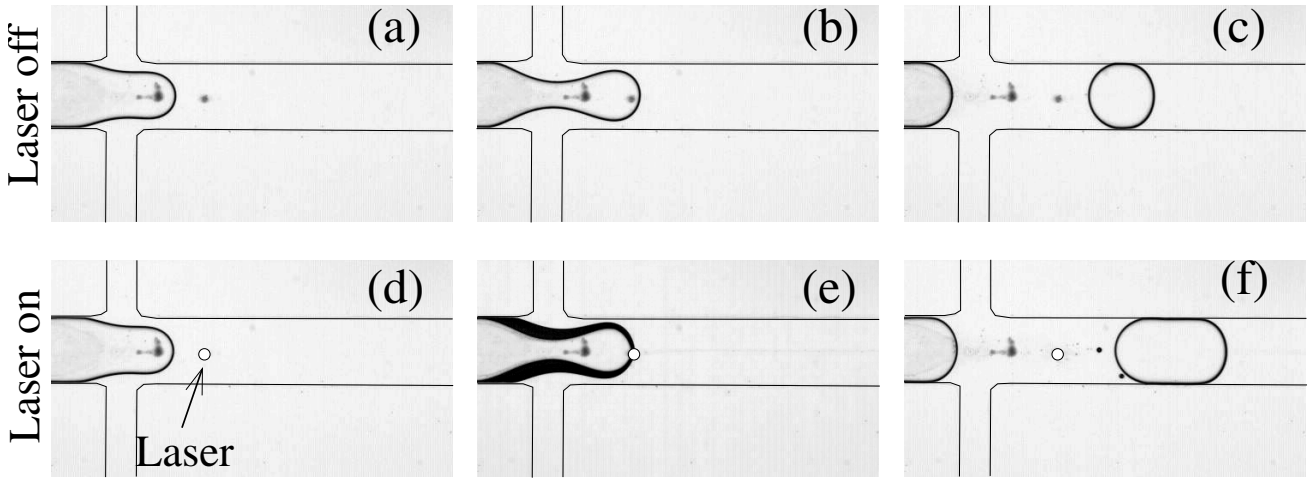

FIG. 1. Microfluidic valve: In a cross-shaped microchannel, the oil flows from the lateral channels and the water enters through the central channel. (a)–(c) In the absence of laser forcing, drops are shed with a typical break-off time [(b) and (c)] of 0.1 s. (d)–(f) When the laser is applied, the interface is blocked for several seconds, producing a larger drop. In image (e), the evolution of the neck shape is shown through a superposition of 100 images (2 s). Exit channel width is 200 μm. Operating conditions are: $Q_{\mathrm{water}}=0.08$ μL/min, $Q_{\mathrm{oil}}=0.90$ μL/min, beam power $P=80$ mW, and beam waist $\omega_0=5.2$ μm.

showing a weak position dependence of the laser spot. Furthermore, the inset of Fig. 2 shows that the droplet length L varies linearly with τ_b. As expected from mass conservation at constant water flow rate, $L=L_0+\tau_b Q_{\mathrm{water}}/S$, L_0 being the droplet length without laser and $S\simeq(125\times30)$ μm^2 the channel cross section. The best linear fit to the data gives an effective water flow rate $Q_{\mathrm{water}}=0.028$ μL/min, close to the nominal value 0.03 μL/min, showing that the water flow rate remains controlled even in presence of the laser forcing.

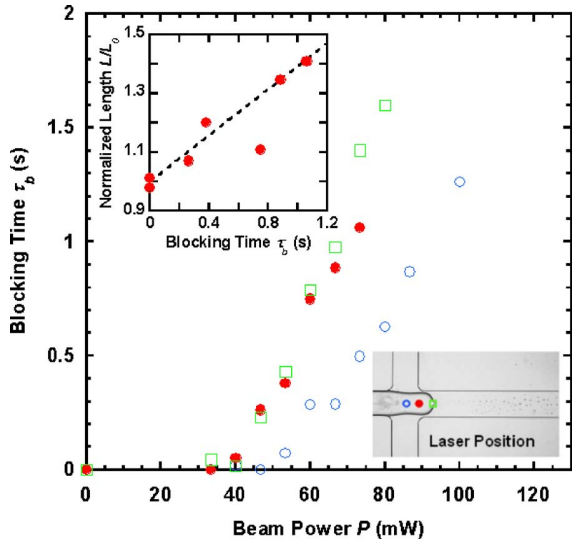

FIG. 2. (Color online) Dependence of the blocking time τ_b on laser power and position (indicated in the picture) for $Q_{\mathrm{water}}=0.03$ μL/min and $Q_{\mathrm{oil}}=0.1$ μL/min, $\omega_0=2.6$ μm. Inset: Rescaled droplet length L/L_0 vs the blocking time (laser position •), where L_0 is the droplet length without the laser. The dashed line is a linear fit, ignoring the outlier at $\tau_b=0.75$ s.

Thus, the optical forcing provides a tunable valve, which provides control over droplet timing and size. Similar blocking is observed in a T geometry or if the flows are driven at constant pressure. However, the blocking is only obtained when the light is absorbed, here through the use of a dye.

We visualize the convection rolls produced by the heating by placing tracer particles in both fluids, as shown in Fig. 3(a), for a drop that is blocked in a straight channel. For pure liquids, the direction of Marangoni flow along the interface is directed from the hot (low surface tension) to the cold (high surface tension) regions. However, the flows in our experiments point towards the laser along the interface, indicating an increase of surface tension with temperature. This is consistent with previous studies that have shown a linear increase of surface tension with temperature in the presence of surfactants [16–18].

One important constraint for practical applications is the amplitude of the temperature rise. Since the materials used in this study have similar thermal properties (thermal diffusivity $D_{th}\sim10^{-7}$ m^2 s^{-1}, thermal conductivity $\Lambda_{th}\sim0.5$ W m^{-1} K^{-1}), we estimate the maximum temperature in the flow by modeling the heating produced by a laser absorbed in a single fluid phase [19], assuming thermal diffusion as the only energy transport mechanism. Considering the measured optical absorption of our water/dye solution $\alpha_{th}=117.9$ m^{-1}, and assuming that the temperature 100 μm away is fixed by the flowing oil at room temperature, we find $\Delta T\simeq12$ K for the temperature rise at the laser focus for a beam power $P=100$ mW. The temperature gradient is steep near the focus, with the temperature dropping to 5 K at 20 μm from the beam spot. However, note that given the typical flow velocity ($U\sim1$ mm/s) and the characteristic length scale over which thermal diffusion occurs ($L=100$ μm), the thermal Péclet number $\mathrm{Pe}=UL/D_{th}$ is comparable to unity. Thus, our calculation overestimates the actual overheating.

The force generated by the convective flow on a droplet is investigated through the depth-averaged Stokes equations, since our channels have a large width/height aspect ratio [20]. The detailed modeling will be discussed in a subsequent publication; here we limit ourselves to the main features: a circular drop of radius R is considered in an infinite domain and the flow due to the Marangoni stresses is evaluated. Assuming a parabolic profile in the small dimension (h) and introducing a stream function for the mean velocities in the plane of the channel, the depth-averaged equations, valid in each fluid, are

$$\left(\frac{1}{r}\frac{\partial}{\partial r}r\frac{\partial}{\partial r}+\frac{1}{r^2}\frac{\partial^2}{\partial\theta^2}\right)\left(\frac{1}{r}\frac{\partial}{\partial r}r\frac{\partial}{\partial r}+\frac{1}{r^2}\frac{\partial^2}{\partial\theta^2}-\frac{12}{h^2}\right)\psi=0, \quad (1)$$

where the depth-averaged velocities may be retrieved from $u_\theta=-\partial\psi/\partial r$ and $u_r=1/r(\partial\psi/\partial\theta)$. The kinematic boundary conditions at the drop interface ($r=R$) are zero normal velocity and the continuity of the tangential velocity. The normal dynamic boundary condition is not imposed since the drop is assumed to remain circular, which is consistent with our experimental observations, Fig. 3(a). Finally, the tangential dynamic boundary condition, which accounts for the optically induced Marangoni stress, is

$$\mu_1 r\frac{\partial}{\partial r}\left(\frac{u_\theta^1}{r}\right)-\mu_2 r\frac{\partial}{\partial r}\left(\frac{u_\theta^2}{r}\right)=-\frac{\gamma'}{r}\frac{dT}{d\theta}, \quad (2)$$

where $\mu_{1,2}$ are the dynamic viscosities and $u_\theta^{1,2}$ are the velocities in the drop and the carrier fluid, respectively. $\gamma'=\partial\gamma/\partial T$ is the surface tension to temperature gradient, which is positive in our case.

For simplicity, we approximate the steady-state temperature distribution using a Gaussian form $T(x,y)=\Delta T\exp\{-[(x-R)^2+y^2]/w^2\}$, where ΔT is the maximum temperature difference between the hot spot and the far field and w corresponds to the size of the diffused hot spot, which is significantly larger than ω_0 [19]. The equations are nondimensionalized using ΔT as temperature scale, R as length scale, $R\gamma'\Delta T$ as force scale, and $\frac{R(\mu_1+\mu_2)}{\gamma'\Delta T}$ as time scale, the remaining nondimensional groups being the aspect ratio h/R, the nondimensional hot spot size w/R, and the viscosity ratio $\bar{\mu}=\mu_2/(\mu_1+\mu_2)$.

A typical predicted flow field solving the above numerical formulation is shown in Fig. 3(b), in which the four recirculation regions are clearly visible. The velocity gradients display a separation of scales in the normal and tangential directions, as observed from the distance between the streamlines in the two directions. Indeed, it may be verified that the velocities vary over a typical length scale h/R in the normal direction, while the tangential length scale is given by w/R.

Along with this flow field, we compute the pressure field, as well as the normal $\left(\bar{\sigma}_{\bar{r}\bar{r}}=2\bar{\mu}\frac{\partial\bar{u}_{\bar{r}}}{\partial\bar{r}}\right)$ and tangential $\left[\bar{\sigma}_{\bar{r}\theta}=\bar{\mu}\left(\frac{1}{\bar{r}}\frac{\partial\bar{u}_{\bar{r}}}{\partial\theta}+\frac{\partial\bar{u}_\theta}{\partial\bar{r}}-\frac{\bar{u}_\theta}{\bar{r}}\right)\right]$viscous shear stresses in the external flow. Their projections on the x axis, shown in the inset of Fig. 3(c), are then summed and integrated along θ to yield the total dimensionless force ($\bar{F}$) on the drop. Note that the global x component of the force is negative and therefore opposes the transport of the drop by the external flow. The y component vanishes by symmetry and the integral of the wall friction may be shown to be zero since the drop is stationary. Numerically computed values of $\bar{F}R/h$ are shown by the isolated points in Fig. 3(c) as a function of w/R, for different values of the aspect ratio h/R. The points all collapse on a single master curve, displaying a nondimensional scaling law $\bar{F}\propto wh/R^2$, for small w/R.

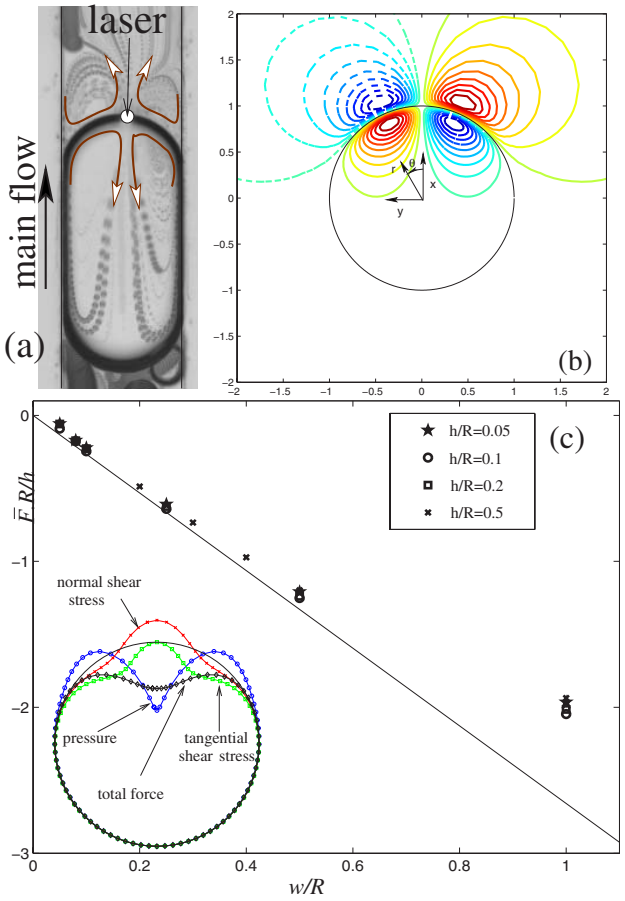

FIG. 3. (Color online) (a) Overlay of 100 images from a video sequence showing the motion of seeding particles near the hot spot. Note that the motion along the interface is directed towards the hot spot. (b) Stream function contours obtained from the depth-averaged model described in the text. Dashed and continuous contours indicate counterclockwise and clockwise flows, respectively. (c) Rescaled nondimensional force $\bar{F}R/h$ plotted as a function of w/R for various aspect ratios h/R for $\bar{\mu}=3/4$. The straight line corresponds to the dimensional scaling derived in the text. The inset shows the x component of the distribution along the azimuthal direction of the pressure, normal and tangential shear stresses, where the solid circle is the reference zero. Their sum yields the total force. Channel width in part (a) is 140 μm. $h/R=0.2$, $w/R=0.5$ for parts (b) and (c) inset.

The dimensional form of the force can be obtained, for small h/R and w/R, by considering the three contributions separately and noting that the velocity scale in this problem is imposed by the Marangoni stress. Using the separation of scales along the azimuthal and radial directions, Eq. (2) becomes $(\mu_1+\mu_2)\frac{U}{h}\sim\frac{\Delta T\gamma'}{R}\frac{R}{w}$, where the "$\sim$" is understood as

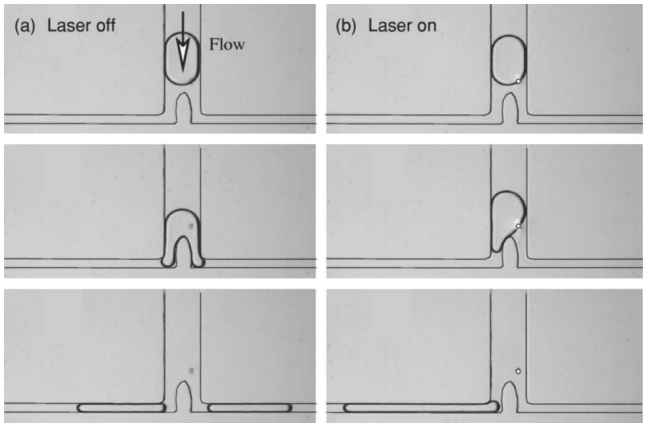

FIG. 4. Sorting drops: (a) Without laser forcing, a drop at a bifurcation divides into approximately equal daughter droplets. (b) When the laser forcing is applied, the drop advance in the right-hand channel is blocked so the whole drop is diverted into the left channel. Main channel width is 200 μm and the operating conditions are $Q_{\mathrm{water}}=0.02$ μL/min, $Q_{\mathrm{oil}}=0.2$ μL/min, and $\omega_0=5.2$ μm.

an order-of-magnitude scaling. This yields the characteristic tangential velocity scale

$$U \sim \frac{\Delta T \gamma'}{\mu_1 + \mu_2} \frac{h}{w}. \tag{3}$$

The force due to the tangential viscous shear is then obtained by multiplying $\sigma_{r\theta} \sim \mu_2 U/h$ by $\sin\theta \simeq w/R$ and integrating on the portion wh of the interface,

$$F_t \sim \mu_2 \frac{U}{h} \frac{w}{R} wh = \frac{\mu_2}{\mu_1 + \mu_2} \Delta T \gamma' \frac{hw}{R}. \tag{4}$$

The force due to the normal viscous shear can be shown to scale like $F_n \sim \frac{h}{R} F_t$ and is therefore negligible. The pressure force, on the other hand, derives from a balance between the pressure gradient and the radial second derivative of velocity. In the present circular geometry, similar scaling arguments yield a law for the contribution of the pressure force F_p, which follows the same scaling as F_t, resulting in the same scaling law for the total force F. A rigorous derivation (to be published elsewhere) yields the final form of the force including the prefactor

$$F = -2\sqrt{\pi} \frac{\mu_2}{\mu_1 + \mu_2} \Delta T \gamma' \frac{hw}{R}. \tag{5}$$

This expression is represented (once nondimensionalized) by the straight line on Fig. 3(c) and agrees very well with the numerically computed values.

The physical value of the force for a typical experiment is estimated by taking $\mu_1 = 10^{-3}$ N m^{-2} s (water), $\mu_2 = 3\mu_1$ (hexadecane), and extracting $\gamma' \sim 1$ mN m^{-1} K^{-1} from Ref. [17]. This yields a force on the order of 0.1 μN, which is of the same order as the drag force on a drop in a large aspect ratio channel [21], thus confirming that thermocapillary forcing can indeed account for the blocking. Note that the force we calculate is several orders of magnitude larger than those generated from electric fields [22] or optical tweezers [23].

This blocking force may be applied at different locations in a microchannel by displacing the laser spot. In particular, we demonstrate the sorting of drops, a fundamental operation in the implementation of lab-on-a-chip devices. Drops are formed, as above, in a cross junction and arrive at a symmetric bifurcation, carried by the continuous phase. In the absence of laser forcing, the drops arriving at the bifurcation divide into two equal parts [5] [Fig. 4(a)]. When the laser is applied, the water-oil interface is asymmetrically blocked on the right-hand side while the left-hand side continues to flow [Fig. 4(b)]. Above a critical laser power (approximately 100 mW for the present configuration), the drop is blocked long enough that it is completely diverted through the left-hand channel [15]. Drops may therefore be sorted by accordingly selecting the laser position.

In summary, we have experimentally and theoretically demonstrated the efficiency of laser-driven blocking of water-in-oil drops. The theoretical treatment brings out two length scales, h/R and w/R. While h and w can be thought of as determining the typical scales for velocity variations in the radial and azimuthal directions, R enters the force scaling as a local radius of curvature rather than the actual size of the drop. It is therefore not surprising that the blocking force should *increase* as R decreases. On the other hand, the drag force due to the external flow scales as R^2 [21], implying that the laser power necessary to counterbalance the drag quickly decreases with the drop size. This, along with the rapidity of viscous and thermal diffusion while thermal inertia is reduced, all lead to laws favorable to miniaturization. The generality of the process provides a practical new way for acting on individual droplets, at any location, while working inside the robust environment of the microchannel.

We acknowledge help from Julien Buchoux, David Dulin, and Emilie Verneuil. This work was partially funded by the CNRS *PIR* "Microfluidique et Microsystèmes Fluidiques," the Conseil Régional d'Aquitaine, and the *convention X-DGA*.

[1] O. Miller, K. Bernath, J. Agresti, G. Amitai, B. Kelly, E. Mastrobattista, V. Taly, S. Magdassi, D. Tawfik, and A. Griffiths, Nat. Methods **3**, 561 (2006).
[2] T. Thorsen, R. W. Roberts, F. H. Arnold, and S. R. Quake, Phys. Rev. Lett. **86**, 4163 (2001).
[3] H. Song, J. Tice, and R. Ismagilov, Angew. Chem., Int. Ed. **42**, 768 (2003).
[4] M. Joanicot and A. Ajdari, Science **309**, 887 (2005).

[5] D. R. Link, S. L. Anna, D. A. Weitz, and H. A. Stone, Phys. Rev. Lett. **92**, 054503 (2004).
[6] N. Young, J. Goldstein, and M. Block, J. Fluid Mech. **6**, 350 (1959).
[7] R. Balasubramaniam and R. Subramanian, Phys. Fluids **12**, 733 (2000).
[8] T. Sammarco and M. Burns, AIChE J. **45**, 350 (1999).
[9] A. Darhuber, J. Valentino, J. Davis, S. Troian, and S. Wagner, Appl. Phys. Lett. **82**, 657 (2003).
[10] N. Garnier, R. O. Grigoriev, and M. F. Schatz, Phys. Rev. Lett. **91**, 054501 (2003).
[11] J. Sur, T. P. Witelski, and R. P. Behringer, Phys. Rev. Lett. **93**, 247803 (2004).
[12] K. Kotz, K. Noble, and G. Faris, Appl. Phys. Lett. **85**, 2658 (2004).
[13] E. Lajeunesse and G. Homsy, Phys. Fluids **15**, 308 (2003).
[14] D. Duffy, J. McDonald, O. Schueller, and G. Whitesides, Anal. Chem. **70**, 4974 (1998).
[15] See EPAPS Document No. E-PLEEE8-75-059703 for movie sequences from the experiments. For more information on EPAPS, see http://www.aip.org/pubservs/epaps.html.
[16] B. Berge, O. Konovalov, J. Lajzerowicz, A. Renault, J. P. Rieu, M. Vallade, J. Als-Nielsen, G. Grübel, and J. F. Legrand, Phys. Rev. Lett. **73**, 1652 (1994).
[17] E. Sloutskin, C. Bain, B. Ocko, and M. Deutsch, Faraday Discuss. **129**, 1 (2005).
[18] A reduction of the surfactant concentration reduced the efficiency of the blocking; a detailed exploration of surfactant effects will be addressed in a future study.
[19] J. Gordon, R. C. C. Leite, R. S. Moore, S. P. S. Porto, and J. R. Whinnery, J. Appl. Phys. **36**, 3 (1965).
[20] W. Boos and A. Thess, J. Fluid Mech. **352**, 305 (1997).
[21] A. Nadim, A. Borhan, and H. Haj-Hariri, J. Colloid Interface Sci. **181**, 159 (1996).
[22] K. Ahn, C. Kerbage, T. Hynt, R. Westervelt, D. Link, and D. Weitz, Appl. Phys. Lett. **88**, 024104 (2006).
[23] D. Grier, Nature (London) **424**, 810 (2003).

An optical toolbox for total control of droplet microfluidics†‡

Charles N. Baroud,*[a] Matthieu Robert de Saint Vincent[b] and Jean-Pierre Delville*[b]

Received 15th February 2007, Accepted 17th May 2007
First published as an Advance Article on the web 8th June 2007
DOI: 10.1039/b702472j

The use of microfluidic drops as microreactors hinges on the active control of certain fundamental operations such as droplet formation, transport, division and fusion. Recent work has demonstrated that local heating from a focused laser can apply a thermocapillary force on a liquid interface sufficient to block the advance of a droplet in a microchannel (C. N. Baroud, J.-P. Delville, F. Gallaire and R. Wunenburger, *Phys. Rev. E: Stat., Nonlinear, Soft Matter Phys.*, 2007, **75**(4), 046302). Here, we demonstrate the generality of this optical approach by implementing the operations mentioned above, without the need for any special microfabrication or moving parts. We concentrate on the applications to droplet manipulation by implementing a wide range of building blocks, such as a droplet valve, sorter, fuser, or divider. We also show how the building blocks may be combined by implementing a valve and fuser using a single laser spot. The underlying fundamentals, namely regarding the fluid mechanical, physico-chemical and thermal aspects, will be discussed in future publications.

1. Introduction

Droplets are natural candidates for use as microreactors, since they transport fluid with no dispersion and may be formed and manipulated using microfluidic techniques.[1–4] Indeed, a drop may be formed with a known composition and volume[5–7] and transported by an inert fluid without loss of the solute species and without cross-contamination.[8] Furthermore, fusion of two drops containing two reactive species leads to the onset, on demand, of a reaction[9] whose product may be sampled by breaking the drop at a bifurcation.[10] Finally, logical operations can be performed on drops by sorting them based on a test of their contents, as they reach a bifurcation in the microchannel.[11,12] The above operations form the basis of a droplet-based lab-on-a-chip which can be designed through an intelligent combination of a few building blocks. Conversely, a lack of active control over individual drops would severely limit the usefulness of droplet microreactors.

However, acting on individual drops in microchannels remains difficult. Recent publications have demonstrated, *via* electrode micropatterning on the chip, the use of electric fields to apply forces on droplets[11] or to merge them.[9,13] However, the forces generated through dielectrophoresis were measured to be in the range of a few nN and scale with the cube of the drop radius, since the electrophoretic force is a body force.[11] This is a highly unfavourable scaling which implies that the force generated will quickly decrease as the drop size decreases. In contrast, others have demonstrated the use of surface forces to manipulate drops on open substrates by modulating their surface properties chemically, electrically or thermally (see *e.g.* ref. 14 and references therein). These surface forces become dominant over body forces at small scales, as the ratio of surface to volume becomes large. It is natural therefore to look for a surface mechanism for the manipulation of drops inside the robust environment of a microchannel.

Along these lines, we have recently demonstrated that forces near the μN range could be produced on a droplet by optically heating a water–oil–surfactant interface with a laser wave.[12] This force is generated through the thermocapillary (or Marangoni) effect, by which the surface tension varies due to a temperature variation; localized heating from a focused laser therefore leads to a spatial imbalance of surface tension which, in turn, induces a flow inside and around the drop. By computing the shear and pressure fields associated with the external flow, one may find that a net force is produced on the drop.[15] A theoretical analysis for localized heating shows a scaling that is highly favourable to miniaturization, since the total force is predicted to increase as the drop radius decreases.[12]

In our experiments, we observe that the surface tension rises as the temperature is increased. This anomalous behaviour, likely due to the presence of surfactant,[16,17] yields a force that pushes the drop away from the hot spot and acts to block it in the presence of an external carrier flow. Since the time required for the Marangoni flow to appear is short enough, a droplet can be blocked during its formation, corresponding to a contactless optical microfluidic valve, which can also be used to control the size of the drops thus produced. Finally, drops can also be sorted by simply illuminating one exit of a bifurcating microchannel.[12]

Below, we show the generality of this optical approach and how it may be used to provide a complete set of tools for the manipulation of drops in microchannels. These tools allow the control of drop formation and sorting, as previously demonstrated, and also drop fusion and division. We also

[a]*LadHyX and Department of Mechanics, Ecole Polytechnique, 91128, Palaiseau cedex, France. E-mail: baroud@ladhyx.polytechnique.fr*
[b]*Université Bordeaux 1, CPMOH (UMR CNRS 5798), 351 Cours de la Libération, F-33405, Talence cedex, France. E-mail: jp.delville@cpmoh.u-bordeaux1.fr*

† Electronic supplementary information (ESI) available: Supporting videos 1 (droplet fusion), 2 (valving and fusion) and 3 (division and sorting). See DOI: 10.1039/b702472j

‡ The HTML version of this article has been enhanced with colour images.

demonstrate how the operations may be combined, while still using a single laser spot, through a combination of channel geometry and laser actuation. This opens the way for total control of droplet microreactors without the need for specific microfabrication.

2. Experimental

Our experimental setup consists of a microchannel fabricated in Polydimethylsiloxane (PDMS), using standard soft lithography techniques. Water and oil (hexadecane + 2% w/w Span 80, a surfactant) are pumped into the channel at constant flowrates, Q_{water} and Q_{oil}, using glass syringes and syringe pumps; the fluids may also be forced at constant pressure. Channel widths are in the range 100–500 μm and the height is in the range 25–50 μm. Local heating is produced by focusing a continuous Argon-Ion laser (wavelength in vacuum λ_{Ar^+} = 514 nm), in the TEM_{00} mode through a microscope objective. The absorption of the laser is mediated by the addition of a dye, such as fluorescein (0.1% w/w), in the water phase. The resulting optical absorption of the aqueous phase is about 1.18 cm^{-1}.

Different microscope objectives were used to focus the laser inside the microchannel, ranging from a ×2.5 to a ×10 magnification, which correspond to beam waists (ω_0) in the range of 10.3 to 2.6 μm. The Fresnel length, defined as $L_F = n\pi\omega_0^2/\lambda$ where n is the refractive index and λ the wavelength in vacuum, may be estimated at $L_F \simeq$ 50 μm by using n = 1.33 and ω_0 = 2.5 μm. Consequently, we can assume that the focused beam is almost cylindrical over a distance of 100 μm (50 μm on each side of the beam waist), which is twice the largest thickness of our channels. This implies that the use of low magnification objectives makes the behavior rather insensitive to the exact focus plane, as opposed for example to laser tweezers.

3. Formation and fusion

3.1 Microfluidic valve

The valve mechanism for two-phase flows was recently achieved[12] by illuminating the water–oil interface during the drop formation at a cross-junction, with a laser power (P) on the order of a few tens of mW, focused through a microscope objective. The local heating thus produced was shown to completely block the advance of the interface for a time τ_b which increased with increasing laser power. This blocking also provided control over the size of the drops thus produced, since they were inflated by the syringe pumps operating at a constant flowrate.

This valve is generic and works equally well in a T geometry where the oil and water arrive either from opposite channels (Fig. 1a) or from perpendicular channels (*e.g.* Fig. 4). Similar blocking is also observed if the flows are driven at constant pressure or by mixing pressure and flowrate sources. For instance, Fig. 1a shows the laser blocking the drop shedding at different locations with the oil flow (bottom channel) driven at constant flowrate and the water flow (top channel) driven at constant pressure. In the absence of the laser, drops are formed in a periodic fashion. In the presence of the laser, the water interface is blocked at the laser focus, as shown in the Figure, while the oil continues to flow. The variation of the blocking time τ_b with the laser power and position is illustrated in Fig. 1b. While τ_b increases approximately linearly with the power above an initial threshold, it also displays a dependence on the laser position in the microchannel. The values of the onset and the slope of τ_b depend on the details of the flow, but the same general behaviour is observed independently of the microchannel geometry, flowrates, or pumping method.

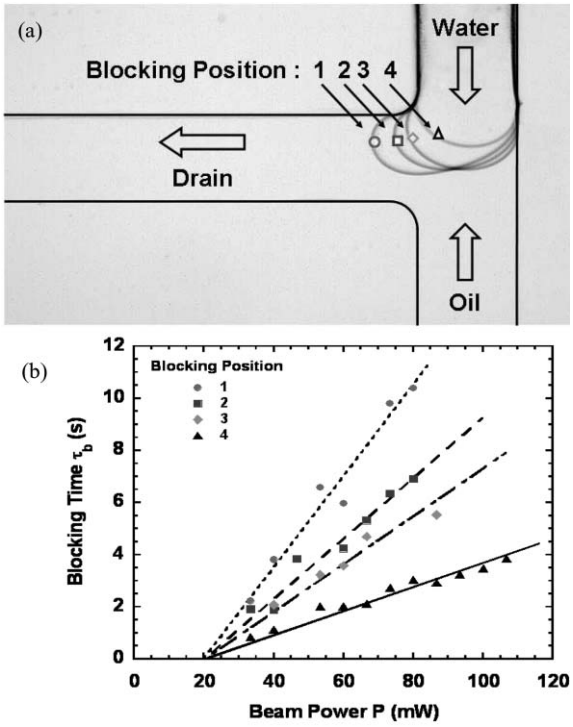

Fig. 1 Microfluidic valve in a T geometry. (a) Superposition of microscopic images of the laser blocking the interface at different locations in the microchannel. All channels are 100 μm wide. (b) Dependence of the blocking time τ_b on laser power and position (indicated in (a)) for Q_{oil} = 0.05 μL min^{-1} and P_{water} = 2.3 × 10^3 Pa, ω_0 = 2.6 μm. The lines are linear fits to guide the eye.

The dependence of the blocking time on beam waist was explored in a cross-geometry by keeping constant the fluid flow rates (Q_{water} = 0.12 μL min^{-1} and Q_{oil} = 0.3 μL min^{-1}) and the laser position. The geometry that was used corresponds to a cross-junction with oil channel widths 100 μm and water channel width 200 μm. The laser was placed at a distance 200 μm downstream of the oil channel centerline and the blocking time (τ_b) was measured as a function of beam waist, which was varied by changing the microscope objective. The measurements of τ_b were normalized by the natural emission frequency of the drops (F_0) and were fitted by straight lines to determine the threshold power (P_{th}) and slope ($S = F_0 d\tau_b/dP$). While P_{th} was found to remain constant at $P_{th} \simeq$ 40 mW, S increased with decreasing beam waist as $S = 4.5 \times 10^{-3}$, 8.2×10^{-3} and 13.4×10^{-3} W^{-1} for ω_0 = 10.3, 5.2 and 2.6 μm, respectively.

3.2 Fusion of drops

Fusing droplets is the step that allows chemical reactions by bringing together the reactants originally contained in separate drops. However, simply putting drops in contact is typically insufficient to induce merging, since a lubrication film between

them prevents the water contained in the two drops from actually touching. Indeed, the presence of surfactant molecules on an oil–water interface is known to stabilize drops against merging.[18,19] Localized heating close to the nearly touching interfaces may be used to evacuate the surfactant molecules and with them the oil film, as shown in Fig. 2. Here, the downstream drop is held stationary by the laser heating until a second one collides with it (Fig. 2a). At this point, the two drops advance until the laser gets near the adjacent interfaces, and we observe that the oil film is evacuated and the two drops rapidly merge.

Similar merging may be obtained in a long train of drops, as shown in Fig. 3. Here, a train of water drops is carried by an oil flow in a wide channel. Again, these drops are stable against merging due to the presence of the surfactant and spontaneous merging is never observed in our experiments (Figs. 3a,b). However, weak heating at the interface from the laser spot, although insufficient to block the drop advance, rapidly induces merging when the laser spot approaches the adjacent interfaces (Fig. 3c). Merging only occurs in the heated region (Fig. 3d) while the other interfaces remain unaffected. This shows that one may induce the merger of specific drops even in a complex flow which contains many drops and interfaces. A succession of such events is shown in the supporting video 1 in the ESI†.

3.3 Combined operations: drop fusion at formation

The synchronization of drops in order to combine their contents is a major challenge for lab-on-a-chip operations. Alternating formation of drops from two sources was recently demonstrated by finely tuning the different water and oil flowrates.[9] This approach, however, is only useful in the simplest cases where only two droplet streams are involved and the downstream conditions are constant. A more robust approach would be for a downstream drop to delay its formation and wait for the upstream drop to catch up with it, at which point the two merge together. This corresponds, in our terms, to a combination of a valve and a fusion mechanism; once the two building blocks exist, combining them becomes a simple matter as shown in Fig. 4.

Here, drops are formed at successive T-junctions and flow down the same exit channel. In the absence of the laser forcing

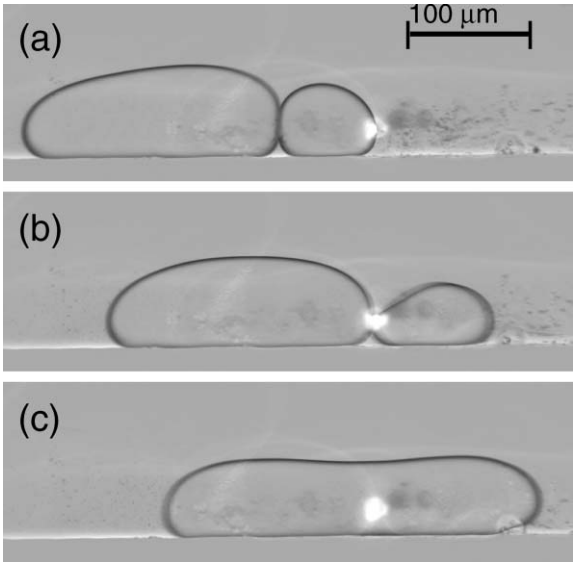

Fig. 2 Time sequence showing droplet fusion through laser heating. (a) The blocking of a first drop by the laser brings the drop that follows in contact with it. (b) The two drops move forward together, their coalescence occurring when the beam reaches the touching interfaces, giving birth to a larger drop (c). Time between images is 40 ms and operating conditions are Q_{water} = 0.2 μL min^{-1}, Q_{oil} = 0.9 μL min^{-1}, P = 67 mW and ω_0 = 2.6 μm.

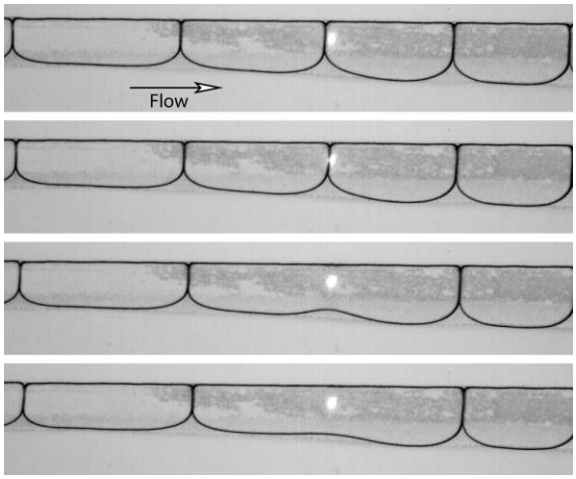

Fig. 3 Localized fusion in a train of large drops. The drops, which flow from left to right, merge as the interface crosses the laser. Time between images is 30 ms and operating conditions are Q_{water} = 0.2 μL min^{-1}, Q_{oil} = 0.3 μL min^{-1}, P = 67 mW and ω_0 = 5.2 μm.

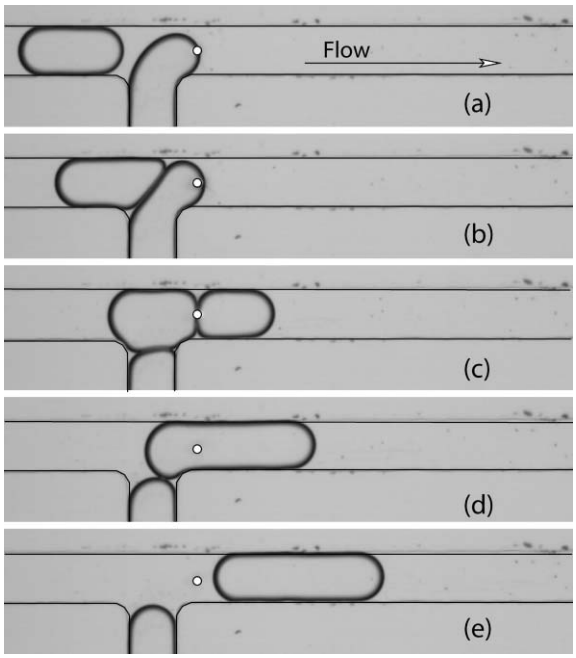

Fig. 4 A forming drop is blocked by the laser-valve (a) until a second drop, formed upstream, collides with it (b). The collision liberates the front drop (c) and the two merge when their interface approach the laser (d). Operating conditions are Q_{water} = 0.1 μL min^{-1}, Q_{oil} = 1 μL min^{-1}, P = 67 mW and ω_0 = 5.2 μm. The laser position is represented by the white circle.

(not shown), the drop formation is not synchronized and neither do they merge if they do come into contact. The situation is different in the presence of the laser, which holds the downstream interface in place (Fig. 4a) until the upstream drop is formed and collides with it (Fig. 4b). Since the upstream drop completely blocks the channel, the hydrodynamic drag on the two-drop system becomes too large and the two drops start to flow again (Fig. 4c), merging together when their touching interfaces approach the laser (Fig. 4d). (See supporting video 2 in the ESI†.)

The valve and fusion actions here are performed with only one laser spot, showing how the different building blocks may be superposed by combining the laser action with a geometric constraint. This is done with no overhead in power or complexity with respect to a single operation, demonstrating how the technique may be scaled to a complex lab-on-a-chip involving many operations.

4. Drop transport: division and sorting

The remaining steps after the formation and merging of drops are their transport and division, which involve control over the route they follow at bifurcating channels. Two operations are demonstrated below: sampling a drop, *i.e.* dividing it into unequal daughter droplets of calibrated size, and sorting. A sampler which uses a combination of channel geometry and laser forcing is shown in Fig. 5. We see in it drops that are longer than the channel width and that arrive at a symmetric bifurcation, carried by the oil phase. At the bifurcation, the drops divide into two parts whose lengths in the daughter channels we label L_1 and L_2. We are interested in the ratio $\lambda \equiv \langle (L_1 - L_2)/(L_1 + L_2) \rangle$ which yields $\lambda = 0$ for symmetric drops and $\lambda = 1$ for complete sorting. The brackets $\langle\ \rangle$ here denote an average over several drops.

In the absence of the laser (Fig. 5a), we measure $\lambda = 0.022 \pm 0.01$ for our microchannel, corresponding to a slight asymmetry in the microfabrication. When the laser is applied in front of one of the two exits, the water–oil interface is asymmetrically blocked at the laser position for a time τ_b, while the other side continues to flow (Fig. 5b). After τ_b, both sides of the drop continue forward into their respective channels, but the retardation of the right hand droplet tip produces an asymmetry in the breaking, measured by an increase in λ. Since the blocking time τ_b increases with the laser power, so does the asymmetry in the division, as shown in Fig. 5c. (See supporting video 3 in the ESI†.)

Above a critical power (approximately 100 mW for the present configuration), the drop does not divide but is always diverted into the opposite branch. This sorting operation may be understood by considering the length of the droplet upstream of the laser. If the upstream length decreases below a critical size of approximately the channel width (corrected by the displacement of the laser with respect to the channel center), the drop takes a circular shape and loses contact with the right hand wall. In this case, a tunnel opens for the oil to flow between the drop and the wall and the drop does not divide anymore but is pushed into the left hand channel.

Unequal droplet splitting may be achieved through passive techniques, for example by varying the downstream resistance

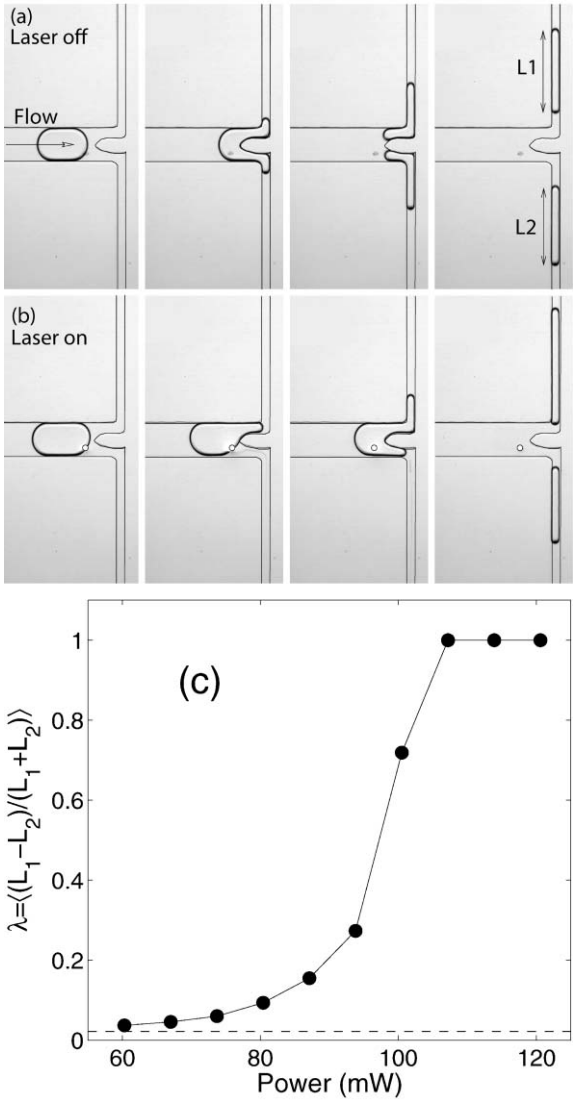

Fig. 5 A droplet sampler: (a) without laser forcing, a drop at a bifurcation divides into approximately equal daughter droplets. (b) By controlling the laser power (marked with a white circle, here P = 93 mW), we control the pinning time of one side of the interface and thus the asymmetry of the division. Main channel width is 200 μm and the time between images is 0.2 s. Operating conditions are Q_{water} = 0.02 μL min^{-1}, Q_{oil} = 0.2 μL min^{-1}, and ω_0 = 5.2 μm. (c) Daughter droplet size dependence on laser power ($\lambda = 0$ is for symmetric drops and $\lambda = 1$ is for the sorter). The dashed line corresponds to the mean value of λ in the absence of the laser.

to the flow in simple cases.[10,20] However, the optical actuation adds an active component to the control of each droplet. It thus provides an additional control parameter that can be used in conjunction with passive control, independently of the downstream conditions or of the microsystem's complexity.

5. Generality and optimization

Our approach to controlling microfluidic droplets relies on all-optical techniques which have been greatly developed in recent years in connection with microfluidic devices.[21–25] Indeed, optical trapping has become a standard tool in biophysics[26] and holographic[22] and generalized phase contrast[25] methods

now allow a single laser to be divided into many spots which can be independently manipulated. The application of beam division techniques to thermocapillary control should be relatively straight-forward and it will allow the parallel implementation of many independent building blocks in a complex network of channels. For instance, many valves, fusers, and sorters may be operated independently through the implementation of holographic division of the laser or by sweeping a single beam with a galvanometric mirror. Furthermore, a judicious choice of a laser wavelength and fluid combinations can improve the efficiency of the approach. In this regard, current experiments have reproduced the above results with an infrared laser which acts directly on the water molecules, allowing us to work without the need for an absorbing dye.

Moreover, the physical scaling laws for this forcing technique are favourable to further miniaturization, since the technique takes advantage of the dominance of surface effects in microfluidics. The force produced by the thermocapillary flow was theoretically found to scale as $1/R$, where R represents the in-plane radius of curvature of the drop at the hot spot.[12] The force is therefore expected to *increase* as the drop size decreases, as long as the local heating hypothesis may be maintained. This scaling may be used to optimize the performance of the system, for example by using channels with a variable width or by placing the laser at the position with highest drop curvature. Such optimization should allow the implementation of the devices with minimal laser power, further promoting parallelization and portability.

The response time should also scale favourably with miniaturization since it is limited by the heat and viscous diffusion processes and thermal inertia. The latter decreases as the cube of the length scale, and is therefore negligibly small in microchannels. Moreover, the viscous diffusion time ($\tau_{visc} \sim \ell^2/\nu$, where $\ell \simeq 30$ μm is a typical length scale and $\nu \simeq 10^{-6}$ m^2 s^{-1} is the kinematic viscosity of water) and the thermal diffusion time ($\tau_{th} \sim \ell^2/D$, where $D \simeq 10^{-7}$ m^2 s^{-1} is a typical thermal diffusion coefficient) are both on the order of a few ms, indicating that droplet manipulation at the kHz range may be possible.

Finally, since the method requires no moving parts or special microfabrication, the forcing is reconfigurable in real-time and may be adapted to many different microchannel geometries. Owing to its flexibility and scalability, our optical approach offers a complete toolbox for droplet based lab-on-a-chip applications.

Acknowledgements

Useful discussions are acknowledged with François Gallaire and Régis Wunenburger. This work was partially funded by the CNRS *Projet interdisciplinaire de recherche* ''Microfluidique et Microsystèmes Fluidiques'', the Conseil Régional d'Aquitaine (Université Bordeaux 1 group), and the *convention X-DGA* (Ecole Polytechnique group).

References

1 T. M. Squires and S. R. Quake, Microfluidics: Fluid physics at the nanoliter scale, *Rev. Mod. Phys.*, 2005, **77**(3), 977–1026.
2 J. Atencia and D. J. Beebe, Controlled microfluidic interfaces, *Nature*, 2005, **437**, 648–655.
3 A. Günther and K. F. Jensen, Multiphase microfluidics: from flow characteristics to chemical and material synthesis, *Lab Chip*, 2006, **6**, 1487–1503.
4 H. Song, D. L. Chen and R. F. Ismagilov, Reactions in droplets in microfluidic channels, *Angew. Chem., Int. Ed.*, 2006, **45**, 7336–7356.
5 T. Thorsen, R. W. Roberts, F. H. Arnold and S. R. Quake, Dynamic pattern formation in a vesicle-generating microfluidic device, *Phys. Rev. Lett.*, 2001, **86**(18), 4163–4166.
6 S. L. Anna, N. Bontoux and H. A. Stone, Formation of dispersions using 'flow-focusing' in microchannels, *Appl. Phys. Lett.*, 2003, **82**(3), 364–366.
7 R. Dreyfus, P. Tabeling and H. Willaime, Ordered and disordered patterns in two phase flows in microchannels, *Phys. Rev. Lett.*, 2003, **90**, 144505.
8 M. Chabert, K. D. Dorfman, P. de Cremoux, J. Roeraade and J.-L. Viovy, Automated microdroplet platform for sample manipulation and polymerase chain reaction, *Anal. Chem.*, 2006, **78**, 7722–7728.
9 K. Ahn, J. Agresti, H. Chong, M. Marquez and D. Weitz, Electrocoalescence of drops synchronized by size-dependent flow in microfluidic channels, *Appl. Phys. Lett.*, 2006, **88**, 264105.
10 D. R. Link, S. L. Anna, D. A. Weitz and H. A. Stone, Geometrically mediated breakup of drops in microfluidic devices, *Phys. Rev. Lett.*, 2004, **92**(5), 054503.
11 K. Ahn, C. Kerbage, T. Hynt, R. M. Westervelt, D. R. Link and D. A. Weitz, Dielectrophoretic manipulation of drops for high-speed microfluidic sorting devices, *Appl. Phys. Lett.*, 2006, **88**, 024104.
12 C. N. Baroud, J.-P. Delville, F. Gallaire and R. Wunenburger, Thermocapillary valve for droplet production and sorting, *Phys. Rev. E: Stat., Nonlinear, Soft Matter Phys.*, 2007, **75**(4), 046302.
13 C. Priest, S. Herminghaus and R. Seemann, Controlled electrocoalescence in microfluidics: Targeting a single lamella, *Appl. Phys. Lett.*, 2006, **89**, 134101.
14 A. A. Darhuber and S. M. Troian, Principles of microfluidic actuation by modulation of surface stresses, *Annu. Rev. Fluid Mech.*, 2005, **37**, 425–455.
15 N. O. Young, J. S. Goldstein and M. J. Block, The motion of bubbles in a vertical temperature gradient, *J. Fluid Mech.*, 1959, **6**, 350–356.
16 B. Berge, O. Konovalov, J. Lajzerowicz, A. Renault, J. P. Rieu, M. Vallade, J. Als-Nielsen, G. Grübel and J. F. Legrand, Melting of short 1-alcohol monolayers on water: Thermodynamics and X-ray scattering studies, *Phys. Rev. Lett.*, 1994, **73**(12), 1652–1655.
17 E. Sloutskin, C. D. Bain, B. M. Ocko and M. Deutsch, Surface freezing of chain molecules at the liquid–liquid and liquid–air interfaces, *Faraday Discuss.*, 2005, **129**, 1–14.
18 J. Bibette, D. C. Morse, T. A. Witten and D. A. Weitz, Stability criteria for emulsions, *Phys. Rev. Lett.*, 1992, **69**, 2439–2442.
19 Y. Amarouchene, G. Cristobal and H. Kellay, Noncoalescing drops, *Phys. Rev. Lett.*, 2001, **87**, 206104.
20 L. Ménétrier-Deremble and P. Tabeling, Droplet breakup in microfluidic junctions of arbitrary angles, *Phys. Rev. E: Stat., Nonlinear, Soft Matter Phys.*, 2006, **74**, 035303.
21 A. Terray, J. Oakey and D. W. M. Marr, Microfluidic control using colloidal devices, *Science*, 2002, **296**, 1841–1844.
22 D. G. Grier, A revolution in optical maniupulation, *Nature*, 2003, **424**, 810–816.
23 M. P. MacDonald, G. C. Spalding and K. Dholakia, Microfluidic sorting in an optical lattice, *Nature*, 2003, **426**, 421–424.
24 D. R. Burnham and D. McGloin, Holographic optical trapping of aerosol droplets, *Opt. Express*, 2006, **14**(9), 4176–4182.
25 I. R. Perch-Nielsen, P. J. Rodrigo, C. A. Alonzo and J. Glückstad, Autonomous and 3d real-time multi-beam manipulation in a microfluidic environment, *Opt. Express*, 2006, **14**(25), 12199–12205.
26 J. Guck, R. Ananthakrishnan, T. J. Moon, C. C. Cunningham and J. Käs, The optical stretcher - a novel, noninvasive tool to manipulate biological materials, *Biophys. J.*, 2001, **81**, 767–784.

Chapter 4

Recent and future work

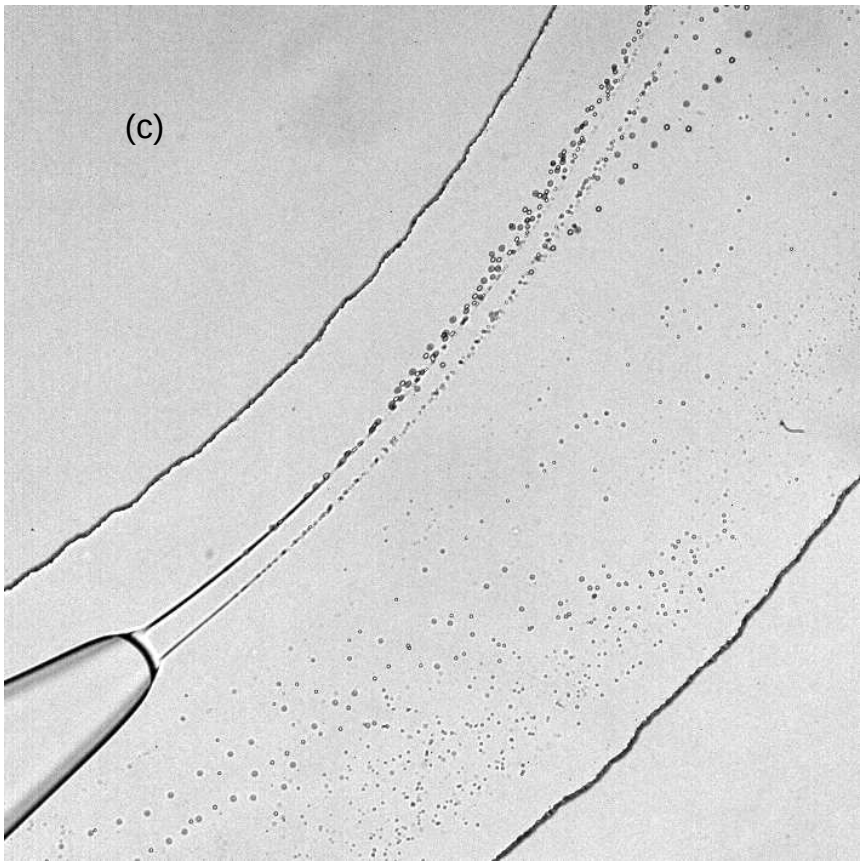

Below, some "other", newer, projects will be described. We will begin with a description of a study on tip-streaming that was undertaken with Simon Molesin, an undergraduate student at Ecole Polytechnique during his "stage d'option". We will end with the current work that is underway at our lab and whose results are not yet in publishable form.

4.1 Tip-Streaming

This work is still ongoing. It was started with the "stage" of Simon Molesin at LadHyX (in 2006-2007) and is being continued with Thomas Dubos.

The production of singular tips on drops has received significant attention, which was increased recently by some detailed work on interfaces submitted to strong shear, whether through "selective withdrawal" [35, 39] or through air entrainment [84]. These singular structures are produced on an otherwise quiescent layer of liquid, which makes their observation and measurements possible. On the other hand, the production of tips on moving droplets has a long history, since it was first observed by G.I. Taylor who described the stretching of a drop submitted to shear and streaming smaller drops as "tip streaming" in 1934 [117]. More recently, this phenomenon was studied from a phenomenological point of view by de Bruijn, who noted that tip streaming only appeared for intermediate surfactant concentrations, which suggests that surfactant must play an important role in the process [43]. Later studies on tip-streaming were mainly numerical in nature [50, 16], although the phenomenon has been reported experimentally in recent papers [7, 8, 53].

However, detailed studies remained difficult. The challenge arises, in the case of experiments, in the difficulty of making detailed quantitative measurements on the drops. Indeed, most experiments to date consist of qualitative observations of a single drop in an externally imposed flow, such as a four roll mill or a Couette flow [43, 89, 105]. In the case of numerical simulations, studies of tip streaming are complicated by the need to follow of a free surface coupled with several nonlinear equations which account for the surfactant transport, adsorption/desorption dynamics, and the relation between surface concentration and surface tension [94, 50, 16].

The experimental setup we used consisted of a circular shaped PDMS microchannel. The channel had four PDMS walls, with a cross-section width $w = 500$ μm and height $h = 35$ μm. The outer radius of the circular channel was 2 mm, allowing observations to be done using an inverted microscope ($\times 4$ to $\times 15$ magnification) and a fast camera at 1024×1024 pixel resolution, as shown in Fig. 4.1a.

Water and paraffin oil are forced through syringe pumps into the microchannel, where drops of water in oil are produced in a continuous fashion at a T-junction. Several hundred drops were studied in this fashion while varying the bulk surfactant concentration (c), the total flow rate (Q), and the drop size. The oil viscosity (μ_o) was measured to be 0.21 Pa s, yielding a Reynolds number below below 10^{-2} for all of our experimental conditions. Surfactant (Span80) was added to the oil at three concentrations: 0.05, 0.15, and 0.5% wt/wt. Finally, the surface tension for the three concentrations was measured using the pendant drop technique, giving $\gamma = 16 \cdot 10^{-3}$, $9 \cdot 10^{-3}$, and $5 \cdot 10^{-3}$ N/m

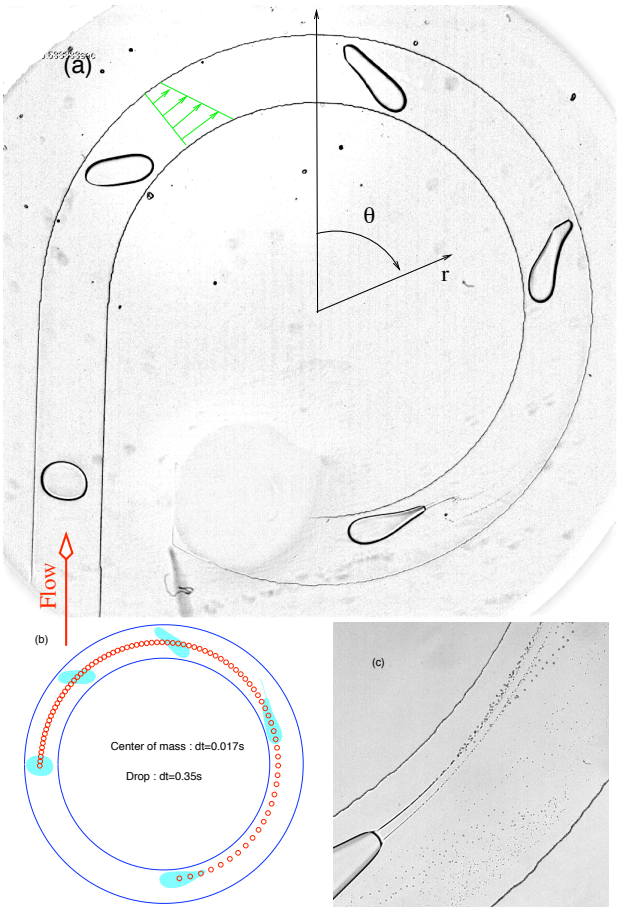

Figure 4.1: (a) Experimental snapshot of the circular channel with several drops flowing clockwise. The channel width is 500 μm. (b) Reconstituted history of a single drop showing the shape and centroid position at regular time intervals. (c) Detail photograph showing two tips streaming from the rear of a drop. Experimental conditions: $Q = 5.2$ μL/min and $c = 0.05\%$.

respectively for the three concentrations. The surface tension in the absence of surfactant was measured to be $25 \cdot 10^{-3}$ N/m.

Owing to the large width/height aspect ratio, one may use the potential flow theory to write the velocity profile of the base flow as $U = \phi/r$, where ϕ is a constant that depends on the total flow rate and r is the radial position measured from the center of the circle. Note that this approximation applies to the velocity averaged across the depth of the channel and is valid a distance of order h from the inner and outer walls. The velocity profile in the direction normal to the plane of the channel is expected to be parabolic. Furthermore, since the channel width ($w = 500$ μm) is small compared with the mean radius ($\bar{R} = 1750$ μm), one may approximate the shear rate as a constant to first order. PIV measurements were used to validate the flowrate estimates.

The effect of the shear flow can be observed in the snapshot of Fig. 4.1a. The drops start out nearly circular (first drop upstream) and their shape begins to deviate as they enter the bend (second and third drops). During this period, sharp corners appear on the rear of the drop, which may also display a straight interface (e.g. fourth drop). We

associate this "rigidity" with the continuous deposition of surfactant molecules on the rear interface. Indeed, the symmetry between the leading and trailing edges is broken by the no-slip condition at the upper and lower walls, so the stationary oil layer continuously sweeps surfactant molecules to the rear of the drop. The drops continuously elongate until a critical point at which they change their orientation and position, aligning their major axis tangent to the channel and migrating towards the inner channel wall (most downstream drop).

A reconstructed history of a single drop is shown at regular time intervals in Fig. 4.1b. The position of the centroid (red circles) shows that the drop accelerates and its center migrates towards the inner wall. These shape and velocity transitions are accompanied by the production of one or more tails at the rear of the drop, which then break up into small droplets behind the mother drop (Fig. 4.1c). The droplets thus produced are polydisperse but a size histogram displays a large peak at the limit of our optical resolution, implying the presence of a large population below a diameter of about 1 μm. This tip streaming only appears for large enough total flow rate and in the presence of surfactant. Experiments carried out without surfactant showed no tip streaming, while those with a high surfactant concentration showed reduced tails and smaller drop acceleration.

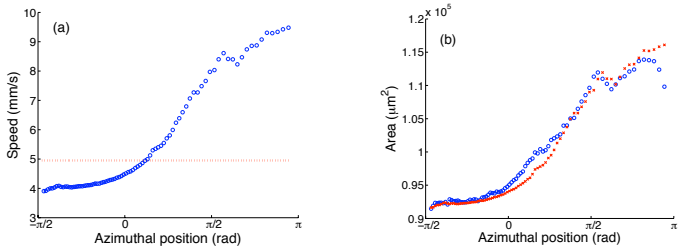

Figure 4.2: Typical evolution for one drop: (a) the velocity as a function of azimuthal position. The dashed line gives the fluid's mean nominal velocity. (b) Drop area as measured (o) and as computed (x) from the velocity using Bretherton's law. Experimental condition : $c = 0.05$ %, $Q = 5.2$ μL/min.

Several quantities go through large changes during the transition to tip-streaming. In particular, the velocity history of a drop is shown in Fig. 4.2a as a function of the azimuthal position of the centroid (θ). The drop initially travels slower than the mean velocity of the oil (marked by the dashed line) but it accelerates to reach a value about twice the mean fluid velocity by the end of the channel.

The increase in velocity is also associated with an increase in the apparent surface area of the drop (Fig. 4.2b), which can be understood by considering the thickness of the lubricating film on the upper and lower channel walls: the thickness (e) of this film may be estimated using Bretherton's law [24] which states that the film left behind an advancing air finger increases as $e/h \sim \mathrm{Ca}^{2/3}$. This scaling was verified by using the initial thickness (e_0) of the film as a free fitting parameter and computing the predicted surface area of the drop as $A = A_0[h - 2e_0]/[h - 2e_0(V/V_0)^{2/3}]$. A comparison of the measured area with the prediction for A shows good agreement, although a time lag is often observed. The initial film thickness was thus found to be approximately $5 - 8$ μm for the different experimental condition.

By finding the azimuthal position of maximum radial extent, we can define a position for the destabilization. This is shown in Fig. 4.3(a) where we have plotted the normalized relative radial extension ($\Delta R = (dr - dr_0)/dr$) of different drops as a function of azimuthal position. We observe that ΔR follows the same evolution for all experimental conditions. The position for destabilization can then be measured for the different control parameters, as shown in Fig. 4.3. We observe that the critical angle θ_c depends strongly on the drop size and on the total flowrate, but does not show a strong dependence on the surfactant concentration.

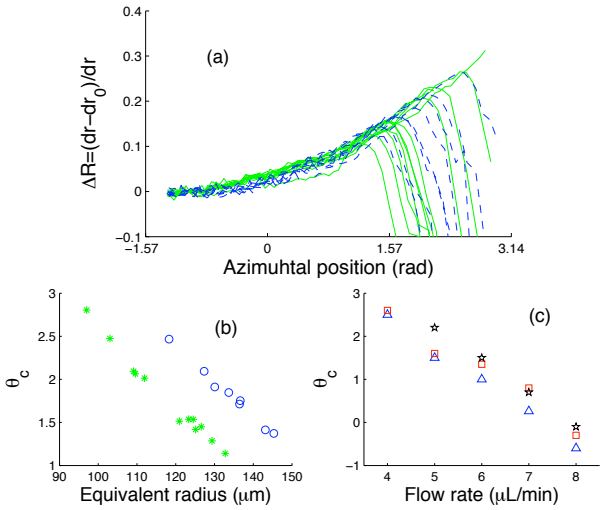

Figure 4.3: (a) Relative radial stretching as a function of azimuthal position. The same evolution is observed for all the drops, regardless of experimental conditions. (b) Critical azimuthal position for destabilization (θ_c) as a function of drop size for two flow rates ($\circ$) $Q = 6.2$ μL/min and ($*$) $Q = 8.2$ μL/min). (c) Variations in θ_c with flow rate for a given drop surface area ($A = 82.10^3 \mu m^2 \pm 7\%$).

Two capillary numbers can be written which describe the balance between viscous and capillary effects on a drop. The first one accounts for the fact that the drop is subjected to a parabolic profile in the thickness of the channel. This number, which we write $\mathrm{Ca}^{\perp}$, may be written as:

$$\mathrm{Ca}^{\perp} = \frac{a}{\gamma}\frac{\mu_o V_o}{e} = \frac{a}{h}\left[\frac{\mu_o V_o}{\gamma}\right]^{1/3}, \tag{4.1}$$

where μ_o is the oil viscosity, γ is a characteristic interfacial tension value (e.g. 20 mN/m), V_o is the drop velocity at the entrance, and a is the drop size, obtained from its apparent area.

The value of this capillary number at the moment of destabilization is plotted on Fig. 4.4a ($\star$) as a function of the drop size, for a given of flow rate and surfactant concentration. This value is seen to monotonically increase with drop size.

This capillary number must be modified, however, by the shear G experienced by the drop in the plane of the channel, which is imposed externally by the circular geometry. This second capillary number can be written as

$$\mathrm{Ca}^{\parallel} = \alpha \frac{\mu_o G a}{\gamma} \Delta R, \tag{4.2}$$

where G is the shear rate from the base flow, ΔR is the relative radial extension of the drop, and α a free parameter which will be used to compare the two capillary numbers ($\alpha \simeq 90$ in our case).

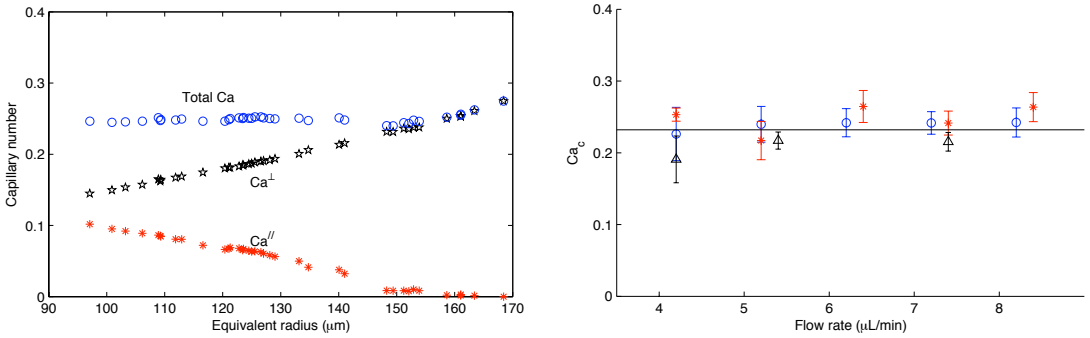

Figure 4.4: (a) Contribution of the different components of capillary number at destabilization. Experimental conditions : Flow rate 8 μ L/min - Surfactant concentration = 0.05% (b) Critical value of the capillary number at the destabilization. The error bars represent the amplitude of values fixing flow rate and surfactant concentration. The different values of the surfactant concentration are 0.05%(o), 0.15%(x) and 0.5%(+).

In this way, one may write a total capillary number as the sum $\mathrm{Ca} = \mathrm{Ca}^{\parallel} + \mathrm{Ca}^{\perp}$. Drops were found to destabilize for a constant value of Ca independent of their drop size (for $a \lesssim 150$ μm), as shown in Fig. 4.4(left). We see that Ca takes on a constant critical value, independently of flow rate, surfactant concentration, or drop size (Fig 4.4(right)).

The significance of this "total capillary number" is still not fully understood, but these experiments represent a clear example where microfluidics offers a unique tool to access fluid dynamical situations which would otherwise be very difficult to study.

4.2 Flows in networks

This work is currently underway, in collaboration with Yu Song (phd student) and Michaël Baudoin (post-doc), while closely working with Paul Manneville.

The results of Chap. 2 lead to the natural desire to look at several generations of bifurcations rather than limiting oneself to flow through a single bifurcation. However, flows in complex networks, as the one shown in Fig. 4.5(left), require mathematical tools distinct from the ones developed in our previous work. The dynamical description of the previous sections must now be replaced with the statistical description of a flow through a branched structure.

The flow of plugs of liquid pushed by a mean air flux is currently being studied at LadHyX, as shown in Fig. 4.5(right). The questions we wish to pursue are related to the stability of the flow distribution through the network, i.e. whether the nonlinearities introduced by the drops will lead to strongly inhomogeneous flow through the

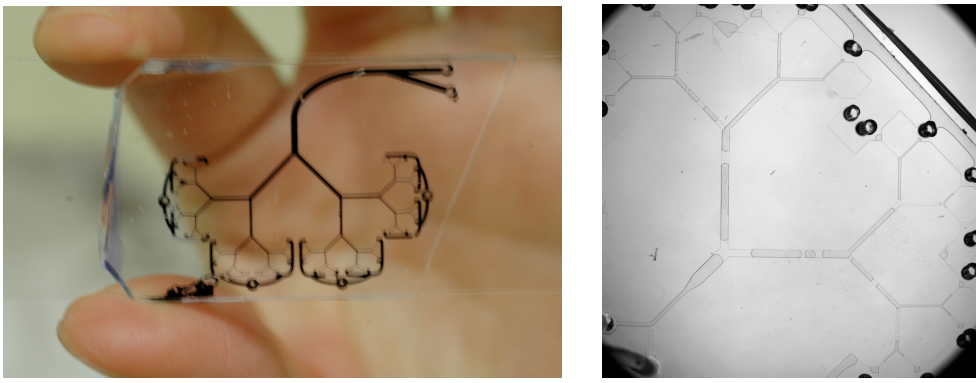

Figure 4.5: (left) An early realization of a network of microchannels at LadHyX. (right) Microscopy image of a network containing a random distribution of plugs.

whole branched structure. Preliminary results confirm that the downstream boundary conditions play a major role in determining the flow paths and may have to be taken into account in the theoretical modeling of the network.

4.3 Manipulation of single cells in drops

It is only fitting to end this document with the application of droplet methods to biological experiments, since we started by stating the major impact that microfluidics could have on biology and chemistry. This for us will consist of very recent but mainly future work, where we explore the manipulation of single cells (or a small population of cells) inside a droplet. Contrary to the experiments discussed in the previous parts of the manuscript, the aim here is neither to explore toy models nor to develop new tools. The purpose of these studies is to shed new light on biological mechanisms by using the tools that we have already developed. These biological projects are very exciting but involve a significant effort to develop the biological know-how in the ladhyx group.

For this, several collaborations have been started with biologists and biophysicists, for example at the "Laboratoire d'Optique et Biosciences" (LOB) at Ecole Polytechnique, where a project was started with Antigoni Alexandrou to run experiments on a large number of cells, by flowing the cells in drops in series. An early image of a cell in a drop is shown in Fig. 4.6, where a red blood cell is followed in time as the drop that carries it travels from left to right.

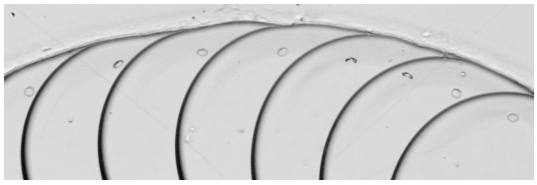

Figure 4.6: Superposition of eight images showing the evolution of a red blood cell in a drop.

The current approach to biological experiments generally consists either in performing detailed and time consuming experiments on a single cell, or in working with tissues

where the number of cells is large. The gap that we hope to bridge with our project is to be able to work with a large number of single cells, thus combining the statistical power of tissue experiments with the detailed measurements of single cell experiments. Microfluidics can allow such measurements since one may perform many copies of an experiment in drops that follow each other, while varying the parameters slightly. By performing experiments in this way, one can expect to provide a new type of information on biological processes that can help in understanding the complex mechanisms at play in biology.

Bibliography

[1] http://www.parl.clemson.edu/stare.

[2] Abkarian, M., Faivre, M., and Stone, H. High-speed microfluidic differential manometer for cellular-scale hydrodynamics. *Proc. Nat. Acad. Sci. 103*, 3 (2006), 538–542.

[3] Adzima, B., and Velankar, S. Pressure drops for droplet flows in microfluidic channels. *J. of micromechanics and microengineering 16*, 8 (2006), 1504 – 1510.

[4] Ahn, K., Agresti, J., Chong, H., Marquez, M., and Weitz, D. Electrocoalescence of drops synchronized by size-dependent flow in microfluidic channels. *Appl. Phys. Lett. 88* (2006), 264105.

[5] Ahn, K., Kerbage, C., Hynt, T., Westervelt, R., Link, D., and Weitz, D. Dielectrophoretic manipulation of drops for high-speed microfluidic sorting devices. *Appl. Phys. Lett. 88* (2006), 024104.

[6] Ajaev, V. S., and Homsy, G. Modeling shapes and dynamics of confined bubbles. *Ann. Rev. Fluid Mech. 38*, 1 (2006), 277–307.

[7] Anna, S., Bontoux, N., and Stone, H. Formation of dispersions using 'flow-focusing' in microchannels. *Appl. Phys. Lett. 82*, 3 (2003), 364–366.

[8] Anna, S., and Mayer, H. Microscale tipstreaming in a microfluidic flow focusing device. *Physics of Fluids 18*, 12 (2006), 121512.

[9] Aubert, C., and Colin, S. High-order boundary conditions for gaseous flows in rectangular microducts. *Nanoscale and Microscale Thermophysical Engineering 5*, 1 (2001), 41–54.

[10] Barbier, V., Willaime, H., Tabeling, P., and Jousse, F. Producing droplets in parallel microfluidic systems. *Phys. Review E 74*, 4 (2006), 046306.

[11] Baroud, C., de Saint Vincent, M., and Delville, J.-P. An optical toolbox for total control of droplet microfluidics. *Lab Chip 7* (July 2007), 1029–1033.

[12] Baroud, C., Delville, J., Gallaire, F., and Wunenburger, R. Thermocapillary valve for droplet production and sorting. *Phys. Rev. E 75*, 4 (2007), 046302.

[13] Baroud, C., Okkels, F., Ménétrier, L., and Tabeling, P. Reaction-diffusion dynamics: confrontation between theory and experiment in a microfluidic reactor. *Phys. Rev. E 67* (July 2003), 060104(R).

[14] Baroud, C., Tsikata, S., and Heil, M. The propagation of low-viscosity fingers into fluid-filled, branching networks. *J. Fluid Mech. 546* (2006), 285–294.

[15] Baroud, C., Wang, X., and Masson, J.-B. Collective behavior during the exit of a wetting liquid through a network of channels. *J. Colloid and Interface Sci. 326* (October 2008), 445–450.

[16] Bazhlekov, I., Anderson, P., and Meijer, H. Numerical investigation of the effect of insoluble surfactants on drop deformation and breakup in simple shear flow. *J. Colloid Interface Sci. 298* (2006), 369–394.

[17] Berthier, E., and Beebe, D. Flow rate analysis of a surface tension driven passive micropump. *Lab on a Chip 7*, 11 (2007), 1475–1478.

[18] Bibette, J., Morse, D., Witten, T., and Weitz, D. Stability criteria for emulsions. *Phys. Rev. Lett. 69* (1992), 2439–2442.

[19] Bico, J., and Quéré, D. Falling slugs. *J. Coll. and Interface Science 243* (2001), 262–264.

[20] Bohn, S., Andreotti, B., Douady, S., Munzinger, J., and Couder, Y. Constitutive property of the local organization of leaf venation networks. *Phys. Rev. E 65*, 6 (Jun 2002), 061914.

[21] Boos, W., and Thess, A. Thermocapillary flow in a hele-shaw cell. *J. Fluid Mech. 352* (1997), 305–320.

[22] Braun, D., and Libchaber, A. Trapping of dna by thermophoretic depletion and convection. *Phys. Rev. Lett. 89* (2002), 188103.

[23] Bremond, N., Thiam, A., and Bibette, J. Decompressing emulsion droplets favors coalescence. *Physical Review Letters 100*, 2 (2008), 024501.

[24] Bretherton, F. The motion of long bubbles in tubes. *J. Fluid Mech. 10* (1961), 166–188.

[25] Brouzes, E., Branciforte, J., Twardowski, M., Marran, D., Suo, Y., Charles, Y., Boitard, L., Perrimon, N., and Link, D. Droplet-based high-throughput live/dead cell assay. In *Proceedings of Micro-TAS 2006* (2006).

[26] Bryant, S., Mellor, D., and Cade, C. Physically representative network models of transport in porous media. *AIChE Journal 39*, 3 (1993), 387–396.

[27] Burnham, D., and McGloin, D. Holographic optical trapping of aerosol droplets. *Optics Express 14*, 9 (2006), 4176–4182.

[28] Burnham, D., Wright, G., Read, N., and McGloin, D. Holographic and single beam optical manipulation of hyphal growth in filamentous fungi. *Journal of Optics A: Pure and Applied Optics 9*, 8 (2007), S172–S179.

[29] Bush, J. The anomalous wake accompanying bubbles rising in a thin gap: a mechanically forced marangoni flow. *J. Fluid Mech. 352* (1997), 283–303.

[30] Calderon, A., and Fowlkes, B. Bull, J. Bubble splitting in bifurcating tubes: a model study of cardiovascular gas emboli transport. *J. Appl. Physiol. 99* (2005), 479–487.

[31] Cassidy, K., Gavriely, N., and Grotberg, J. Liquid plug flow in straight and bifurcating tubes. *J. Biomech. Eng. 123* (2001), 580–589.

[32] Chabert, M., Dorfman, K., de Cremoux, P., Roeraade, J., and Viovy, J.-L. Automated microdroplet platform for sample manipulation and polymerase chain reaction. *Anal. Chem. 78* (2006), 7722–7728.

[33] Chabert, M., Dorfman, K. D., and Viovy, J. Droplet fusion by alternating current (AC) field electrocoalescence in microchannels. *Electrophoresis 26* (2005), 3706–3715.

[34] Cicciarelli, B., Elia, J., Hatton, T., and Smith, K. Temperature dependence of aggregation and dynamic surface tension in a photoresponsive surfactant system. *Langmuir 23*, 16 (2007), 8323–8330.

[35] Cohen, I., and Nagel, S. Scaling at the selective withdrawal transition through a tube suspended above the fluid surface. *Phys. Rev. Lett. 88*, 7 (2002), 074501.

[36] Constantin, P., Dupont, T., Goldstein, R., Kadanoff, L., and Shelley, M. Droplet breakup in a model of the Hele-Shaw cell. *Phys. Rev. E 47*, 6 (1993), 4169–4181.

[37] Cordero, M., Burnham, D., Baroud, C., and McGloin, D. Thermocapillary manipulation of droplets using holographic beam shaping: Microfluidic pin ball. *Appl. Phys. Lett. 93*, 3 (2008), 034107.

[38] Cordero, M., Verneuil, E., and Baroud, C. Optical forcing of microdrops : Flows and temperature field characterization. In *Proceedings of MicroTAS 2007* (2007).

[39] Courrech du Pont, S., and Eggers, J. Sink flow deforms the interface between a viscous liquid and air into a tip singularity. *Phys. Rev. Lett. 96* (2006), 034501–1–4.

[40] Cristobal, G., Benoit, J., Joanicot, M., and Ajdari, A. Microfluidic bypass for efficient passive regulation of droplet traffic at a junction. *Appl. Phys. Lett. 89* (2006), 034104.

[41] Darhuber, A., and Troian, S. Principles of microfluidic actuation by modulation of surface stresses. *Annu. Rev. Fluid Mech. 37* (2005), 425–455.

[42] Darhuber, A., Valentino, J., Davis, J., Troian, S., and Wagner, S. Microfluidic actuation by modulation of surface stresses. *Appl. Phys. Letters 82*, 4 (January 2003), 657–659.

[43] de Bruijn, R. Tipstreaming of drops in simple shear flows. *Chem. Eng. Sci. 48*, 2 (1993), 277–294.

[44] de Gennes, P. Wetting: statics and dynamics. *Rev. Mod. Phys. 57*, 3 (1985), 827–863.

[45] Dollet, B., van Hoeve, W., Raven, J., Marmottant, P., and Versluis, M. Role of the channel geometry on the bubble pinch-off in flow-focusing devices. *Physical Review Letters 100*, 3 (2008), 034504.

[46] Dreyfus, R., Tabeling, P., and Willaime, H. Ordered and discordered patterns in two phase flows in microchannels. *Phys. Rev. Lett. 90* (April 2003), 144505.

[47] Duclaux, V., Clanet, C., and Quéré, D. The effects of gravity on the capillary instability in tubes. *J. Fluid Mech. 556* (2006), 217–226.

[48] Duhr, S., Arduini, S., and Braun, D. Thermophoresis of dna determined by microfluidic fluorescence. *Eur. Phys. J. E 15* (2004), 277–286. DOI 10.1140/epje/i2004-10073-5.

[49] Eastoe, J., and Dalton, J. Dynamic surface tension and adsorption mechanisms of surfactants at the air-water interface. *Adv. Colloid Interface Sci. 85* (2000), 103–144.

[50] Eggleton, C., Tsai, T.-M., and Stebe, K. Tip streaming from a drop in the presence of surfactants. *Phys. Rev. Lett. 87* (2001), 048302–1–4.

[51] Engl, W., Roche, M., Colin, A., Panizza, P., and Ajdari, A. Droplet Traffic at a Simple Junction at Low Capillary Numbers. *Physical Review Letters 95*, 20 (2005), 208304.

[52] Espinosa, F., and Kamm, R. Bolus dispersal through the lungs in surfactant replacement therapy. *J. Appl. Physiol. 86*, 1 (1999), 391–410.

[53] Fernandez, J., and Homsy, G. Chemical reaction-driven tip-streaming phenomena in a pendant drop. *Phys. Fluids 16*, 7 (2004), 2548–2555.

[54] Ferri, J., and Stebe, K. Which surfactants reduce surface tension faster? a scaling argument for diffusion-controlled adsorption. *Adv. Colloid and Interface Science 85* (2000), 61–97.

[55] Fuerstman, M., Garstecki, P., and Whitesides, G. coding/decoding and reversibility of droplet trains in microfluidic networks. *Science 315* (2007), 828–832.

[56] Fuerstman, M., Lai, A., Thurlow, M., Shevkoplyas, S., Stone, H., and Whitesides, G. The pressure drop along rectangular microchannels containing bubbles. *Lab on a Chip 7*, 11 (2007), 1479–1489.

[57] Gallaire, F., and Baroud, C. Marangoni induced force on drop in a microchannel. *In Preparation* (2007).

[58] Garstecki, P., Stone, H., and Whiteseides, G. Mechanism for flow-rate controlled breakup in confined geometries: A route to monodisperse emulsions. *Phys. Rev. Lett. 94* (2005), 164501.

[59] Grier, D. A revolution in optical maniupulation. *Nature 424* (Aug. 2003), 810–816.

[60] Guillot, P., Colin, A., Utada, A., and Ajdari, A. Stability of a jet in confined pressure-driven biphasic flows at low reynolds numbers. *Phys. Rev. Lett 99* (2007), 104502.

[61] Günther, A., and Jensen, K. Multiphase microfluidics: from flow characteristics to chemical and material synthesis. *Lab Chip 6* (2006), 1487–1503.

[62] Hazel, A. L., and Heil, M. The steady propagation of a semi-infinite bubble into a tube of elliptical or rectangular cross-section. *J. Fluid Mech. 470* (2002), 91–114.

[63] Hoffman, R. A study of the advancing interface. *J. Colloid and Interface Science 50*, 2 (75), 228–241.

[64] Hu, Y., and Lips, A. Estimating surfactant surface coverage and decomposing its effect on drop deformation. *Phys. Rev. Lett. 91* (2003), 044501.

[65] Huang, L., Cox, E., Austin, R., and Sturm, J. Continuous particle separation through deterministic lateral displacement. *Science 304* (2004), 987–990.

[66] Hudson, S. D., Cabral, J. T., William J. Goodrum, J., Beers, K. L., and Amis, E. J. Microfluidic interfacial tensiometry. *Appl. Phys. Lett. 87*, 8 (2005), 081905.

[67] Ismagilov, R., Stroock, A., Kenis, P., Whitesides, G., and Stone, H. Experimental and theoretical scaling laws for transverse diffusive broadening in two-phase laminar flows in microchannels. *Appl. Phys. Lett. 76*, 17 (April 2000), 2376–2378.

[68] Jeffries, G., Kuo, J., and Chiu, D. Controlled Shrinkage and Re-expansion of a Single Aqueous Droplet inside an Optical Vortex Trap. *Journal of physical chemistry. B, Condensed matter, materials, surfaces, interfaces, & biophysical chemistry 111*, 11 (2007), 2806–2812.

[69] Jin, F., Gupta, N., and Stebe, K. The detachment of a viscous drop in a viscous solution in the presence of a soluble surfactant. *Physics of Fluids 18* (2006), 022103.

[70] Joanicot, M., and Ajdari, A. Droplet control for microfluidics. *Science 309* (2005), 887–888.

[71] Jung, B., Bharadwaj, R., and Santiago, J. Thousandfold signal increase using field-amplified sample stacking for on-chip electrophoresis. *Electrophoresis 24* (2003), 3476–3483.

[72] Khan, S., Günther, A., Schmidt, M., and Jensen, K. Microfluidic synthesis of colloidal silica. *Langmuir 20*, 20 (2004), 8604–8611.

[73] Kopp, M., de Mello, A., and Manz, A. Chemical amplification: Continuous-flow pcr on a chip. *Science 280* (May 1998), 1046–1048.

[74] Kotz, K., Noble, K., and Faris, G. Optical microfluidics. *Appl. Phys. Lett. 85*, 13 (2004), 2658–2660.

[75] Lajeunesse, E., and Homsy, G. Thermocapillary migration of long bubbles in polygonal tubes. ii. experiments. *Phys. Fluids 15* (2003), 308–314.

[76] Laser, D., and Santiago, J. A review of micropumps. *J. Micromech. Microeng. 14* (2004), R35–R64.

[77] Laval, P., Salmon, J., and Joanicot, M. A microfluidic device for investigating crystal nucleation kinetics. *Journal of Crystal Growth 303*, 2 (2007), 622–628.

[78] Lee, J. N., Park, C., and Whitesides, G. Solven compatibility of poly(dimethylsiloxane)-based microfluidic devices. *Anal. Chem. 75* (2003), 6544–6554.

[79] Lenormand, R. Pattern growth and fluid displacements through porous media. *Physica 140A* (1986), 114–123.

[80] Lenormand, R., and Zarcone, C. Role of roughness and edges during imbibition in square capillaries. *SPE* (1984).

[81] Levich, V. *Physicochemical Hydrodynamics*. Prentice Hall, Englewood Clifs, N.J., 1962.

[82] Link, D., Anna, S., Weitz, D., and Stone, H. Geometrically mediated breakup of drops in microfluidic devices. *Phys. Rev. Lett. 92*, 5 (2004), 054503.

[83] Liu, R., Stremler, M., Sharp, K., Olsen, M., Santiago, J., Adrian, R., Aref, H., and Beebe, D. Passive mixing in a three-dimensional serpentine microchannel. *Microelectromechanical Systems, Journal of 9*, 2 (2000), 190–197.

[84] Lorenceau, E., Restagno, F., and Quéré, D. Fracture of a viscous liquid. *Phys. Rev. Lett. 90*, 18 (May 2003), 184501.

[85] Madou, M. *Fundamentals of microfabrication: The science of miniaturization*, second ed. CRC Press, 2002.

[86] Marmottant, P., and Hilgenfeldt, S. A bubble-driven microfluidic transport element for bioengineering. *Proc. Nat. Acad. Sci. 101*, 26 (2004), 9523–9527.

[87] Maurer, J., Tabeling, P., Joseph, P., and Willaime, H. Second-order slip laws in microchannels for helium and nitrogen. *Phys. Fluids 15*, 9 (2003), 2613–2621.

[88] Mazouchi, A., and Homsy, G. Thermocapillary migration of long bubbles in cylindrical capillary tubes. *Phys. Fluids 12*, 3 (2000), 542–549.

[89] Mietus, W., Matar, O., Lawrence, C. J., and Briscoe, B. J. Droplet deformation in con. *Chem. Eng. Sci. 57* (2002), 1217–1230.

[90] Nadim, A., Borhan, A., and Haj-Hariri, H. Tangential stress and marangoni effects at a fluid-fluid interface in a hele-shaw cell. *J. Colloid and Interface Science 181* (1996), 159–164.

[91] Ody, C., Baroud, C., and de Langre, E. Transport of wetting liquid plugs in bifurcating microfluidic channels. *J. Colloid Interface Sci. 308* (Jan. 2007), 231–238.

[92] Okkels, F., and Tabeling, P. Spatiotemporal Resonances in Mixing of Open Viscous Fluids. *Physical Review Letters 92*, 3 (2004), 38301.

[93] Oron, A., Davis, S., and Bankoff, S. Long-scale evolution of thin liquid films. *Revs. Modern Physics 69*, 3 (1997), 931 – 980.

[94] Park, C.-W., Maruvada, S., and Yoon, D.-Y. The influence of surfactant on the bubble motion in hele-shaw cells. *Phys. Fluids 6* (1994), 3267–3275.

[95] Pollack, M., Fair, R., and Shenderov, A. Electrowetting-based actuation of liquid droplets for microfluidic applications. *Appl. Phys. Lett. 77*, 11 (2000), 1725–1726.

[96] Priest, C., Herminghaus, S., and Seemann, R. Controlled electrocoalescence in microfluidics: Targeting a single lamella. *Appl. Phys. Lett. 89* (Sept 2006), 134101.

[97] Quillet, C., and Berge, B. Electrowetting: A recent outbreak. *Curr. Opin. Colloid Interface Sci. 6*, 1 (2001), 34–39.

[98] Renaudin, A., Tabourier, P., Zhang, V., Camart, J., and Druon, C. SAW nanopump for handling droplets in view of biological applications. *Sensors & Actuators: B. Chemical 113*, 1 (2006), 389–397.

[99] Ross, D., Gaitan, M., and Locascio, L. Temperature measurements in microfluidic systems using a temperature-dependent fluorescent dye. *Anal. Chem. 73* (2001), 4117–4123.

[100] Saint-Jalmes, A., Zhang, Y., and Langevin, D. Quantitative description of foam drainage: Transitions with surface mobility. *Eur. Phys. J. E 15* (2004), 53–60.

[101] Sammarco, T., and Burns, M. Thermocapillary pumping of discrete drops in microfabricated analysis devices. *AIChE J. 45*, 2 (1999), 350–366.

[102] Sarrazin, F., Loubière, K., Prat, L., Gourdon, C., Bonometti, T., and Magnaudet, J. Experimental and numerical study of droplets hydrodynamics in microchannels. *AiChE J. 52* (2006), 4061–4070.

[103] Sarrazin, F., Prat, L., Di Miceli, N., Cristobal, G., Link, D., and Weitz, D. Mixing characterization inside microdroplets engineered on a microcoalescer. *Chem. Eng. Sci. 62* (2007), 1042–1048.

[104] Schindler, M., and Ajdari, A. Droplet traffic in microfluidic networks: A simple model for understanding and designing. *Physical Review Letters 100*, 4 (2008), 044501.

[105] Sibillo, V., Pasquariello, G., Simeone, M., Cristini, V., and Guido, S. Drop deformation in microconfined shear flow. *Phys. Rev. Lett. 97*, 5 (2006), 054502.

[106] Song, H., and Ismagilov, R. Millisecond kinetics on a microfluidic chip using nanoliters of reagents. *J. Am. Chem. Soc 125*, 14 (2003), 613.

[107] Song, H., Tice, J., and Ismagilov, R. A microfluidic system for controlling reaction networks in time. *Angew. Chem., Int. Ed. 42*, 7 (2003), 768–772.

[108] Squires, T., and Quake, S. Microfluidics: Fluid physics at the nanoliter scale. *Rev. Mod. Phys. 77*, 3 (July 2005), 977–1026.

[109] Stark, J., and Manga, M. The motion of long bubbles in a network of tubes. *Transport in Porous Media 40* (2000), 201–218.

[110] Stone, H., Strook, A., and Ajdari, A. Engineering flows in small devices: Microfluidics toward a lab-on-a-chip. *Annu. Rev. Fluid Mech. 36* (2004), 381–411.

[111] Strook, A., Dertinger, S., Ajdari, A., Mezic, I., Stone, H., and Whitesides, G. Chaotic mixer for microchannels. *Science 295* (2002), 647–651.

[112] Sun, B., Lim, D., Kuo, J., Kuyper, C., and Chiu, D. Fast initiation of chemical reactions with laser-induced breakdown of a nanoscale partition. *Langmuir 20*, 22 (2004), 9437–9440.

[113] Tan, Y.-C., Fisher, J., Lee, A., Cristini, V., and Lee, A. Design of microfluidic channel geometries for the control of droplet volume, chemical concentration, and sorting. *Lab Chip 4* (2004), 292–298.

[114] Tanner, L. The spreading of silicone oil drops on horizontal surfaces. *J. Phys. D: Appl. Phys. 12* (1979), 1473–1484.

[115] Tawfik, D., and Griffiths, A. Man-made cell-like compartments for molecular evolution. *Nature Biotech. 16* (1998), 652–656.

[116] Taylor, G. The viscosity of a fluid containing small drops of another fluid. *Proceedings of the Royal Society of London. Series A 138* (1932), 41–48.

[117] Taylor, G. The formation of emulsions in definable fields of flow. *Proceedings of the Royal Society of London. Series A 146* (1934), 501–523.

[118] Taylor, G. Deposition of a viscous fluid on the wall of a tube. *J. Fluid Mech. 10* (1961), 161–165.

[119] Velev, O., Prevo, B., and Bhatt, K. Onchip manipulation of free droplets. *Nature 426* (2003), 515–516.

[120] Vennemann, P., Kiger, K., Lindken, R., Groenendijk, B. C., Stekelenburg-de vos, S., Ten Hagen, T. L., Ursem, N. T., Poelmann, R. E., Westerweel, J., and Hierck, B. P. In vivo micro particle image velocimetry measurements of blood-plasma in the embryonic avian heart. *Journal of Biomechanics 39*, 7 (2006), 1191 – 1200.

[121] Verneuil, E., Cordero, M., Gallaire, F., and Baroud, C. Anomalous thermocapillary force on microdroplet: Origin and magnitude. *Submitted* (2008).

[122] Weibel, E. R. *The pathway for oxygen*. Harvard U. press, Cambridge, MA., USA, 1984.

[123] White, F. *Viscous fluid flow*. McGraw Hill, 1991.

[124] Young, N., Goldstein, J., and Block, M. The motion of bubbles in a vertical temperature gradient. *J. Fluid Mech. 6* (1959), 350–356.

[125] Zheng, B., Tice, J., Roach, L., and Ismagilov, R. A droplet based, composite pdms/glass capillary microfluidic system for evaluating protein crystallization conditions by microbatch and vapor-diffusion methods with on-chip x-ray diffraction. *Angew. Chem. Int. Ed. 43*, 19 (May 2004), 2508–2511.

[126] Zhu, X., and Kim, E. Microfluidic motion generation with acoustic waves. *Sensors & Actuators: A. Physical 66*, 1-3 (1998), 355–360.